BEILSTEIN JOURNAL OF NANOTECHNOLOGY

Physics and optical applications of all-dielectric nanostructures

Edited by Zhanghua Han, Sanshui Xiao and Jin Xiang

Imprint

Beilstein Journal of Nanotechnology
www.bjnano.org
ISSN 2190-4286
Email: journals-support@beilstein-institut.de

The *Beilstein Journal of Nanotechnology* is published by the Beilstein-Institut zur Förderung der Chemischen Wissenschaften.

Beilstein-Institut zur Förderung der Chemischen Wissenschaften
Trakehner Straße 7–9
60487 Frankfurt am Main
Germany
www.beilstein-institut.de

BEILSTEIN JOURNAL OF NANOTECHNOLOGY

Tunable high-quality-factor absorption in a graphene monolayer based on quasi-bound states in the continuum

Jun Wu*[1], Yasong Sun[2,3], Feng Wu[4], Biyuan Wu[2,5] and Xiaohu Wu*[5]

Full Research Paper

Open Access

Address:
[1]College of Electrical Engineering, Anhui Polytechnic University, Wuhu, 241000, China, [2]Basic Research Center, School of Power and Energy, Northwestern Polytechnical University, Xi'an 710064, Shaanxi, China, [3]Center of Computational Physics and Energy Science, Yangtze River Delta Research Institute of NPU, Northwestern Polytechnical University, Taicang 215400, Jiangsu, China, [4]School of Optoelectronic Engineering, Guangdong Polytechnic Normal University, Guangzhou 510665, China and [5]Shandong Institute of Advanced Technology, Jinan 250100, China

Email:
Jun Wu* - mailswj2011@163.com; Xiaohu Wu* - xiaohu.wu@iat.cn

* Corresponding author

Keywords:
bound states in the continuum; graphene; gratings; selective absorption

Beilstein J. Nanotechnol. **2022,** *13,* 675–681.
https://doi.org/10.3762/bjnano.13.59

Received: 28 March 2022
Accepted: 08 July 2022
Published: 19 July 2022

This article is part of the thematic issue "Physics and optical applications of all-dieletric nanostructures".

Guest Editor: Z. Han

Abstract

A tunable graphene absorber, composed of a graphene monolayer and a substrate spaced by a subwavelength dielectric grating, is proposed and investigated. Strong light absorption in the graphene monolayer is achieved due to the formation of embedded optical quasi-bound states in the continuum in the subwavelength dielectric grating. The physical origin of the absorption with high quality factor is examined by investigating the electromagnetic field distributions. Interestingly, we found that the proposed absorber possesses high spatial directivity and performs similar to an antenna, which can also be utilized as a thermal emitter. Besides, the spectral position of the absorption peak can not only be adjusted by changing the geometrical parameters of dielectric grating, but it is also tunable by a small change in the Fermi level of the graphene sheet. This novel scheme to tune the absorption of graphene may find potential applications for the realization of ultrasensitive biosensors, photodetectors, and narrow-band filters.

Introduction

Absorbers possess a wide range of applications, including radar stealth, infrared detectors, thermophotovoltaic cells, and thermal emitters. According to their spectral bandwidths, the absorbers can be classified as broad-band absorbers and narrow-band absorbers [1-4]. In general, broad-band absorbers [5-8] are used for electromagnetic cloaking and solar energy conversion,

while narrow-band absorbers [9-12] have great potential in sensing and monochromatic light detecting. An example is the application of narrow-band absorbers in refractive index sensing [13]. When the absorbers are surrounded by gas or liquid, the resonance wavelength will shift as the background refractive index changes [14]. Narrow-band absorbers have attracted attention in practical applications due to the absorption with high quality factor (Q-factor), which is beneficial to improve the sensing performance. Up to now, many strategies for improving the Q-factor have been successfully proposed, such as dielectric resonant [15], all-metal [14,16] and metal–dielectric–metal (MDM) configurations [17,18]. Recently, as a type of particular localized states, optical bound states in the continuum (BICs) [19-24] have also been demonstrated to enable perfect light confinement and giant field enhancement [25-29]. Hence, quasi-BICs can be utilized to design narrow-band absorbers with high Q-factor.

Tunable absorption is interesting regarding many potential applications. There are generally two ways to achieve tunable absorption. One is to change the structural parameters and the other is to add tunable materials, such as phase change materials, graphene, or liquid crystals. Among them, graphene has attracted much attention in optics and optoelectronics [30-34]. As a single layer of carbon atoms arranged in a honeycomb structure, graphene supports much stronger binding of surface plasmon polaritons (SPPs) with less loss, which leads to a longer propagation distance compared with traditional metal SPPs [35]. In addition, its conductivity can be dynamically controlled by chemical doping or electrostatic fields owing to the linear dispersion of the Dirac fermions [36]. These features proposed for graphene enable novel active devices, including modulators [37], perfect absorbers [38,39], imaging devices [40], detectors [41], waveguides [42,43], polarizers [44], and electromagnetic chirality devices [45]. The strength of interaction between graphene and incident light plays a key role in these applications. Unfortunately, it is extremely weak owing to the single-atom thickness of graphene monolayers, which severely limits the performance of graphene devices. Various approaches based on different physical mechanisms have been proposed to enhance the absorption in graphene monolayers, such as coherent perfect absorption effect [46], critical coupling effect [47], guided mode resonance effect [48], metal Tamm plasmon polaritons effect [49], and graphene Tamm surface plasmons effect [50]. In addition, the quasi-BICs mentioned previously also can be employed to enhance the absorption in graphene monolayers [51-54]. However, in the above works, the quasi-BICs are quite sensitive to the geometric parameters, which limit their practical applications. Besides, in [51-53], the proposed structures are metasurfaces, which makes the fabrication quite difficult.

In this paper, motivated by the investigation in [28], a tunable graphene absorber, which consists of a graphene monolayer on a dielectric grating backed with a substrate, is designed and investigated. The paper is arranged as follows: First, we present the structure of the absorber and give the corresponding geometric parameters. Second, the absorption properties are calculated and the electromagnetic field distributions at the resonant wavelength are investigated to disclose the physical origin of enhanced absorption. Next, the spatial directivity is discussed so as to find its potential applications as thermal emitter with high directivity. Finally, the properties of the active absorber, including tunability with different geometric parameters and different Fermi levels are investigated.

Results

Figure 1 gives a schematic view of the proposed absorber. A graphene monolayer is placed on a one-dimensional dielectric grating, under which a dielectric substrate is used to support the device. The dielectric grating is defined by the period d, the width w, and the thickness h. The refractive indices of grating and substrate are n_h and n_s, respectively. TM polarized (the magnetic field is along the direction of the y-axis) monochromatic plane waves are incident from the substrate at an angle θ. In our simulation, we set d = 3.3 μm, w = 2.31 μm, h = 3.5 μm, n_h = 3.48, n_s = 1.45, and θ = 0.1°.

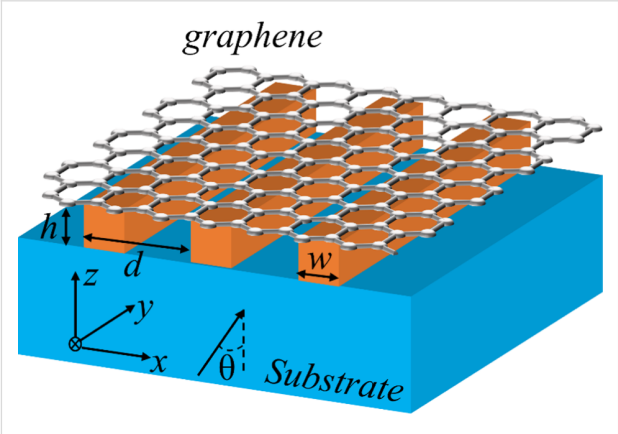

Figure 1: Schematic of the graphene absorber consisting of a graphene monolayer and a substrate separated by a dielectric grating.

The surface conductivity of graphene has intraband and interband contributions and is described by:

$$\sigma(\omega) = \sigma_{\text{intra}}(\omega) + \sigma_{\text{inter}}(\omega). \quad (1)$$

Here, σ_{intra} and σ_{inter} are the intraband and interband conductivity, respectively. In the mid-infrared wavelength region considered in this work, the Fermi level is greater than half of

the photon energy, that is, $\hbar\omega < 2E_f$. Thus, the intraband contribution will dominate the graphene conductivity as the interband transitions are negligible due to Pauli blocking. Therefore, the conductivity of graphene can be approximately expressed by the Drude-like surface conductivity σ_{intra} as follows [55,56]:

$$\sigma(\omega) = \frac{e^2 E_f}{\pi h^2} \frac{i}{\omega + i\tau^{-1}}, \quad (2)$$

where $\hbar$ is the reduced Planck's constant, E_f is the energy of the Fermi level, ω is the angular frequency, e is the elementary charge, and τ is the carrier relaxation lifetime.

In our simulation, the permittivity of the graphene monolayer is described by:

$$\varepsilon_g = 1 + \frac{i\sigma(\omega)}{\varepsilon_0 \omega h_g}, \quad (3)$$

where ε_0 is the relative permittivity of vacuum, and h_g is the thickness of the graphene, which is assumed to be 0.34 nm. Throughout this work, we assume $\tau = 0.1$ ps. The Fermi level is initially considered to be $E_f = 0.3$ eV, and its influence on absorption spectra will be analyzed latter.

Based on the parameters mentioned above, we calculated the absorption spectra shown in Figure 2. The absorption spectra $A(\lambda)$ are obtained from reflection spectra $R(\lambda)$ and transmission spectra $T(\lambda)$ through $A(\lambda) = 1 - R(\lambda) - T(\lambda)$, where, $R(\lambda)$ and $T(\lambda)$ are calculated by employing the rigorous coupled wave analysis (RCWA) method [57,58]. Clearly, a sharp strong resonant absorption peak is observed at a wavelength of 7908.03 nm. The absorption at the resonant wavelength is about 54.13%. The enhanced absorption at this wavelength is attributed to the excitation of quasi-BICs, which will be verified in the following. Moreover, the corresponding Q-factor is about 37657, which yields an ultrasharp absorption profile. Here, the Q-factor is defined by $Q = \lambda/\Delta\lambda$, where λ is the resonant wavelength of the absorption peak and $\Delta\lambda$ denotes the full width at half maximum of the peak.

To examine the physical mechanism of this phenomenon, we illustrate the distributions of the electromagnetic field at the resonant wavelength in Figure 3. Clearly, when the dielectric grating is illuminated by a TM polarized light under nearly normal incidence, the resonator will generate field distributions similar to an electric dipole [28]. At this point, H_y and E_x are antisymmetric with respect to the y–z plane, as illustrated in Figure 3a and Figure 3b. Now, radiation in the z-axis direction

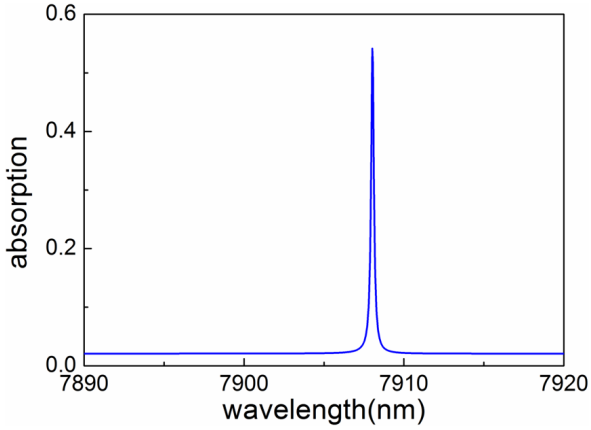

Figure 2: Simulated absorption spectrum for the graphene absorber with operating wavelength at about 7908.03 nm. Here, θ = 0.1°.

will be forbidden as the symmetry of field inside the grating is mismatched with the external field distributions [28]. At the same time, radiation to the off-z-axis direction is also forbidden because only zero-order radiation is permissible for light under normal incidence owing to the subwavelength unit cell of this structure. Therefore, the radiation mode will be confined in the dielectric grating, which results in large electric field intensity enhancement and concentration inside the grating, as presented in Figure 3d. For a nonmagnetic dispersive medium, the time-averaged power loss density is described by [59]: $dP_{loss}/dV = 1/2\varepsilon_0\omega \cdot \mathrm{Im}(\varepsilon(\omega))|E|^2$, where Im($\varepsilon$) denotes the imaginary part of relative permittivity and E is the electric field. Thus, the strong electric intensity enhancement inside the dielectric grating will boost light absorption in the graphene monolayer when it is attached on the grating. The enhanced absorption in the graphene monolayer is attributed to the excitation of optical quasi-BICs of radiation modes.

To confirm that the absorption originates from quasi-BICs, we show the simulated zero-order transmission spectra of the structures without graphene monolayer for angles of 0°, 0.1°, 0.5°, 1.0°, 1.5°, and 2.0° in Figure 4a. Clearly, with the successively reduction of the incident angle from 2.0° to 0°, the bandwidth of the Fano resonance peak decreases rapidly. At θ = 0°, the bandwidth has completely vanished, indicating an infinite Q-factor. To further confirm the formation of the BICs, we define an asymmetric parameter $\beta = \sin\theta$ and give the dependence of the Q-factor on the inverse square of the asymmetric parameter β^{-2} in Figure 4b (in log–log scale). Here, the Q-factor is calculated by $Q = \lambda_{peak}/|\lambda_{Peak} - \lambda_{dip}|$ [60]. It is found that, in the log–log scale, the Q-factor almost linearly depends on β^{-2}, indicating the formation of BICs in the proposed structure [53].

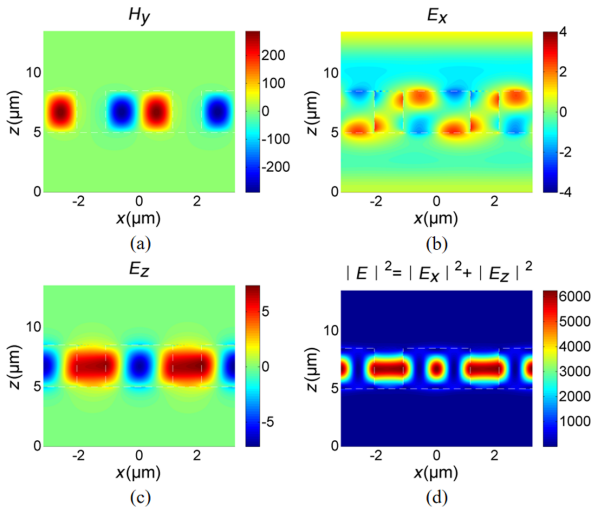

Figure 3: Electromagnetic field distributions: (a) real(H_y), (b) real(E_x), (c) real(E_z), and (d) $|E|^2 = |E_x|^2 + |E_z|^2$. The regions enclosed by the white dash line are the dielectric grating. A graphene monolayer, which cannot be displayed due to its ultrathin thickness, is attached to the dielectric grating. The origin of the z-axis is located at a surface 5 μm below the dielectric grating.

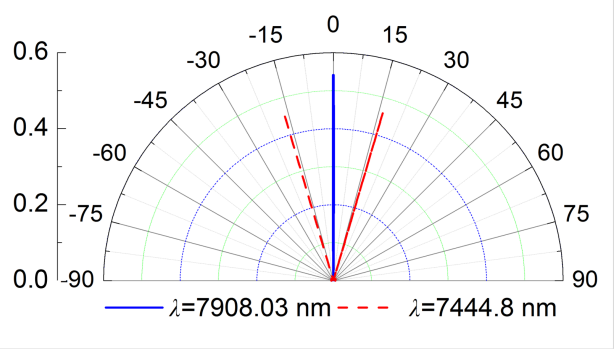

Figure 5: Polar plot of the absorption at wavelengths of λ_1 = 7908.03 nm and λ_2 = 7444.8 nm.

Discussion

Subsequently, we examine the spatial directivity of the absorber. In Figure 5, we show the polar plot of absorption at wavelengths of λ_1 = 7908.03 nm and λ_2 = 7444.8 nm. Obviously, the peak absorptions of λ_1 and λ_2 are in the direction of 0° and 16.3°, respectively. In addition, their corresponding angular widths are about 0.22° and 0.086°, respectively, which are ultranarrow angular bandwidths. Therefore, the proposed absorber possesses excellent spatial coherence as the inverse relationship between coherence length and its angular width [61]. Usually, the emissivity is the same as the absorptivity, according to the Kirchhoff's law [61]. The spectral emissivity can be obtained by multiplying the spectral absorptivity with the black-body radiation. Thus, the designed absorber could also be employed to achieve highly directional thermal emission.

As mentioned above, the absorber has an ultrasharp absorption profile due to the formation of optical quasi-BICs, indicating that the absorption is sensitive to a change of the geometric parameters. Therefore, the geometric tolerance should be precisely controlled inside a certain range during fabrication. We investigate the influence of geometric parameters on the absorption spectra so as to provide a useful guidance for practical fabrication. The results are shown in Figure 6. As shown in Figure 6a, increasing d from 3.2 to 3.4 μm results in the shift of the resonant peak to longer wavelengths. This trend is similar to the change of d when h or w are increased. Moreover, the absorption remains almost unchanged with the change of geometric parameters. It is worth noting that the absorption is more sensitive to the change of w than to that of d and h. In general, the

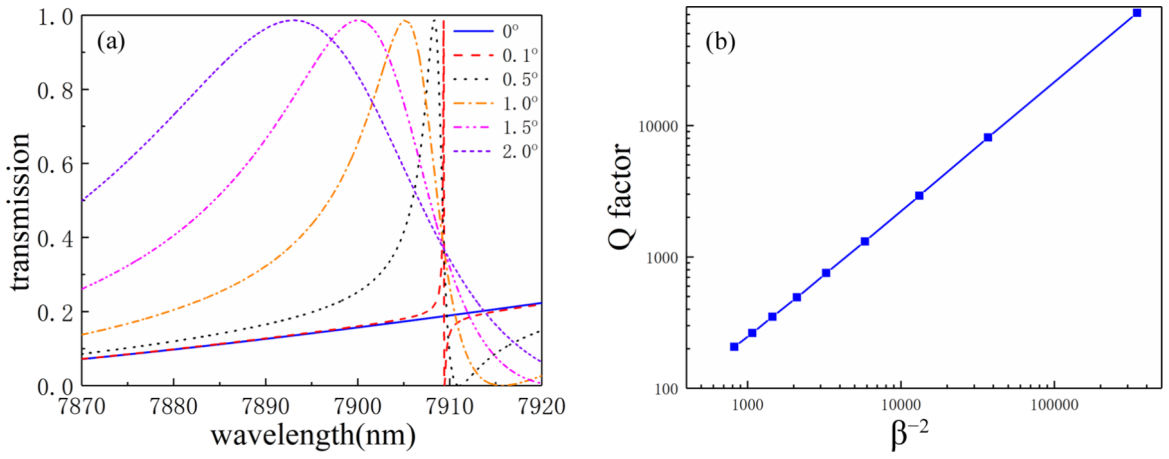

Figure 4: (a) Simulated zero-order transmission spectra of the structures without graphene monolayer for angles of 0°, 0.1°, 0.5°, 1.0°, 1.5°, and 2.0°; (b) dependence of the Q-factor on the inverse square of the asymmetric parameter β^{-2} (log–log scale).

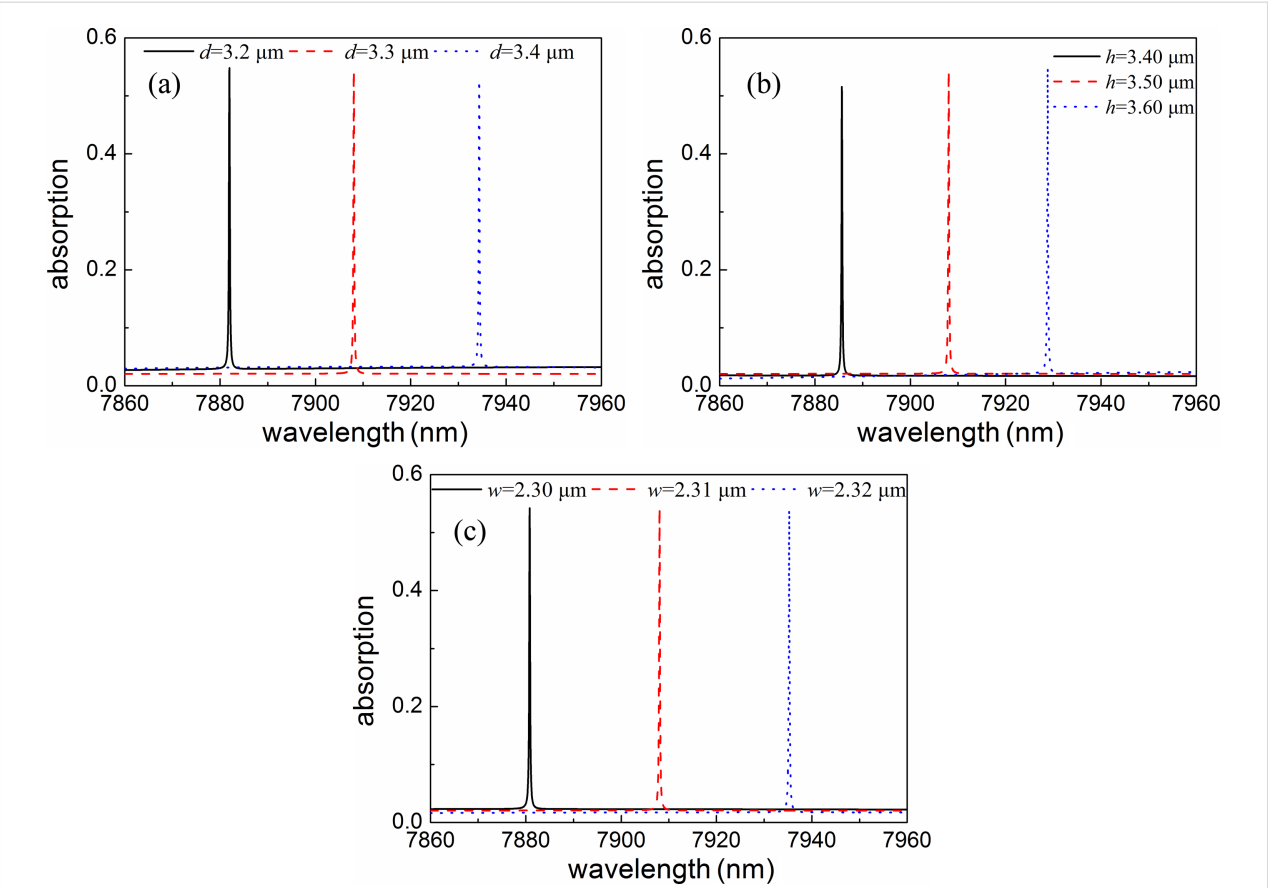

Figure 6: Absorption spectra of the graphene absorbers for different values of (a) *d*, (b) *h* and (c) *w*.

ultrasharp absorption can be maintained with a large tolerance regarding the geometric parameters, which is beneficial for real-life fabrication.

As the surface conductivity of the graphene sheet is proportional to the Fermi level (Equation 2), a change of the Fermi level should have direct influence on the graphene absorption. In Figure 7, we show the absorption spectra for different Fermi levels. Obviously, the spectral absorptivity exhibits a blueshift with E_f increasing from 0.1 to 0.5 eV. In addition, the corresponding resonant absorption increases first and then decreases again. Thus, the ultranarrow absorption could be dynamically controlled through changing the Fermi level without re-designing and re-fabricating the structure, which should be attractive for real-life applications.

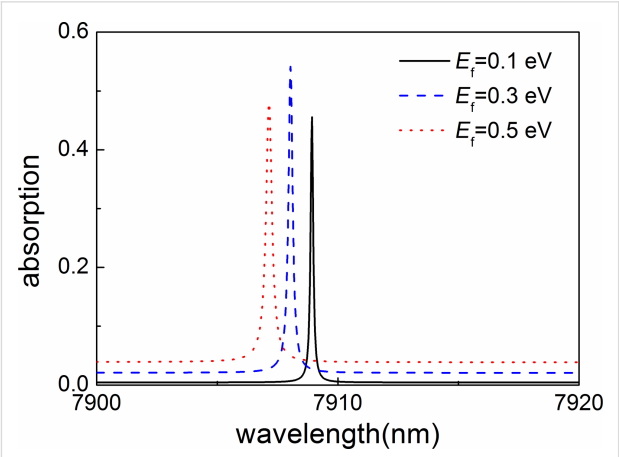

Figure 7: Absorption spectra with different Fermi levels. The geometric parameters of the absorber are the same as before.

Although the theoretical Q-factor of BICs for the dielectric resonant gating is nearly infinite, the practical Q-factor with the fabricated grating only has a large finite value. As clearly shown in Figure 6, the ultrasharp absorption can be maintained with large tolerance regarding the geometric parameters. This means that the high Q-factor of the proposed scheme is robust to the change of the geometric dimensions, which should be beneficial for real-life applications. Only theoretical design and analysis are presented in this work. For real-life applications, we could first fabricate the substrate-supported dielectric grating by means of traditional lithography, and then employ

the conventional wet-base transfer method to transfer a CVD-grown graphene monolayer onto the grating structure.

Conclusion

In summary, an active graphene absorber, consisting of a graphene monolayer and a substrate spaced by a dielectric grating, is proposed and investigated. The absorber exhibits an absolute absorption of more than 50% using a graphene monolayer, which is attributed to the extremely high field enhancement in graphene associated with embedded bound states in the dielectric grating. The electromagnetic field distributions confirm the physical origin of this phenomenon. The proposed absorber has an ultranarrow absorption profile with ultrahigh Q-factor and high spatial directivity, which enables the use as a thermal emitter with high spatial directivity. We also found that the spectral position of the absorption peak can be changed without degrading performance by adjusting the geometrical parameters. This indicates a large geometric tolerance, which is advantageous for fabrication. More importantly, the operating wavelength can be tuned by only a small change in the Fermi level, which is particularly attractive as the absorption properties can be electrically tuned without re-fabricating the whole structure. The results may find potential applications for the realization of high-performance graphene-based electrically tunable active devices including ultrasensitive biosensors, detectors, and perfect filters.

Funding

The authors acknowledge the support of the National Natural Science Foundation of China (Grant Nos. 61405217, 52106099 and 12104105), the Zhejiang Provincial Natural Science Foundation (Grant No. LY20F050001), the Anhui Provincial Natural Science Foundation (Grant No. 2108085MF231), the Anhui Polytechnic University Research Startup Foundation (Grant No. 2020YQQ042), the Pre-research Project of National Natural Science Foundation of Anhui Polytechnic University (Grant No. Xjky02202003), the Natural Science Foundation of Shandong Province (Grant No. ZR2020LLZ004), and the Start-Up Funding of Guangdong Polytechnic Normal University (Grant No. 2021SDKYA033).

References

1. Dimitriadis, A.; Kantartzis, N.; Tsiboukis, T. *Appl. Phys. A: Mater. Sci. Process.* **2012,** *109,* 1065–1070. doi:10.1007/s00339-012-7385-5
2. Wu, D.; Liu, C.; Xu, Z.; Liu, Y.; Yu, Z.; Yu, L.; Chen, L.; Li, R.; Ma, R.; Ye, H. *Mater. Des.* **2018,** *139,* 104–111. doi:10.1016/j.matdes.2017.10.077
3. Wu, X. H.; Fu, C. J. *J. Quant. Spectrosc. Radiat. Transfer* **2018,** *209,* 150–155. doi:10.1016/j.jqsrt.2018.01.031
4. Wang, J.; Fan, C.; Ding, P.; He, J.; Cheng, Y.; Hu, W.; Cai, G.; Liang, E.; Xue, Q. *Opt. Express* **2012,** *20,* 14871–14878. doi:10.1364/oe.20.014871
5. Wu, X. H.; Fu, C. J. *Nanoscale Microscale Thermophys. Eng.* **2018,** *22,* 114–123. doi:10.1080/15567265.2018.1434844
6. Wang, T.; Wang, P.; Wang, Y.; Qiao, L. *Mater. Des.* **2016,** *95,* 486–489. doi:10.1016/j.matdes.2016.01.096
7. Ding, F.; Jin, Y.; Li, B.; Cheng, H.; Mo, L.; He, S. *Laser Photonics Rev.* **2014,** *8,* 946–953. doi:10.1002/lpor.201400157
8. Wang, B.-Y.; Liu, S.-B.; Bian, B.-R.; Mao, Z.-W.; Liu, X.-C.; Ma, B.; Chen, L. *J. Appl. Phys.* **2014,** *116,* 094504. doi:10.1063/1.4894824
9. Yuan, L.; Liao, J.; Ren, A.; Huang, C.; Ji, C.; Wu, J.; Luo, X. *Plasmonics* **2021,** *16,* 1165–1174. doi:10.1007/s11468-021-01384-y
10. Wu, D.; Liu, Y.; Li, R.; Chen, L.; Ma, R.; Liu, C.; Ye, H. *Nanoscale Res. Lett.* **2016,** *11,* 483. doi:10.1186/s11671-016-1705-1
11. Huang, X.; Wang, T.; Yan, R.; Jiang, X.; Yue, X.; Wang, L. *Appl. Opt.* **2021,** *60,* 4113–4119. doi:10.1364/ao.424471
12. Askari, M. *Opt. Quantum Electron.* **2021,** *53,* 67. doi:10.1007/s11082-020-02703-z
13. Tavakoli, F.; Zarrabi, F. B.; Saghaei, H. *Appl. Opt.* **2019,** *58,* 5404–5414. doi:10.1364/ao.58.005404
14. Cheng, Y.; Zhang, H.; Mao, X. S.; Gong, R. *Mater. Lett.* **2018,** *219,* 123–126. doi:10.1016/j.matlet.2018.02.078
15. Liao, Y.-L.; Zhao, Y. *Results Phys.* **2020,** *17,* 103072. doi:10.1016/j.rinp.2020.103072
16. Li, Z.; Butun, S.; Aydin, K. *ACS Nano* **2014,** *8,* 8242–8248. doi:10.1021/nn502617t
17. Chamoli, S. K.; Singh, S. C.; Guo, C. *Plasmonics* **2020,** *15,* 1339–1350. doi:10.1007/s11468-020-01161-3
18. Lu, X.; Wan, R.; Zhang, T. *Opt. Express* **2015,** *23,* 29842–29847. doi:10.1364/oe.23.029842
19. Zhen, B.; Hsu, C. W.; Lu, L.; Stone, A. D.; Soljacic, M. *Phys. Rev. Lett.* **2014,** *113,* 257401. doi:10.1103/physrevlett.113.257401
20. Hsu, C. W.; Zhen, B.; Chua, S. L.; Johnson, S. G.; Joannopoulos, J. D.; Soljacic, M. *Light: Sci. Appl.* **2013,** *2,* e84. doi:10.1038/lsa.2013.40
21. Singh, R.; Rockstuhl, C.; Lederer, F.; Zhang, W. *Appl. Phys. Lett.* **2009,** *94,* 021116. doi:10.1063/1.3063051
22. Al-Naib, I.; Singh, R.; Rockstuhl, C.; Lederer, F.; Delprat, S.; Rocheleau, D.; Chaker, M.; Ozaki, T.; Morandotti, R. *Appl. Phys. Lett.* **2012,** *101,* 071108. doi:10.1063/1.4745790
23. Srivastava, Y. K.; Manjappa, M.; Cong, L.; Krishnamoorthy, H. N. S.; Savinov, V.; Pitchappa, P.; Singh, R. *Adv. Mater. (Weinheim, Ger.)* **2018,** *30,* 1801257. doi:10.1002/adma.201801257
24. Manjappa, M.; Solanki, A.; Kumar, A.; Sum, T. C.; Singh, R. *Adv. Mater. (Weinheim, Ger.)* **2019,** *31,* 1901455. doi:10.1002/adma.201901455
25. Lee, J.; Zhen, B.; Chua, S.-L.; Qiu, W.; Joannopoulos, J.; Soljacic, M.; Shapira, O. *Phys. Rev. Lett.* **2012,** *109,* 067401. doi:10.1103/physrevlett.109.067401
26. Yang, Y.; Peng, C.; Liang, Y.; Li, Z.; Noda, S. *Phys. Rev. Lett.* **2014,** *113,* 037401. doi:10.1103/physrevlett.113.037401
27. Mocella, V.; Romano, S. *Phys. Rev. B* **2015,** *92,* 155117. doi:10.1103/physrevb.92.155117
28. Yoon, J. W.; Song, S. H.; Magnusson, R. *Sci. Rep.* **2015,** *5,* 18301. doi:10.1038/srep18301
29. Wu, F.; Wu, J.; Guo, Z.; Jiang, H.; Sun, Y.; Li, Y.; Ren, J.; Chen, H. *Phys. Rev. Appl.* **2019,** *12,* 014028. doi:10.1103/physrevapplied.12.014028
30. Bonaccorso, F.; Sun, Z.; Hasan, T.; Ferrari, A. C. *Nat. Photonics* **2010,** *4,* 611–622. doi:10.1038/nphoton.2010.186

31. Grigorenko, A. N.; Polini, M.; Novoselov, K. S. *Nat. Photonics* **2012,** *6,* 749–758. doi:10.1038/nphoton.2012.262
32. Bao, Q.; Loh, K. P. *ACS Nano* **2012,** *6,* 3677–3694. doi:10.1021/nn300989g
33. Zhan, T.; Han, D.; Hu, X.; Liu, X.; Chui, S.-T.; Zi, J. *Phys. Rev. B* **2014,** *89,* 245434. doi:10.1103/physrevb.89.245434
34. Meng, Y.; Zhang, R.-Y.; Zhang, Q.; Liu, Z.; Wu, X.; Xiao, J.; Xiang, H.; Han, D.; Wen, W. *J. Phys. D: Appl. Phys.* **2017,** *50,* 485101. doi:10.1088/1361-6463/aa9300
35. Koppens, F. H. L.; Chang, D. E.; García de Abajo, F. J. *Nano Lett.* **2011,** *11,* 3370–3377. doi:10.1021/nl201771h
36. Mak, K. F.; Sfeir, M. Y.; Wu, Y.; Lui, C. H.; Misewich, J. A.; Heinz, T. F. *Phys. Rev. Lett.* **2008,** *101,* 196405. doi:10.1103/physrevlett.101.196405
37. Liu, M.; Yin, X.; Ulin-Avila, E.; Geng, B.; Zentgraf, T.; Ju, L.; Wang, F.; Zhang, X. *Nature* **2011,** *474,* 64–67. doi:10.1038/nature10067
38. Thongrattanasiri, S.; Koppens, F. H. L.; García de Abajo, F. J. *Phys. Rev. Lett.* **2012,** *108,* 047401. doi:10.1103/physrevlett.108.047401
39. Alaee, R.; Farhat, M.; Rockstuhl, C.; Lederer, F. *Opt. Express* **2012,** *20,* 28017–28024. doi:10.1364/oe.20.028017
40. Sensale-Rodriguez, B.; Rafique, S.; Yan, R.; Zhu, M.; Protasenko, V.; Jena, D.; Liu, L.; Xing, H. G. *Opt. Express* **2013,** *21,* 2324–2330. doi:10.1364/oe.21.002324
41. Xia, F.; Mueller, T.; Lin, Y.-m.; Valdes-Garcia, A.; Avouris, P. *Nat. Nanotechnol.* **2009,** *4,* 839–843. doi:10.1038/nnano.2009.292
42. Christensen, J.; Manjavacas, A.; Thongrattanasiri, S.; Koppens, F. H. L.; García de Abajo, F. J. *ACS Nano* **2012,** *6,* 431–440. doi:10.1021/nn2037626
43. Midrio, M.; Galli, P.; Romagnoli, M.; Kimerling, L. C.; Michel, J. *Photonics Res.* **2014,** *2,* A34–A40. doi:10.1364/prj.2.000a34
44. Bao, Q.; Zhang, H.; Wang, B.; Ni, Z.; Lim, C. H. Y. X.; Wang, Y.; Tang, D. Y.; Loh, K. P. *Nat. Photonics* **2011,** *5,* 411–415. doi:10.1038/nphoton.2011.102
45. Rizza, C.; Palange, E.; Ciattoni, A. *Photonics Res.* **2014,** *2,* 121–125. doi:10.1364/prj.2.000121
46. Fan, Y.; Zhang, F.; Zhao, Q.; Wei, Z.; Li, H. *Opt. Lett.* **2014,** *39,* 6269–6272. doi:10.1364/ol.39.006269
47. Piper, J. R.; Fan, S. *ACS Photonics* **2014,** *1,* 347–353. doi:10.1021/ph400090p
48. Zheng, G.; Zhang, H.; Xu, L.; Liu, Y. *Opt. Lett.* **2016,** *41,* 2274–2277. doi:10.1364/ol.41.002274
49. Lu, H.; Gan, X.; Jia, B.; Mao, D.; Zhao, J. *Opt. Lett.* **2016,** *41,* 4743–4746. doi:10.1364/ol.41.004743
50. Wang, X.; Jiang, X.; You, Q.; Guo, J.; Dai, X.; Xiang, Y. *Photonics Res.* **2017,** *5,* 536–542. doi:10.1364/prj.5.000536
51. Zhang, S.; Zhang, Y.; Ma, K. *Sci. Rep.* **2015,** *5,* 13049. doi:10.1038/srep13049
52. Wang, X.; Duan, J.; Chen, W.; Zhou, C.; Liu, T.; Xiao, S. *Phys. Rev. B* **2020,** *102,* 155432. doi:10.1103/physrevb.102.155432
53. Zeng, T.; Liu, G.; Wang, L.; Lin, Q. *Opt. Express* **2021,** *29,* 40177–40186. doi:10.1364/oe.446072
54. Wu, F.; Liu, D.; Xiao, S. *Opt. Express* **2021,** *29,* 41975–41989. doi:10.1364/oe.446270
55. Gusynin, V. P.; Sharapov, S. G.; Carbotte, J. P. *Phys. Rev. Lett.* **2006,** *96,* 256802. doi:10.1103/physrevlett.96.256802
56. Gan, C. H.; Chu, H. S.; Li, E. P. *Phys. Rev. B* **2012,** *85,* 125431. doi:10.1103/physrevb.85.125431
57. Moharam, M. G.; Grann, E. B.; Pommet, D. A.; Gaylord, T. K. *J. Opt. Soc. Am. A* **1995,** *12,* 1068–1076. doi:10.1364/josaa.12.001068
58. Lalanne, P.; Morris, G. M. *J. Opt. Soc. Am. A* **1996,** *13,* 779–784. doi:10.1364/josaa.13.000779
59. Hao, J.; Zhou, L.; Qiu, M. *Phys. Rev. B* **2011,** *83,* 165107. doi:10.1103/physrevb.83.165107
60. Zhang, Y.; Liu, W.; Li, Z.; Li, Z.; Cheng, H.; Chen, S.; Tian, J. *Opt. Lett.* **2018,** *43,* 1842–1845. doi:10.1364/ol.43.001842
61. Gong, Y.; Liu, X.; Li, K.; Huang, J.; Martinez, J. J.; Rees-Whippey, D.; Carver, S.; Wang, L.; Zhang, W.; Duan, T.; Copner, N. *Phys. Rev. B* **2013,** *87,* 205121. doi:10.1103/physrevb.87.205121

License and Terms

BEILSTEIN JOURNAL OF NANOTECHNOLOGY

Ideal Kerker scattering by homogeneous spheres: the role of gain or loss

Qingdong Yang[1], Weijin Chen[1], Yuntian Chen[*1,2] and Wei Liu[*3]

Full Research Paper

Open Access

Address:
[1]School of Optical and Electronic Information, Huazhong University of Science and Technology, Wuhan, Hubei 430074, P. R. China, [2]Wuhan National Laboratory for Optoelectronics, Huazhong University of Science and Technology, Wuhan, Hubei 430074, P. R. China and [3]College for Advanced Interdisciplinary Studies, National University of Defense Technology, Changsha, Hunan 410073, P. R. China

Email:
Yuntian Chen[*] - yuntian@hust.edu.cn; Wei Liu[*] - wei.liu.pku@gmail.com

* Corresponding author

Keywords:
gain and loss; Kerker scattering; Mie particle

Beilstein J. Nanotechnol. **2022,** *13,* 828–835.
https://doi.org/10.3762/bjnano.13.73

Received: 13 May 2022
Accepted: 21 July 2022
Published: 24 August 2022

This article is part of the thematic issue "Physics and optical applications of all-dieletric nanostructures".

Guest Editor: Z. Han

Abstract

We investigate how the optical gain or loss (characterized by isotropic complex refractive indexes) influence the ideal Kerker scattering of exactly zero backward scattering. It was previously shown that, for non-magnetic homogeneous spheres with incident plane waves, either gain or loss prohibit ideal Kerker scattering, provided that only electric and magnetic multipoles of a specific order are present and contributions from other multipoles can all be made precisely zero. Here we reveal that, when two multipoles of a fixed order are perfectly matched in terms of both phase and magnitude, multipoles of at least the next two orders cannot possibly be tuned to be all precisely zero or even perfectly matched, and consequently cannot directly produce ideal Kerker scattering. Moreover, we further demonstrate that, when multipoles of different orders are simultaneously taken into consideration, loss or gain can serve as helpful rather than harmful contributing factors, for the elimination of backward scattering.

Introduction

The original Kerker scattering of zero backward scattering was first proposed for homogeneous magnetic spheres with equal electric permittivity and magnetic permeability $\varepsilon = \mu$ [1]. This proposal had not attracted much attention for a long time, mainly due to the scarcity of magnetic materials, especially at the high-frequency spectral regimes. In the past decade, thanks to the explosive developments of metamaterials and metasurfaces, the underlying core concept of optically induced magnetism in non-magnetic structures has invigorated and completely transformed Kerker's original proposal (see the reviews [2-4]). The fusion of optically induced magnetism with Kerker scattering by high-index materials [5] has rendered new perspectives for photonic studies concerning not only scattering of individual particles or their finite clusters [6,7], but also of

extended periodic or aperiodic structures [2-4,8-14]. Moreover, this significantly broadened concept of Kerker scattering has rapidly penetrated into other disciplines of photonics, revealing hidden connections between seemingly unrelated concepts and demonstrations [15-23].

In the original proposal for homogenous spheres with $\varepsilon = \mu$, electric and magnetic multipoles of all orders are automatically perfectly matched in terms of both phase and magnitude [24], leading to ideal Kerker scattering of exactly zero backward scattering [1]. Nevertheless, for demonstrations relying on optically induced magnetism with non-magnetic structures ($\mu = 1$), it is rather challenging, if not impossible, to precisely match all multipoles simultaneously, ending up with only significantly suppressed but not exactly zero backward scattering [2-4]. Quite recently, Olmos-Trigo et al. revisited the simplest case of a non-magnetic isotropic and homogeneous sphere with incident plane waves and concluded that: (i) ideal zero backward scattering is achievable only for materials without gain or loss (characterized by real refractive indexes) [25], and (ii) extra gain or loss inhibit such ideal Kerker scattering. Besides the proven feasible perfect matching of electric and magnetic multipoles of one specific fixed order, the validity of the conclusion resides on the additional assumption that magnitudes of multipoles of all other orders can be simultaneously tuned to be perfectly zero. For general discussions of optical properties, such as scattering and absorption cross sections, it is physically legitimate to take into consideration only those dominant contributing multipole terms and drop other minor ones (such as in the widely adopted dipole approximation). While for the investigation into the extreme case of ideal zero backward scattering, those minor multipole terms cannot be simply discarded unless they are exactly zero or also perfectly matched in a similar fashion.

In this work we show that, despite the previously proven fact that multipoles of a fixed order can be perfectly matched in the absence of loss or gain [25], the contributions from multipoles of at least the next two orders cannot be simultaneously tuned to be all zero or perfectly matched. In other words, ideal Kerker scattering of exact zero backward scattering is not directly achievable through matching a pair of multipoles of one specific order only. We further reveal that when multipoles of different orders are all taken into consideration, loss or gain should be employed rather than avoided for the elimination of backward scattering. It is shown that, at the presence of multipoles of various orders, the absence of backward scattering can be obtained through tuning the refractive index on the complex plane, breaking the connection between zero backscattering and helicity conservation.

Results

Formulas and analysis of ideal Kerker scattering

For the scattering of incident linearly polarized plane waves (wavelength λ and angular wavenumber $k = 2\pi/\lambda$) by homogeneous non-magnetic spheres (isotropic refractive index m, radius R, and normalized geometric parameter $x = kR$), the scattered fields can be expanded into a series of electric and magnetic multipoles of order l ($l = 1$ corresponds to dipoles). They are characterized, respectively, by the complex Mie coefficients a_l and b_l [26,27]:

$$a_l = \frac{1}{2}\left(1 - e^{-2i\alpha_l}\right),\ b_l = \frac{1}{2}\left(1 - e^{-2i\beta_l}\right), \tag{1}$$

where α_l and β_l are complex phase angles (they are real when m is real). Those phase angles can be obtained through the following relations [26]:

$$\begin{aligned}\tan\alpha_l &= -\frac{S_l'(mx)S_l(x) - mS_l(mx)S_l'(x)}{S_l'(mx)C_l(x) - mS_l(mx)C_l'(x)},\\ \tan\beta_l &= -\frac{mS_l'(mx)S_l(x) - S_l(mx)S_l'(x)}{mS_l'(mx)C_l(x) - S_l(mx)C_l'(x)}.\end{aligned} \tag{2}$$

Here the prime $'$ denotes first-order derivative with respect to the entire argument in the bracket; $S_l(z) = zj_l(z)$ and $C_l(z) = -zy_l(z)$ are Riccati–Bessel functions; $j_l(z)$ and $y_l(z)$ are spherical Bessel functions of the first and second kinds.

With a_l and b_l obtained, the total scattering efficiency can be calculated through [26,27]:

$$Q_{\text{sca}} = \frac{2}{x^2}\sum_{l=1}^{\infty}(2l+1)\left(|a_l|^2 + |b_l|^2\right), \tag{3}$$

and the ideal Kerker scattering in terms of backward scattering efficiency Q_{b} can be expressed as [26,27]:

$$Q_{\text{b}} = \frac{1}{x^2}\left|\sum_{l=1}^{\infty}(2l+1)(-1)^l\left(a_l - b_l\right)\right|^2 = 0. \tag{4}$$

Equation 4 has an infinite set of possible solutions, and what is discussed [25] is actually the following very special scenario:

$$a_l = b_l \neq 0, \quad l = l_0, \tag{5}$$

$$a_l = b_l = 0, \quad l \neq l_0, \tag{6}$$

where l_0 is an arbitrary natural number and a pair of multipoles of order l_0 are perfectly matched as shown in Equation 5. The significant contribution from [25] is to prove rigorously that Equation 5 has a solution only when m is real, meaning that, at the presence of loss or gain, multipoles of the same order cannot be ideally matched. Despite this seminal contribution, there is a problem that in [25] it has not been discussed whether Equation 5 and Equation 6 are really compatible. Such discussions concerning compatibility are vitally important, since Equation 5 will not necessarily lead to ideal Kerker scattering of precise zero backscattering.

Mismatch among multipoles of three successive orders

In this section, we aim to prove that Equation 5 and Equation 6 are not exactly compatible, thus proving that Ideal Kerker scattering of exact zero backward scattering is actually inaccessible through matching multipoles of a specific order only. For all our following discussions, the obviously trivial scenario of $m = 1$ (we assume that the background medium is air of index 1 throughout our study) or $R = 0$ is excluded. For another special case of zero index $m = 0$, the Mie coefficients can be simplified as (as $m \to 0$) [26,27]:

$$a_l = \frac{S_l(x)}{T_l(x)}, \; b_l = \frac{S_l'(x) S_l(mx)}{T_l'(x) S_l(mx)}, \tag{7}$$

where $T_l(x) = x h_n^{(1)}(x)$, and $h_n^{(1)}(x)$ is a spherical Hankel function of the first kind. Since $S_l(mx) \to 0$ when $m \to 0$, we get a definite a_l but indefinite b_l (L'Hôpital's rule will not help to make b_l definite, since the zero term in the numerator and denominator is the same [28]). So it has been proved that for $m = 0$, there are no definite scattering properties for ideally monochromatic plane waves. Physical investigations can be implemented only after considering simultaneously the dispersion of the index and the spectrum of the incident waves. Consequently, the zero-index scenario is also excluded in the following analysis.

It has been rigorously proved that the solutions of Equation 5 satisfy either of the following equations:

$$S_{l_0}(mx) = 0, \tag{8}$$

$$S_{l_0}'(mx) = 0, \tag{9}$$

which do not have a common solution according to the Brauer–Siegel theorem [29,30]. Similarly, to prove that then multipoles of all other orders ($l \neq l_0$) cannot all be perfectly matched (of which that other multipoles cannot be tuned to be all zero is merely a special scenario), it is more than sufficient to prove that there exists one multipole order l_1 ($l_1 \neq l_0$) for which:

$$S_{l_1}(mx) \cdot S_{l_1}'(mx) \neq 0. \tag{10}$$

Obviously, Equation 10 ensures that $a_{l_1} \neq b_{l_1}$, meaning that Equation 6 cannot be simultaneously met.

According to the following recurrence relations of Riccati–Bessel functions [29]:

$$S_{l_0+1}'(mx) = -\frac{l_0+1}{mx} S_{l_0+1}(mx) + S_{l_0}(mx), \tag{11}$$

$$S_{l_0}'(mx) = \frac{l_0+1}{mx} S_{l_0}(mx) - S_{l_0+1}(mx), \tag{12}$$

(i) when $S_{l_0}(mx) = 0$ and $S_{l_0}'(mx) \neq 0$: According to Equation 12, we obtain $S_{l_0+1}(mx) \neq 0$. This together with Equation 11 leads to $S_{l_0+1}'(mx) \neq 0$. As a result, Equation 10 is satisfied at least for $l_1 = l_0 + 1$, securing that $a_{l_0+1} \neq b_{l_0+1}$.

(ii) When $S_{l_0}(mx) \neq 0$ and $S_{l_0}'(mx) = 0$: Also, according to Equation 12, we get $S_{l_0+1}(mx) \neq 0$. Nevertheless, according to Equation 11, $S_{l_0+1}'(mx) = 0$ if the following conditions can be met:

$$S_{l_0+1}(mx) = \pm S_{l_0}(mx), l_0 + 1 = \pm mx. \tag{13}$$

Nevertheless, following the same logic, extending the multipole matching to the next order $l_0 + 2$ requires:

$$S_{l_0+2}(mx) = \pm S_{l_0+1}(mx), l_0 + 2 = \pm mx. \tag{14}$$

It is quite obvious that Equation 13 and Equation 14 can not be simultaneously satisfied, that is, mx cannot be both $\pm(l_0 + 1)$ and $\pm(l_0 + 2)$, and, thus, multipole mismatch happens at least for $l_1 = l_0 + 2$: $a_{l_0+2} \neq b_{l_0+2}$.

The arguments above, consistent with a recent study [30], confirm that when a multipole of a specific order l_0 is perfectly matched in a nontrivial way, Equation 5, the scattering contributions from multipoles of at least the next two successive

orders (l_0 + 1 and l_0 + 2) cannot be simultaneously tuned to be zero or matched. In other words, perfect matching of multipoles of one specific order does not guarantee ideal zero backward scattering.

Effects of gain or loss on ideal Kerker scattering: non-resonant regimes

We show in Figure 1 two scenarios where the electric and magnetic dipoles (ED and MD) are perfectly matched in non-resonant spectra regimes. The scattering efficiency spectra (scattering efficiency Q_{sca} as a function of $x = kR$) for a homogeneous sphere (m = 4.1) are shown in Figure 1a, where both total scattering and the contributions from different multipoles (dipoles and electric and magnetic quadrupoles: EQ and MQ) are included. This is actually the case studied in detail in [25]. The ED and MD are perfectly matched at $x_\mathbf{A}$ = 0.6684, where $S_1'(mx_\mathbf{A}) = 0$. As argued in the last section, at $x_\mathbf{A}$, scattering from multipoles of higher orders is not exactly zero (see Figure 1b, which shows an enlarged part of the spectra close to $x_\mathbf{A}$ in logarithmic scale), though they are much smaller than those of dipoles. For explorations of general properties like scattering and absorption cross sections, it is fine to drop those quadrupole terms and to keep the dipole terms only. Nevertheless, for the study of the extreme case of ideal Kerker scattering, simply discarding those higher-order terms cannot be justified and could even lead to inaccurate conclusions.

To verify the claim above, we show in Figure 1c the dependence of the backward scattering efficiency Q_b at $x_\mathbf{A}$ on the imaginary part of refractive index Im(m); the real part of m is fixed at Re(m) = 4.1. Im(m) > 0 and Im(m) < 0 correspond to loss and gain, respectively. Here two sets of spectra are shown, for which either only dipoles or multipoles of all orders are taken into consideration. It is clear from Figure 1c that, when only dipoles are considered, ideal Kerker scattering is achieved when m is real, and any extra loss or gain would inhibit such scattering, as is the major conclusion of [25]. In sharp contrast, when all multipoles are considered, ideal Kerker scattering is not accessible at the perfect matching point of dipoles anymore. Moreover, as shown in Figure 1c, extra loss can be employed to further suppress the backward scattering, serving as a friend rather than a foe for the Kerker scattering. Another scenario of perfect dipole matching at $x_\mathbf{B}$ = 1.0472 for m = 4.29 is summarized in Figure 1d–f, for which the other perfect matching condition is satisfied, that is $S_1(mx_\mathbf{A}) = 0$. Here the effects of higher-order multipoles are even more pronounced (see Figure 1f) since the magnitudes of dipoles and higher multipoles are comparable (see Figure 1e.

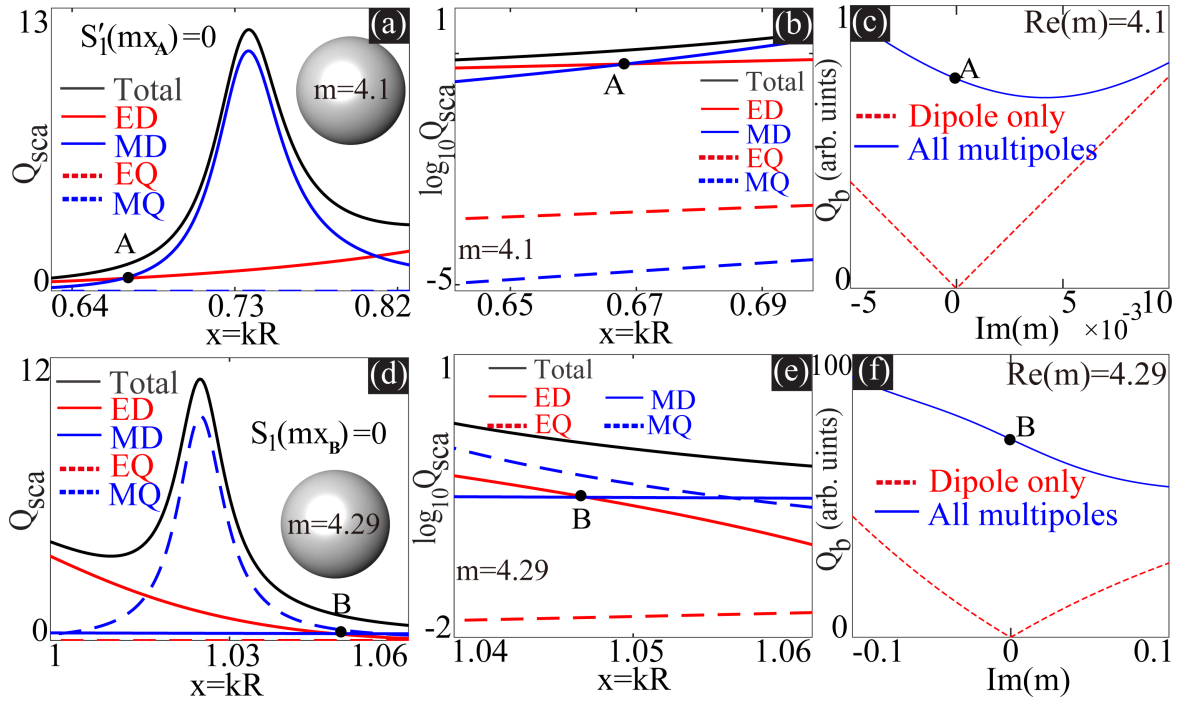

Figure 1: Scattering spectra (both total scattering and the contributions from different multipoles are included) are shown in (a) and (b) for m = 4.1, and in (d) and (e) for m = 4.29. Here, (b) and (e) are sections of (a) and (b), respectively, which are close to the dipole matching points and enlarged for clarity. For each scenario, there is a indicated point ($x_\mathbf{A} \approx 0.6684$ and $x_\mathbf{B} \approx 1.0472$) where the dipoles are perfectly matched. (c, f) Dependence of Q_b on Im(m), at $x_\mathbf{A}$ with fixed Re(m) = 4.1 and at $x_\mathbf{B}$ with fixed Re(m) = 4.29, respectively. In (c) and (f), two sets of results are shown, considering only dipoles or all multipoles, respectively.

Effects of gain or loss on ideal Kerker scattering: resonant regimes

In the last section, we discussed only the perfect dipole matching at the non-resonant regimes, where not only the backward scattering is suppressed, but also the overall scattering is small. Such scattering is of very limited significance, since what is widely required in photonics is suppressed backward scattering accompanied by large total scattering [2-4]. In this section, we move to the resonant regimes where the dipoles can be perfectly matched. Two such scenarios are summarized in Figure 2, where the conditions of $S_1(mx_{\mathbf{C}}) = 0$ and $S_1'(mx_{\mathbf{D}}) = 0$ are satisfied, in Figure 2a–c with $x_{\mathbf{C}} \approx 2.7366$, $m = 5.14$, and in Figure 2d–f with $x_{\mathbf{D}} \approx 4.4123$, and $m = 2.83$), respectively. In Figure 2, besides the scattering spectra (Figure 2a,d) and dependence of Q_b on Im(m) (Figure 2b,e), we show also the two-dimensional (2D) scattering patterns (in the plane parallel to both the incident and polarization directions of the independent plane waves) at the dipole matching points (Figure 2c,f).

As indicated by the scattering spectra, the scattering by the higher-order multipoles is rather strong, which ruins the ideal Kerker scattering (see Figure 2b,e) and makes the overall patterns considering all multipoles (solid lines of Figure 2c,f) contrastingly different from those of matched dipoles only (dashed lines of Figure 2c,f). Similar to what is shown in Figure 1, when all multipoles are considered, extra loss can be employed to further suppress the backward scattering, serving as a constructive rather than a destructive factor for demonstrations of Kerker scattering.

Kerker scattering without multipole matching of any specific order

We have confirmed in the last sections, by both mathematical analysis and numerical calculations, that perfect matching of multipoles of a specific order does not necessarily produce ideal Kerker scattering due to non-negligible higher-order multipoles. Moreover, those higher-order terms would make the extra gain or loss a constructive factor for further suppression of the backward scattering. Now we come back to Equation 4, the solution of which does not really require multipole matching of any specific order (such as those shown in Equation 5 and Equation 6), but can be obtained through fully destructive interferences among multipoles of several orders along the backward direction. Such an effect is also termed as "generalized Kerker effect", originating from interferences among multipoles of different orders [4,31-34]. Generally speaking, to obtain zero

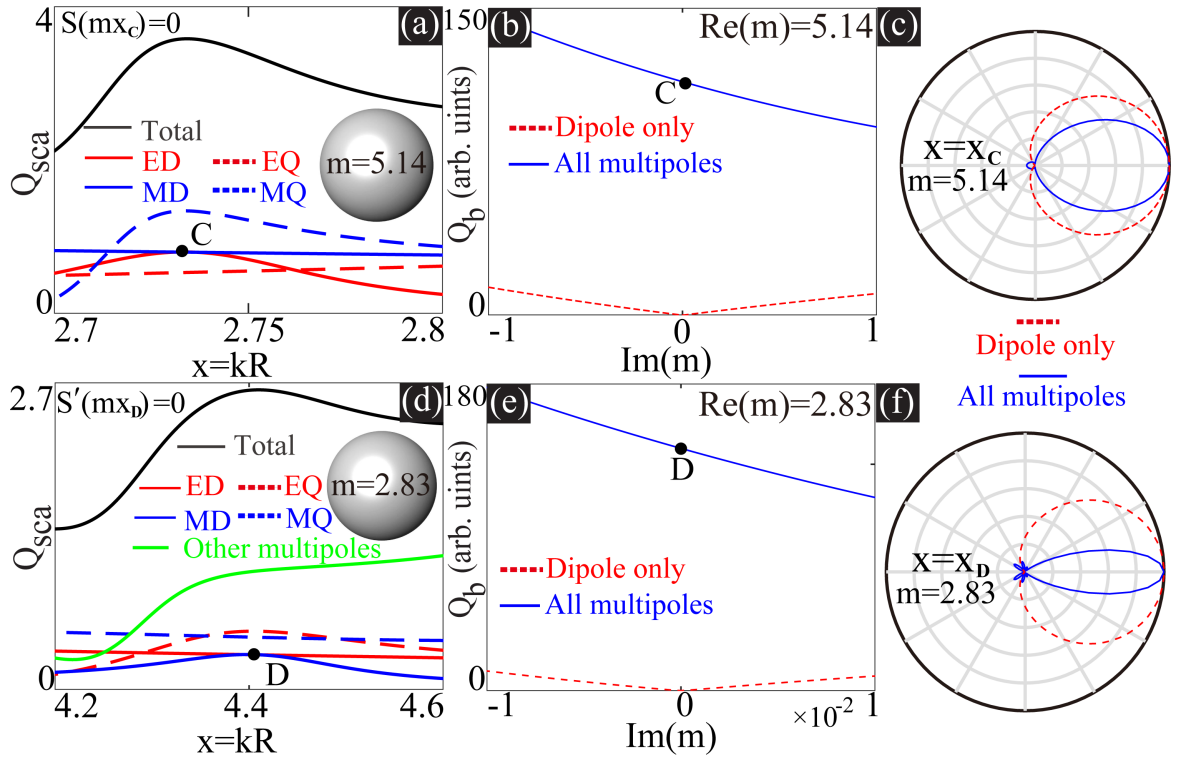

Figure 2: Scattering spectra are shown in (a) for $m = 5.14$ and in (d) for $m = 2.83$. For each scenario, there is an indicated point ($x_{\mathbf{C}} \approx 2.7366$ and $x_{\mathbf{D}} \approx 4.4123$) where the dipoles are perfectly matched. (b, e) Dependence of Q_b on Im(m) at $x_{\mathbf{C}}$ with fixed Re(m) = 5.14 and at $x_{\mathbf{D}}$ with fixed Re(m) = 2.83, respectively. (c, f) The 2D angular scattering patterns (in the plane parallel to both polarization and incident directions) at $x_{\mathbf{C}}$ with $m = 5.14$ and at $x_{\mathbf{D}}$ with $m = 2.83$, respectively. In (b, c) and (e, f) two sets of results are shown, considering only dipoles or all multipoles, respectively.

backward scattering with complete destructive interferences among multipoles, at least two multipoles of opposite parities are needed. This could be a pair of multipoles of the same order (such as ED and MD), or two multipoles of different orders (such as ED and EQ, or MD and MQ), or more than two multipoles that are not of the same parity [4,31]. For further confirmation, we show two such scenarios with loss or gain in Figure 3, where Kerker scattering is observed, in Figure 3a,b ($x_{\mathbf{E}} \approx 1.9591$, $m = 1.1875 + 0.1i$), and in Figure 3d,e ($x_{\mathbf{F}} \approx 1.7492$ for $m = 1.275 - 4.225i$), respectively. Figure 3a,b shows that there is no non-trivial perfect multipole matching ($a_l = b_l \neq 0$) at the indicated positions, despite which the Kerker scattering can still be achieved (see Figure 3b,e at $x_{\mathbf{E}}$ and $x_{\mathbf{F}}$). Moreover, the dependence of Q_b on Im(m) (Figure 3b,e) can confirm that the selected loss or gain is vitally important for such achievement, as a little detuning from them would immediately ruin the Kerker scattering. For both scenarios, it is quite obvious that to fix the index to be real is actually harmful for the suppression of backward scattering.

It has been rigorously proved that n-fold ($n \geq 3$) rotation symmetry together with helicity conservation would automatically guarantee ideal Kerker scattering of zero backward scattering [22,35]. For homogenous sphere scattering with incident plane waves, the rotation symmetry is secured ($n = \infty$) and the helicity conservation requires the multipole matching of all orders. Consequently, Kerker scattering obtained through perfect matching of multipoles at each order are inextricably connected through helicity conservation, as is confirmed in [25]. Nevertheless, we have shown in the last section that Kerker scattering is also achievable without multipole matching of any specific order, for which it is expected that the connection between Kerker scattering and helicity conservation would be broken. To confirm this, we further show the dependence of the helicity conservation factor $\mathbb{H}$ on Im(m) in Figure 3c,f. Here $\mathbb{H}$ is defined as [25,36]:

$$\mathbb{H} = \frac{\sum_{l=1}^{\infty}(2l+1)\,\mathrm{Re}\left\{a_l b_l^*\right\}}{\sum_{l=1}^{\infty}(l+1/2)\left(|a_l|^2+|b_l|^2\right)}. \tag{15}$$

Here $\mathbb{H} = 1$ corresponds to ideal helicity conservation, which means that for incident circularly polarized plane waves, the waves scattered along all directions are also circularly polarized of the same handedness (including the special case of zero scattering) [17,22,37,38]. A comparison between Figure 3c,f and Figure 3b,e can confirm that there is no connection between the Kerker scattering and helicity conservation, since $\mathbb{H}$

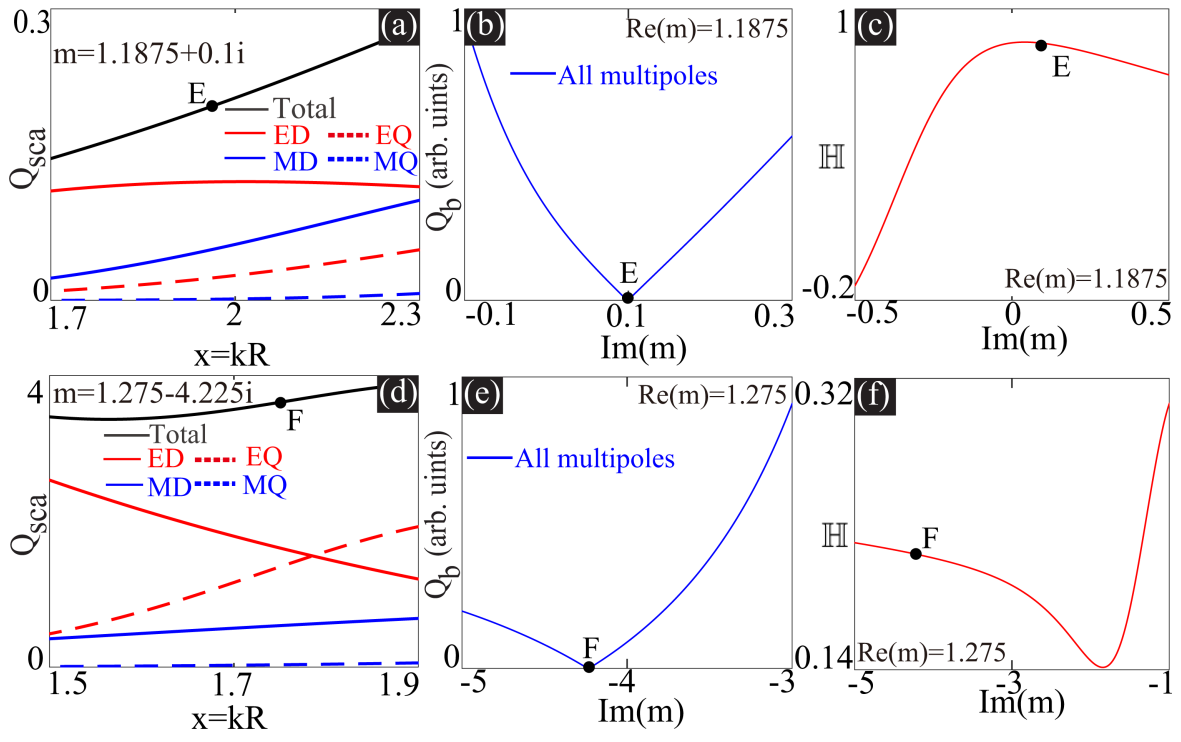

Figure 3: Scattering spectra are shown in (a) for $m = 1.1875 + 0.1i$ (with loss) and in (d) for $m = 1.275 - 4.225i$ (with gain). For each scenario, there is an indicated point ($x_{\mathbf{E}} \approx 1.9591$ and $x_{\mathbf{F}} \approx 1.7492$) where the backward scattering is eliminated, as confirmed in (b) and (e). Dependence of Q_b (b, e) and $\mathbb{H}$ (c, f) on Im(m), at $x_{\mathbf{E}}$ with fixed Re(m) = 1.1875 and at $x_{\mathbf{F}}$ with fixed Re(m) = 1.275.

is far from unity at the indicated Kerker scattering points ($\mathbb{H}_{\mathbf{E}} = 0.857$, $\mathbb{H}_{\mathbf{F}} = 0.2115$). In other words, rotation symmetry and helicity conservation lead to zero backward scattering, while rotation symmetry and zero backward scattering does not necessarily imply helicity conservation.

Discussion

There are several significant points worth emphasizing at the end: (i) For numerical demonstrations of perfect multipole matching, we discuss only dipoles while the principles revealed are applicable for multipoles of any order. (ii) In this study, we only discuss Kerker scattering of zero backward scattering (first Kerker scattering). For the second Kerker scattering of zero forward scattering, despite the inevitable involvement of gain materials as required by optical theorem, multipoles of various order rather than a specific order should be taken into considerations simultaneously, as has been implemented in this work. (iii) Is ideal Kerker scattering of exact zero backward scattering achievable, in a rigorously mathematical sense, with homogenous non-magnetic spheres? The answer is: We do not know. It is well known that for arbitrary algebraic equations of order L,

$$\sum_{l=0}^{L} c_l x^{L-l} = 0,$$

for which L is a finite natural number and c_l are complex constant coefficients, the fundamental theorem of algebra secures that there is at least one solution on the complex x-plane [28]. Nevertheless, Equation 4 is a transcendental rather than an algebraic equation, of which the existence of exact solution on the complex plane is not definite. Such a transcendental equation can be only tackled through numerical analysis and, thus, numerical errors make it impossible to decide if the Kerker scattering demonstrated in Figure 3 is ideal or not in a mathematical sense. (iv) If an exact solution of Equation 4 exists, the chances of this solution being complex are much higher than it being purely real (real axes cover a tiny part of the complex plane). If an exact solution does not exist, the backward scattering is minimized more probably at complex arguments rather than at purely real ones. As a result, gain or loss are definitely helpful rather than harmful for the realizations of ideal Kerker scattering or suppression of backward scattering. (v) Discussing the exact solution of Equation 4 (and thus ideal Kerker scattering) is interesting and meaningful only mathematically. From a physical perspective, such an exploration is of very little significance, if not of no significance at all. This is because for realistic observations, there is no absolute boundary between exactly zero and approximately zero, which highly depends on the resolutions of different equipments. Moreover, when the scattering intensity gets smaller and smaller, the optical regime we study will shift from wave optics to quantum optics, where the quantum fluctuations would play a non-negligible role [39]. Then wave optics and, thus, Equation 4 itself breaks down and it becomes meaningless to discuss its exact solution.

Conclusion

We have proved that perfectly matching electric and magnetic multipoles of a specific order do not necessarily produce ideal Kerker scattering of exact zero backward scattering. This is because no matter how small the contributions from other multipoles are, they can never be made to be all zero or perfectly matched. In other words, to obtain zero backward scattering, we cannot just consider multipoles of a specific order. Instead we need to consider all contributing ones that are not exactly zero. It is further demonstrated that when multipoles of various order are simultaneously considered, loss or gain can be employed for suppression of backward scattering, serving as beneficial rather than detrimental contributions for the realization of ideal Kerker scattering. When Kerker scattering is achieved through the destructive interference among multipoles of several orders in the backward direction, rather than perfect multipole matching of each order, it is not synonymous with helicity conservation any more.

Acknowledgements

W. L. thanks Dr. Jorge Olmos-Trigo for his comments on this work.

Funding

The following sources of funding are acknowledged: National Natural Science Foundation of China (Grant No. 11874026, and 11874426), and the Outstanding Young Researcher Scheme of National University of Defense Technology, and all authors thank the generous research funding for financial support.

ORCID® iDs

Qingdong Yang - https://orcid.org/0000-0002-3870-3567
Wei Liu - https://orcid.org/0000-0002-7067-6239

Preprint

A non-peer-reviewed version of this article has been previously published as a preprint: https://doi.org/10.48550/arXiv.2009.04939

References

1. Kerker, M.; Wang, D.-S.; Giles, C. L. *J. Opt. Soc. Am.* **1983,** *73,* 765. doi:10.1364/josa.73.000765
2. Jahani, S.; Jacob, Z. *Nat. Nanotechnol.* **2016,** *11,* 23–36. doi:10.1038/nnano.2015.304
3. Kuznetsov, A. I.; Miroshnichenko, A. E.; Brongersma, M. L.; Kivshar, Y. S.; Luk'yanchuk, B. *Science* **2016,** *354,* aag2472. doi:10.1126/science.aag2472
4. Liu, W.; Kivshar, Y. S. *Opt. Express* **2018,** *26,* 13085–13105. doi:10.1364/oe.26.013085

5. Tribelsky, M. I.; Miroshnichenko, A. E. *Phys. Rev. A* **2016,** *93,* 053837. doi:10.1103/physreva.93.053837
6. Geffrin, J. M.; García-Cámara, B.; Gómez-Medina, R.; Albella, P.; Froufe-Pérez, L. S.; Eyraud, C.; Litman, A.; Vaillon, R.; González, F.; Nieto-Vesperinas, M.; Sáenz, J. J.; Moreno, F. *Nat. Commun.* **2012,** *3,* 1171. doi:10.1038/ncomms2167
7. Fu, Y. H.; Kuznetsov, A. I.; Miroshnichenko, A. E.; Yu, Y. F.; Luk'yanchuk, B. *Nat. Commun.* **2013,** *4,* 1527. doi:10.1038/ncomms2538
8. Person, S.; Jain, M.; Lapin, Z.; Sáenz, J. J.; Wicks, G.; Novotny, L. *Nano Lett.* **2013,** *13,* 1806–1809. doi:10.1021/nl4005018
9. Smirnova, D.; Kivshar, Y. S. *Optica* **2016,** *3,* 1241–1255. doi:10.1364/optica.3.001241
10. Chen, H.-T.; Taylor, A. J.; Yu, N. *Rep. Prog. Phys.* **2016,** *79,* 076401. doi:10.1088/0034-4885/79/7/076401
11. Staude, I.; Schilling, J. *Nat. Photonics* **2017,** *11,* 274–284. doi:10.1038/nphoton.2017.39
12. Kruk, S.; Kivshar, Y. *ACS Photonics* **2017,** *4,* 2638–2649. doi:10.1021/acsphotonics.7b01038
13. Yang, Z.-J.; Jiang, R.; Zhuo, X.; Xie, Y.-M.; Wang, J.; Lin, H.-Q. *Phys. Rep.* **2017,** *701,* 1–50. doi:10.1016/j.physrep.2017.07.006
14. Ding, F.; Pors, A.; Bozhevolnyi, S. I. *Rep. Prog. Phys.* **2018,** *81,* 026401. doi:10.1088/1361-6633/aa8732
15. Chen, W.; Chen, Y.; Liu, W. *Phys. Rev. Lett.* **2019,** *122,* 153907. doi:10.1103/physrevlett.122.153907
16. Sadrieva, Z.; Frizyuk, K.; Petrov, M.; Kivshar, Y.; Bogdanov, A. *Phys. Rev. B* **2019,** *100,* 115303. doi:10.1103/physrevb.100.115303
17. Chen, W.; Yang, Q.; Chen, Y.; Liu, W. *ACS Omega* **2020,** *5,* 14157–14163. doi:10.1021/acsomega.0c01843
18. Poshakinskiy, A. V.; Poddubny, A. N. *Phys. Rev. X* **2019,** *9,* 011008. doi:10.1103/physrevx.9.011008
19. Alaee, R.; Gurlek, B.; Albooyeh, M.; Martín-Cano, D.; Sandoghdar, V. *Phys. Rev. Lett.* **2020,** *125,* 063601. doi:10.1103/physrevlett.125.063601
20. Ballantine, K. E.; Ruostekoski, J. *Phys. Rev. Lett.* **2020,** *125,* 143604. doi:10.1103/physrevlett.125.143604
21. Zhu, T.; Shi, Y.; Ding, W.; Tsai, D. P.; Cao, T.; Liu, A. Q.; Nieto-Vesperinas, M.; Sáenz, J. J.; Wu, P. C.; Qiu, C.-W. *Phys. Rev. Lett.* **2020,** *125,* 043901. doi:10.1103/physrevlett.125.043901
22. Fernandez-Corbaton, I. *Opt. Express* **2013,** *21,* 29885–29893. doi:10.1364/oe.21.029885
23. Yang, Q.; Chen, W.; Chen, Y.; Liu, W. *ACS Photonics* **2020,** *7,* 1830–1838. doi:10.1021/acsphotonics.0c00555
24. Lee, J. Y.; Miroshnichenko, A. E.; Lee, R.-K. *Phys. Rev. A* **2017,** *96,* 043846. doi:10.1103/physreva.96.043846
25. Olmos-Trigo, J.; Sanz-Fernández, C.; Abujetas, D. R.; Lasa-Alonso, J.; de Sousa, N.; García-Etxarri, A.; Sánchez-Gil, J. A.; Molina-Terriza, G.; Sáenz, J. J. *Phys. Rev. Lett.* **2020,** *125,* 073205. doi:10.1103/physrevlett.125.073205
26. van de Hulst, H. C. *Light Scattering by Small Particles;* John Wiley & Sons: New York, NY, USA, 1957.
27. Bohren, C. F.; Huffman, D. R. *Absorption and Scattering of Light by Small Particles;* John Wiley & Sons: Hoboken, NJ, USA, 1983. doi:10.1002/9783527618156
28. Aleksandrov, A. D.; Kolmogorov, A. N.; Lavrent'ev, M. A. *Mathematics: Its Content, Methods and Meaning;* Dover Publications: Mineola, NY, USA, 1999.
29. Watson, G. N. *A Treatise on the Theory of Bessel Functions,* 2nd ed.; Cambridge University Press: Cambridge, UK, 1995.
30. Olmos-Trigo, J.; Abujetas, D. R.; Sanz-Fernández, C.; Zambrana-Puyalto, X.; de Sousa, N.; Sánchez-Gil, J. A.; Sáenz, J. J. *Phys. Rev. Res.* **2020,** *2,* 043021. doi:10.1103/physrevresearch.2.043021
31. Liu, W. *Phys. Rev. Lett.* **2017,** *119,* 123902. doi:10.1103/physrevlett.119.123902
32. Luk'yanchuk, B.; Paniagua-Domínguez, R.; Kuznetsov, A. I.; Miroshnichenko, A. E.; Kivshar, Y. S. *Philos. Trans. R. Soc., A* **2017,** *375,* 20160069. doi:10.1098/rsta.2016.0069
33. Tribelsky, M. I.; Miroshnichenko, A. E. *Phys. Rev. A* **2016,** *93,* 053837. doi:10.1103/physreva.93.053837
34. Luk'yanchuk, B. S.; Voshchinnikov, N. V.; Paniagua-Domínguez, R.; Kuznetsov, A. I. *ACS Photonics* **2015,** *2,* 993–999. doi:10.1021/acsphotonics.5b00261
35. Yang, Q.; Chen, W.; Chen, Y.; Liu, W. *Laser Photonics Rev.* **2021,** *15,* 2000496. doi:10.1002/lpor.202000496
36. Olmos-Trigo, J.; Sanz-Fernández, C.; Bergeret, F. S.; Sáenz, J. J. *Opt. Lett.* **2019,** *44,* 1762–1765. doi:10.1364/ol.44.001762
37. Fernandez-Corbaton, I.; Zambrana-Puyalto, X.; Tischler, N.; Vidal, X.; Juan, M. L.; Molina-Terriza, G. *Phys. Rev. Lett.* **2013,** *111,* 060401. doi:10.1103/physrevlett.111.060401
38. Yang, Q.; Chen, W.; Chen, Y.; Liu, W. *Phys. Rev. B* **2020,** *102,* 155427. doi:10.1103/physrevb.102.155427
39. Berry, M. V. Much Ado about Nothing: Optical Distortion Lines (Phase Singularities, Zeros, and Vortices). In *Proc. SPIE 3487,* International Conference on Singular Optics, Aug 3, 1998; Soskin, M. S., Ed.; International Society for Optics and Photonics, 1998; pp 1–5. doi:10.1117/12.317693

License and Terms

BEILSTEIN JOURNAL OF NANOTECHNOLOGY

Numerical study on all-optical modulation characteristics of quantum cascade lasers

Biao Wei, Haijun Zhou, Guangxiang Li and Bin Tang*

Full Research Paper

Open Access

Address:
Key Laboratory of Optoelectronic Technology & Systems, Ministry of Education, Chongqing University, Chongqing 400044, China

Email:
Bin Tang* - Tangbin8@sina.com

* Corresponding author

Keywords:
all-optical modulation; dielectric nanostructures; high refractive index materials; numerical study; quantum cascade lasers

Beilstein J. Nanotechnol. **2022,** *13,* 1011–1019.
https://doi.org/10.3762/bjnano.13.88

Received: 29 May 2022
Accepted: 13 September 2022
Published: 23 September 2022

This article is part of the thematic issue "Physics and optical applications of all-dieletric nanostructures".

Guest Editor: Z. Han

Abstract

To explain the phenomenon of all-optical modulation of quantum cascade laser (QCL), and explore the physics in QCL's gain medium which consists of multiple of dielectric nanostructures with high refractive index under light injection, we modified the 1½-period model to calculate values of electron population and lifetime in each subband which is separated by the nanostructures, optical gain, current and number of photons in the cavity of a mid-infrared QCL modulated with near-infrared optical injection. The results were consistent with an experiment, where the injected light increases the electron population and lifetime, but does not affect the optical gain obviously. Our study can be helpful for optimizing its use and dielectric nanostructure design.

Introduction

The quantum cascade laser (QCL) was invented nearly 30 years ago [1], and its cavity consists of multiple nanostructures, which are grown by molecular beam epitaxy (MBE) [1]. It has been widely used in the fields of free space optical communication [2,3], gas detection [4,5], and biological research [6,7]. Because the QCL is a narrow linewidth and high-power laser working in the mid-infrared to terahertz band, it can cover most of the gas molecular-fingerprint absorption spectrum and atmospheric transmission window, and it will not damage organisms. Modulation of QCLs is an effective method of suppressing low-frequency noise and improving the signal-to-noise ratio. Various approaches to modulation have been reported, including thermal [8], electrical [9], acousto-optic [10], Faraday rotation effect spectroscopy [11], and all-optical methods [12]. The unipolar characteristics of QCLs provide them with unique advantages for all-optical modulation. All-optical modulation can avoid parasitic effects, and the modulation frequency can reach 60 GHz [13]. Moreover, all-optical modulation can directly alter the carrier distribution and is highly efficient. However, the mechanism of all-optical modulation is very com-

plex. If we could effectively describe all-optical modulation of QCLs by numerical simulation, it would be very helpful for optimizing its use and dielectric nanostructure design. Although there has been much research on all-optical modulation of QCLs, only optical injection locking [14] and quenching [15,16] can currently provide one-sided numerical support. Based on the classical 1½-period model of QCLs [17], a numerical calculation method for all-optical modulation of QCLs is proposed here. By considering the change of carrier distribution in the active region of a QCL caused by the injected light, the results of all-optical modulation experiments can be reasonably explained. These findings provide support for further research on all-optical modulation of QCLs.

Results and Discussion

Numerical approach

To examine the all-optical modulation of QCLs, we must consider the output characteristics of QCLs. In the four-level system, the carrier distribution is described by the full rate equations (FRE) [18] as Equations 1–4 shows, where n_0 is the cavity index, g_c is the gain cross section, c is the speed of light. Γ_P is the optical confinement factor per stage, α is the laser total loss. N_P the total number of stages, $1/\tau_{k,i}$ is the rate of electron scattered from subband k to subband i, $1/\tau_{sp}$ is the spontaneous emission rate of the upper laser subband, α is the cavity absorption coefficient, β is the rate of spontaneous emission getting into the laser modes, n_k is the k-th subband population, S is the photon population in the cavity, and the laser upper and lower subbands are denoted by Equation 4 and Equation 3, respectively. The numerical methods solving FRE are excellently recorded in [18]. By taking into account the effects of optical injection [19] and electron temperature [20,21], the full rate equation is modified to obtain a more accurate numerical simulation of the output characteristics of QCLs. In all-optical modulation, light directly illuminates the facet of the active region of the QCL. Injection of a large amount of energy will inevitably change the original energy balance and carrier distribution and, of course, generate heat. The injected light will excite the valence band electrons to transition to the conduction band and produce electron-hole pairs. The lifetimes of electrons and holes are quite different [22] and result in accumulation of holes, and then, in order to maintain electrical neutrality of the laser, the electrons in the current are added to the conduction band [23]. Moreover, the fluctuation of threshold current caused by the light injection is around tens of mA [19], which is much smaller than the threshold current. Therefore, all-optical modulation can only be achieved when the QCL works near or above the threshold. It is worth noting that, when the wavelength of the modulating light is close to the band gap of the active region of the QCL, most of the injected light energy excites the electrons in the valence band to transition to the conduction band and then to the upper laser subband, thereby increasing the power of the modulating light. However, with a decrease in the modulated laser wavelength, its energy becomes greater than the band gap between the valence band and the lower laser subband of the conduction band of the QCL active region, with the excess energy exciting the electrons to a higher energy level or high kinetic state (high kinetic state means high electron temperature) and generating heat through electron–electron and electron–lattice scattering, which suppresses the laser output. And such a compression can be explained by the hot electron backfilling effect [20,24,25], which is caused by an increase of the electron temperature. The electrons with high kinetic state increase the number of electrons in the lower laser subband by backfilling and inhibit the population inversion. As a result, the light output is suppressed.

$$\frac{dn_i}{dt} = -n_i \sum_{k\neq i} \frac{1}{\tau_{i,k}} + \sum_{k\neq i} \frac{n_k}{\tau_{k,i}} \tag{1}$$

$$\frac{dn_4}{dt} = -n_4 \sum_{k\neq 4} \frac{1}{\tau_{4,k}} + \sum_{k\neq 4} \frac{n_k}{\tau_{k,4}} - S\Gamma_P \frac{c}{n_0} g_c (n_4 - n_3) \tag{2}$$

$$\frac{dn_3}{dt} = -n_3 \sum_{k\neq 3} \frac{1}{\tau_{3,k}} + \sum_{k\neq 4} \frac{n_k}{\tau_{k,3}} + S\Gamma_P \frac{c}{n_0} g_c (n_4 - n_3) \tag{3}$$

$$\frac{dS}{dt} = S\left[N_P \Gamma_P \frac{c}{n_0} g_c (n_4 - n_3) - \frac{c}{n_0}\alpha \right] + N_P \beta \frac{n_4}{\tau_{sp}} \tag{4}$$

In this paper, we further modify the rate equation to facilitate a numerical study of the all-optical modulation of QCLs. A flow chart of the numerical calculations for the all-optical modulation of QCLs is shown in Figure 1. Here, we modify our numerical model in two cases. The first case is when modulating the laser wavelength to greater than the lower laser subband of the active region of the QCL. The injected laser will then not be able to excite the electrons in the valence band to the laser subband of the conduction band, and the transition of electrons in the conduction band will be affected by the electric field. Therefore, we can allocate all the photoexcited electrons to the conduction band, and obtain the electron number of each subband of the conduction band by solving the partial rate equations (PRE) [17]. Whether the scattering rate and electron population of each subband can be further calculated by the FRE is judged by whether or not the electrons of each subband converge. Numerical studies of the FRE involved here have been previously reported [18]. The second case is when the modulating laser wavelength is less than that of the lower laser subband of the active region of the QCL. The injected laser light may then excite the electrons to the laser subband or high

kinetic state, which requires correct allocation of the photoexcited electrons to each subband; the fluctuation of the electron temperature in the conduct band is an important parameter for characterizing this change. First, the photoexcited electrons are evenly distributed into each subband to complete the initial conditions for the calculations. Through multiple iterations during which the electron number of each subband converges, the electron distribution is approached by energy conservation and the hot electron backfilling effect which increase the lifetime of electrons in the lower laser energy level as described in Equation 11, and finally the scattering rate and number of electrons in each subband are obtained.

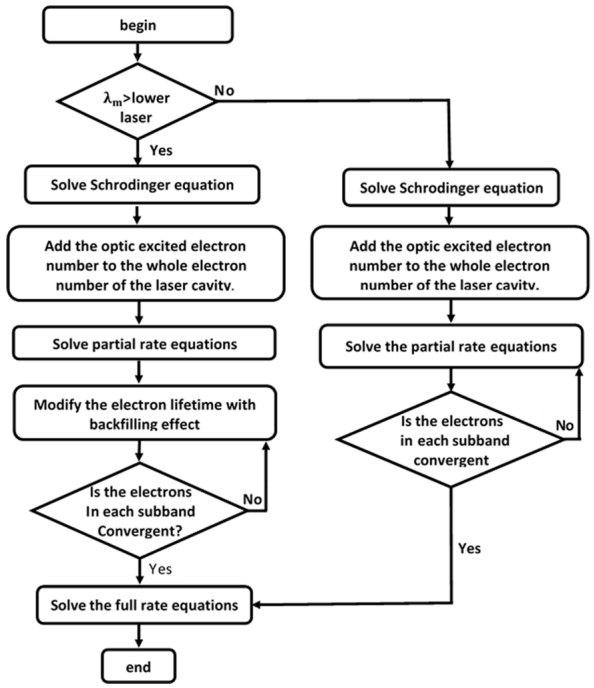

Figure 1: An algorithm for solving the scattering rate and electron distribution for each subband using all-optical modulation.

The number of photoexcited electrons, which is closely related to the number and area density of photons, forms the basis of the subsequent numerical calculation. When the modulated QCL is illuminated on the facet of its active region at an angle of 30°, almost all the laser energy is absorbed [19], so we disregard this loss, and the initial photoexcited electrons are generated from the valence band.

Furthermore, the number of photons produced during the hole lifetime τ_p can be described as:

$$n_t = \frac{P\tau_p\lambda_{inj}}{ch}, \tag{5}$$

where c is the speed of light, λ_{inj} is the wavelength of the injected light, h is Planck's constant, and P is the power of the modulated laser.

Then, the area density of photons is obtained as:

$$\rho = \frac{n_t}{lw} = \frac{P\tau_p\lambda_{inj}}{chlw}, \tag{6}$$

where l is the length and w is the width of the laser cavity. All these parameters are known except τ_p, and τ_p can be obtained from the experimental data in reference [19], which gives the relationship between $\Delta\lambda$ and injection power; $\Delta\lambda$ is the variation in laser wavelength λ caused by optical injection. The relationship between $\Delta\lambda$ and the refractive index n_0 can be described as

$$\Delta\lambda = \lambda\frac{\Delta n_0}{n_0}, \tag{7}$$

where Δn_0 is the variation in n_0.

We know that Δn_0 is induced by electron-hole pairs, and can be described by the following equation [12]:

$$\Delta n_0 = -\frac{e^2\lambda^2}{8\pi^2c^2\varepsilon_0 n_0}\left(\frac{N}{m_e} + \frac{P}{m_p}\right). \tag{8}$$

Combining Equations 2, 3 and 4, we obtain the following:

$$\Delta n_0 = -\frac{e^2\lambda^2}{8\pi^2c^2\varepsilon_0 n_0}\frac{P\tau_p\lambda_{inj}}{chlwh}\left(\frac{1}{m_e} + \frac{1}{m_p}\right), \tag{9}$$

which yields:

$$\tau_p = -\frac{\Delta\lambda n_0 8\pi^2c^2\varepsilon_0 n_0 chlw}{e^2\lambda^2 P\lambda_{inj}\left(\frac{1}{m_e^*} + \frac{1}{m_p^*}\right)}, \tag{10}$$

where e is the charge of an electron, λ is the wavelength of the laser, N and P are the numbers of the electrons and holes, ε_0 is the permittivity in a vacuum, and m_e^* and m_p^* are the effective electron and hole masses, respectively.

When the wavelength of the injected light is 820 nm, the electrons in the cavity are heated and enhance the backfilling effect, which increases the lifetime of electrons in the lower laser energy level (A3) as described by the following equation [20]:

$$\frac{1}{\tau_{3,i}} = \frac{1}{\tau'_{3,i}} - \frac{1}{\tau_{\mathrm{bf}}}\left(e^{-\frac{E_{\mathrm{bf}}}{K_{\mathrm{b}}T}} - e^{\frac{E_{\mathrm{bf}}}{K_{\mathrm{b}}(T+\Delta T)}} \right), i = 1,2\ , \quad (11)$$

where T is the electron temperature without injected light, ΔT is the variation in electron temperature induced by the injected light, E_{bf} is the backfilling energy, and τ_{bf} is the backfilling lifetime. $\tau_{3,\mathrm{i}}$ and $\tau'_{3,\mathrm{i}}$ are the electron lifetimes in A3 with and without injected light, respectively, and K_{b} is the Boltzmann constant. To determine ΔT, we assume that all the energy of the optically excited electrons, except those that overcome the bandgap, converts to the kinetic energy of the electrons in the cavity. So the kinetic energy of a single optically excited electron E can be described by the following function (it can be verified by the well-known Fermi–Dirac distribution function):

$$E = K_{\mathrm{b}}\Delta T. \quad (12)$$

And E can be described as

$$E = \frac{c}{\lambda_{\mathrm{inj}}}h - E_{\mathrm{g}}, \quad (13)$$

where E_{g} is the bandgap. So the average variation in electron temperature can be described as

$$\Delta T = \frac{En_{\mathrm{inj}}}{K_{\mathrm{b}}\left(n_{\mathrm{inj}} + N_{\mathrm{e}}\right)}, \quad (14)$$

where $n_{\mathrm{inj}}$is the number of optically excited electrons, and N_{c} is the number of electrons in the cavity without optical injection.

The values of the key device parameters used in analyzing are summarized in Table 1.

Simulation

In this simulation, the laser we studied is the same as in [26], which is a standard 35-stage $In_{0.52}Al_{0.48}As/In_{0.53}Ga_{0.47}As$ type-I four-level Fabry–Perot QCL based on a two-phonon-resonance design [27]. Current injection efficiency is defined as the ratio of current to total current injected into the upper subband of the QCL in the active region, which is close to 56%. The QCL total optical loss is assumed to be 23.3 cm^{-1}, including a 14.3 cm^{-1} waveguide loss [27] and a 9 cm^{-1} mirror loss for a waveguide refractive index of 3.4. Although there are many bound states in the active region, most electrons remain in several low energy levels. So seven confined subbands are sufficient for the calculation, and here Ai (i = 1, 2, 3, 4, 5, 6, 7) represents the i-th subband in the active region, as shown in Figure 2. Our simulation used an external bias electrical field of 53 kV/cm, which was above the threshold value, and the temperature of the electrons and cavity were 300 K and 30 K, respectively.

Electron population

Figure 3 shows the number of electrons in subbands A1–A7 using an optical injection power of 1–5 mW for wavelengths of 1550 nm (a) and 820 nm (b). In Figure 3a, because the injected light of wavelength 1550 nm increases the number of electrons by accumulating holes, the electron numbers in each subband increase as injection power increases. But electron numbers in subbands A5–A7 are not much different than A1–A4, which results from there being fewer electrons in A5–A7 than A1–A4. In many other studies [17,18,20,21], electrons in A5–A7 have been largely ignored, and similarly, the electron number in A1 is much larger than in the other energy levels, so the variation in the number of electrons in A1 is much larger than in A2–A7. The number of electrons in A2 is lower than in A3 and A4 because it functions as an excessive subband that accelerates the transition of electrons from A3 to A1 [26]. There are some differences in electron numbers of A1–A4 when the wavelength of the injected light is 820 nm, as shown in Figure 3b.

Table 1: List of analyzing parameters.

Parameter	Value	Unit	Parameter	Value	Unit
Γ_{P}	0.8	–	E_{bf}	0.1616	eV
N_{P}	35	–	N_{c}	2.04×10^{11}	$1/cm^2$
α	23.336	1/cm	E_{g}	0.8	eV
n_0	3.4	–	τ_{p}	8	ns
m_{p}^*	0.4	–	l	1.358×10^{-3}	m
m_{e}^*	0.042	–	w	1.4×10^{-5}	m
T	300	K			

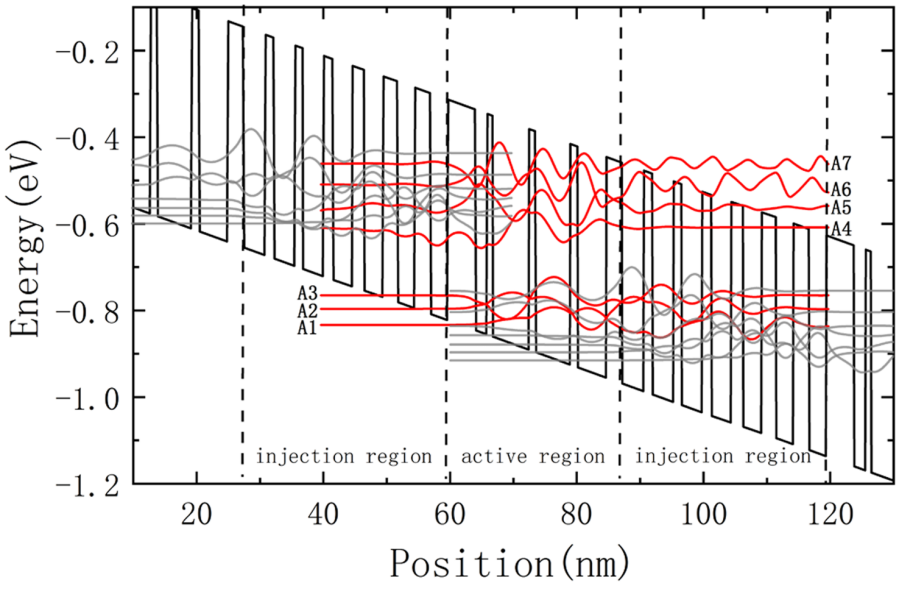

Figure 2: Calculated conduction subbands and moduli squared of relevant wave functions with a 53 kV/cm DC bias.

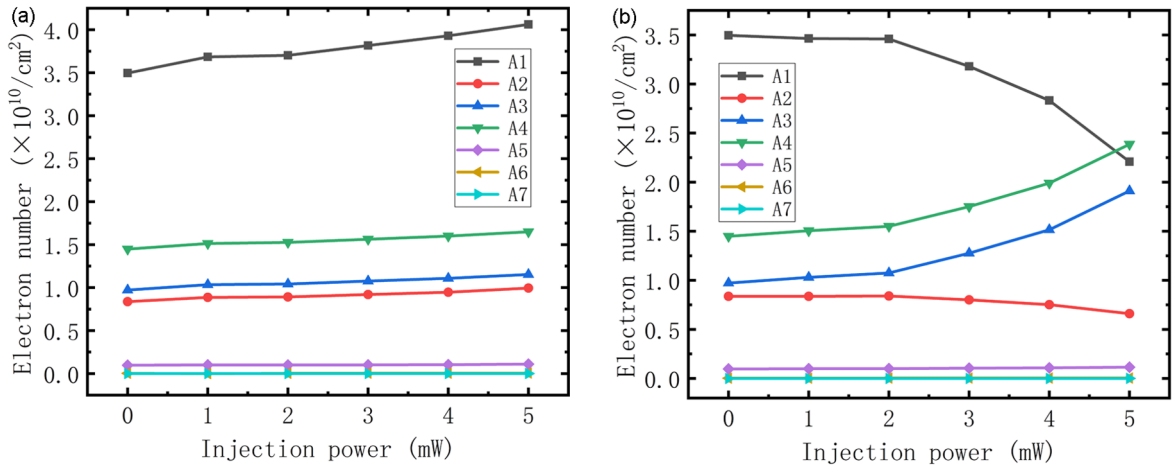

Figure 3: Numbers of electrons in each subband using optical injection at wavelengths of 1550 nm (a) and 820 nm (b).

First, compared with the behavior in Figure 3a, electron numbers in A3 and A4 increased to a greater extent with increasing injection power. This is a result of a backfilling effect which increased the lifetime of electrons, and hence their number, in A3, resulting in fewer electrons transitioning from A4 to A3 and increasing the number of electrons in A4, leading to the variation in numbers of electrons in A4 with injection power being almost the same as that for A3. Moreover, as the lifetime of electrons in A3 increases, the time that electrons spend in A3 becomes longer, which restrains electrons from transitioning from A3 to A2 and A1, resulting in the numbers of electrons in A1 greatly decreasing with injection power.

Electron lifetime

With the variation in electron numbers in each subband, naturally it is necessary to consider the change in electron lifetime in the corresponding subband. As Figure 4a shows, since electrons in subband A1 have the lowest energy compared with those in A2–A7, they have the longest lifetime. The second longest electron lifetime was in A4 as a result of an external electrical field that caused a population inversion. Moreover, in Figure 4a, which depicts the electron lifetime of each subband using injection of light of wavelength 1550 nm, the change in electron lifetime is not very obvious because the number of optically induced electron–hole pairs is much lower (by about

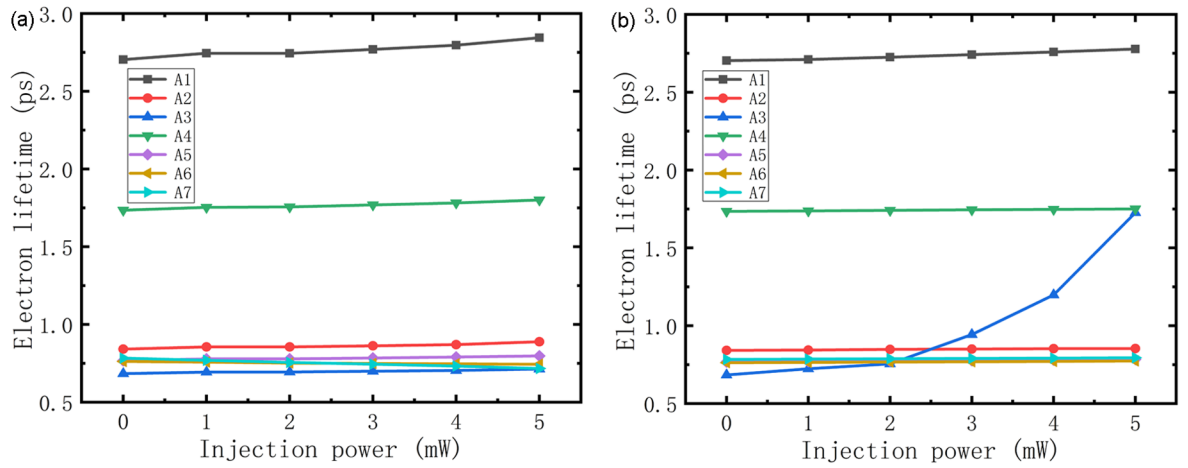

Figure 4: Electron lifetime of each subband using optical injection at wavelengths of 1550 nm (a) and 820 nm (b).

an order of magnitude) than for electrons in the cavity. The electron lifetime in A1–A6 increases with injection power because as numbers of electrons increase in those subbands, the number of unoccupied quantum states is reduced, which causes the transition of electrons between those subbands to become less frequent. There are also some differences in Figure 4b. Due to the backfilling effect, which is enhanced by increases in electron temperature, the lifetime of electrons in A3 increases greatly with optical injection power at 820 nm. This behavior results from injected light at that wavelength exciting electrons to high-*k* states, which increases the average temperature of the electrons. And because the backfilling effect only occurs in the lower laser energy level (A3) [20], the variation in electron lifetime with injection power in the other subbands is similar to that in Figure 4a.

Gain

Optical gain in the cavity during optical injection was also studied. As shown in Figure 5, although the wavelength of injected light is different, the variation of the optical gain is the same and there is less variation. This can be understood from Figure 3 in which the difference in electron number between A4 (upper laser subband) and A3 (lower laser subband) states is almost constant with changes in optical injection power. This difference is indirect proportional to optical gain, indicating that the modulation is not caused by changing the gain.

Current

Figure 6 shows when the injection power increases, the cavity current using injected light at a wavelength of 1550 nm increases as well. Because such injected light only increases the number of electrons in the cavity, it enhances the current upon an increase in injection power. While the cavity current using injected light at a wavelength of 820 nm increases at first, when the injection power reaches 2 mW, it reaches its maximum value of 0.65 A and then decreases with further increase in injection power. This behavior occurs because, in addition to increasing electrons in the cavity, injected light at 820 nm also in-

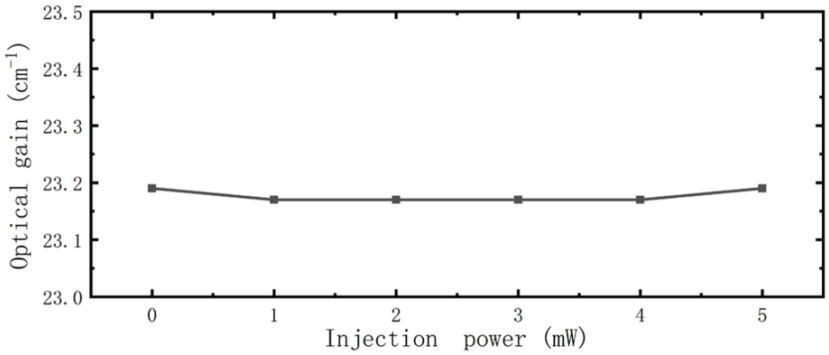

Figure 5: Optical gain as a function of optical injection power.

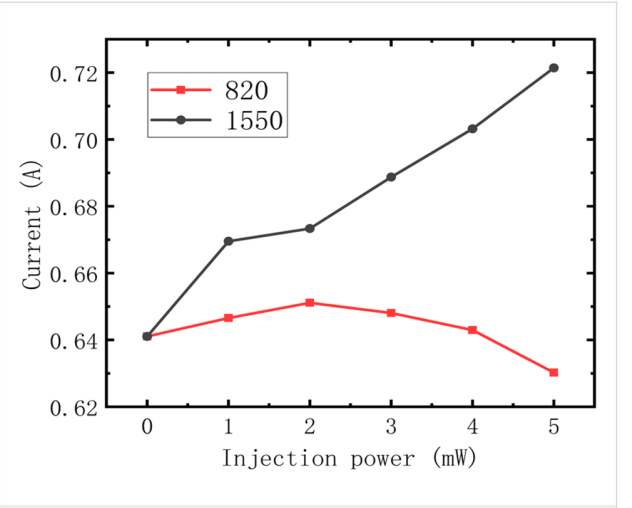

Figure 6: Current vs optical injection power at wavelengths of 1550 nm (black circles) and 820 nm (red squares).

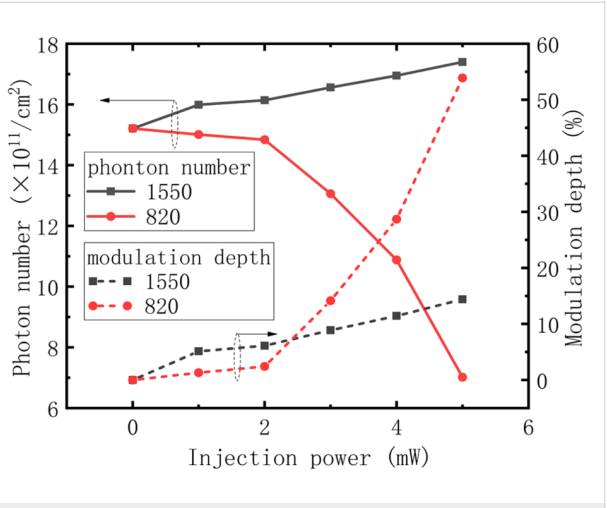

Figure 7: Modulation depth and photon number vs optical injection power at two wavelengths.

creases the temperature of the electrons, which enhances the backfilling effect and blocks the transition of electrons. Before the injection power reaches 2 mW, the increasing number of electrons plays a dominant role in the process, and the current therefore increases with injection power. Above 2 mW, the effect of backfilling surpasses this effect, so the current is reduced with increasing injection power. In addition, there is an inflection in the curve for injected light at 1550 nm when the injection power reaches 1 mW, where it appears to deviate from a line through the other five points. This results from the arithmetic we used to solve the rate equations. There are numerous solutions to the rate equations, so we solved them iteratively, and for different initial conditions (electron number in the cavity), the solution may not have always been linear.

Modulation depth

Finally, modulation depth using different injection conditions was studied. Figure 5 shows that gain has almost nothing to do with modulation, while for the rate equation, it is not so difficult to demonstrate that the transition speed of electrons between subbands is determined by electron numbers and lifetime in each, and that transition speed is key to the number of photons in the cavity. So we conclude that modulation is induced by the number of electrons and their lifetime. As shown in Figure 7 (black line with square symbols), when the wavelength of the injected light is 1550 nm, the number of photons and modulation depth increase with injection power so that when it reaches 5 mW, the modulation has a value of 15%, which is half the experimental result [19]. The increase in modulation depth with injection power is reminiscent of that for current shown in Figure 6. This modulation characteristic is not difficult to explain, the injected light increases the numbers of electrons (Figure 3a), although it also causes the increase in electron lifetime shown in Figure 4, which may slow the transition. However, from Figure 6 we know that the numbers of electrons play the major role in enhancing current, so with an increase in injection power, the number of photons in the cavity increases, and modulation is achieved. In terms of the injected light at a wavelength of 820 nm shown in Figure 7, the number of photons in the cavity is reduced with an increase in injection power. Although the electron number in A3 and A4 increases as shown in Figure 3b, which enhances the transition process, it can be seen from Figure 4b that electron lifetime in A3 greatly increases, resulting in electrons remaining in A3 for longer times. This blocks the transition from A4 to A3, thus reducing the number of photons in the cavity and achieving modulation.

Conclusion

In this paper, to explore the phenomenon of all-optical modulation of QCLs, we studied the characteristics of a mid-infrared QCL using near-infrared optical injection of several mW at wavelengths of 820 nm and 1550 nm. A modified classical 1½-period model was established to characterize the process of optical injection, and optically excited electrons and optically induced temperature enhancement are considered in our model. The following parameters were calculated: electron population and lifetime in each subband, optical gain, current and photons in the cavity, which were consistent with the experimental results. We found that for injected light at wavelengths of 820 nm or 1550 nm, electron population and lifetime increases, but does not affect optical gain. Furthermore, injected light at a wavelength of 1550 nm always enhances the current, but at 820 nm only does so when the power of the injected light is greater than 2 mW. Finally, the calculations show that numbers of electrons and electron lifetime in the cavity are of great importance in all-optical modulation of QCLs.

Acknowledgements

The authors would like to thank Yuan-kun Sun, University of Electronic Science and Technology of China, for the help on this work.

Funding

This work was supported by the National Key R&D Program of China under grant 2019YFC0605203, in part by the Chongqing Postgraduate Research and Innovation Project (CYS21059), and in part by Chongqing Basic Research and Frontier Exploration Project (cstc2020jcyj-msxmX0553).

References

1. Faist, J.; Capasso, F.; Sivco, D. L.; Hutchinson, A. L.; Chu, S.-N. G.; Cho, A. Y. *Appl. Phys. Lett.* **1998,** *72,* 680–682. doi:10.1063/1.120843
2. Spitz, O.; Herdt, A.; Wu, J.; Maisons, G.; Carras, M.; Wong, C.-W.; Elsäßer, W.; Grillot, F. *Nat. Commun.* **2021,** *12,* 3327. doi:10.1038/s41467-021-23527-9
3. Rodriguez, E.; Mottaghizadeh, A.; Gacemi, D.; Palaferri, D.; Asghari, Z.; Jeannin, M.; Vasanelli, A.; Bigioli, A.; Todorov, Y.; Beck, M.; Faist, J.; Wang, Q. J.; Sirtori, C. *ACS Photonics* **2018,** *5,* 3689–3694. doi:10.1021/acsphotonics.8b00704
4. Irimajiri, Y.; Morohashi, I.; Kawakami, A. *IEEE Trans. Terahertz Sci. Technol.* **2020,** *10,* 474–479. doi:10.1109/tthz.2020.2990358
5. Dostál, M.; Suchánek, J.; Válek, V.; Blatoňová, Z.; Nevrlý, V.; Bitala, P.; Kubát, P.; Zelinger, Z. *Energy Fuels* **2018,** *32,* 10163–10168. doi:10.1021/acs.energyfuels.8b01021
6. Zhang, J.; He, Y.; Liang, S.; Liao, X.; Li, T.; Qiao, Z.; Chang, C.; Jia, H.; Chen, X. *Nat. Commun.* **2021,** *12,* 2730. doi:10.1038/s41467-021-23025-y
7. Liu, X.; Qiao, Z.; Chai, Y.; Zhu, Z.; Wu, K.; Ji, W.; Li, D.; Xiao, Y.; Mao, L.; Chang, C.; Wen, Q.; Song, B.; Shu, Y. *Proc. Natl. Acad. Sci. U. S. A.* **2021,** *118,* e2015685118. doi:10.1073/pnas.2015685118
8. Basnar, B.; Mujagic, E.; Andrews, A. M.; Klang, P.; Schrenk, W.; Strasser, G. Novel Thermal Tuning of Quantum Cascade Lasers Utilizing Thermochromic Claddings. Conference on Lasers and Electro-Optics/International Quantum Electronics Conference, Baltimore, MD, USA, June 2–4, 2009; OSA Technical Digest, Optica Publishing Group, 2009; CThC7. doi:10.1364/cleo.2009.cthc7
9. Tholl, H. D.; Münzhuber, F. System physics modeling of the electro-optical energy conversion in mid-infrared quantum cascade lasers. In *Proceedings pf SPIE , volume 9989,* Technologies for Optical Countermeasures XIII, Edinburgh, UK, Sept 26–29, 2016; Titterton, D. H.; Grasso, R. J.; Richardson, M. A., Eds.; SPIE Security + Defence, 2016. doi:10.1117/12.2240877
10. Kittlaus, E. A.; Jones, W. M.; Rakich, P. T.; Otterstrom, N. T.; Muller, R. E.; Rais-Zadeh, M. *Nat. Photonics* **2021,** *15,* 43–52. doi:10.1038/s41566-020-00711-9
11. Bovkun, L. S.; Ikonnikov, A. V.; Aleshkin, V. Y.; Krishtopenko, S. S.; Mikhailov, N. N.; Dvoretskii, S. A.; Potemski, M.; Piot, B.; Orlita, M.; Gavrilenko, V. I. *J. Exp. Theor. Phys. Lett.* **2018,** *108,* 329–334. doi:10.1134/s0021364018170058
12. Peng, C.; Zhou, H.; Zhu, L.; Chen, T.; Liu, Q.; Wang, D.; Li, J.; Peng, Q.; Chen, G.; Li, Z. *Opt. Lett.* **2017,** *42,* 4506–4509. doi:10.1364/ol.42.004506
13. Cai, H.; Liu, S.; Lalanne, E.; Guo, D.; Chen, X.; Wang, X.; Choa, F.-S.; Johnson, A. M. *Appl. Phys. Lett.* **2014,** *104,* 211101. doi:10.1063/1.4880358
14. Sheikhey, M. M.; Kavian, S.; Baghban, H. *Phys. Rev. A* **2018,** *98,* 053810. doi:10.1103/physreva.98.053810
15. Cheng, L.; Chen, X.; Choa, F.-S.; Worchesky, T. Integrated tunable DBR quantum cascade lasers with 30 cm^{-1} tuning range at 4.7 μm. In *Proceedings of SPIE vol.7616,* Novel In-Plane Semiconductor Lasers IX, San Francisco, CA, USA, Jan 23–28, 2010; Belyanin, A. A.; Smowton, P. M., Eds.; SPIE OPTO, 2010. doi:10.1117/12.842397
16. Guo, D.; Cai, H.; Talukder, M. A.; Chen, X.; Johnson, A. M.; Khurgin, J. B.; Choa, F.-S. *Appl. Phys. Lett.* **2014,** *104,* 251102. doi:10.1063/1.4884605
17. Donovan, K.; Harrison, P.; Kelsall, R. W. *J. Appl. Phys.* **2001,** *89,* 3084–3090. doi:10.1063/1.1341216
18. Jirauschek, C.; Kubis, T. *Appl. Phys. Rev.* **2014,** *1,* 011307. doi:10.1063/1.4863665
19. Yang, T.; Chen, G.; Tian, C.; Martini, R. *Opt. Lett.* **2013,** *38,* 1200–1202. doi:10.1364/ol.38.001200
20. Li, Z.-M. S.; Li, Y.-Y.; Ru, G.-P. *J. Appl. Phys.* **2011,** *110,* 093109. doi:10.1063/1.3660207
21. Sakasegawa, Y.; Sekine, N.; Saito, S.; Ashida, M.; Kasamatsu, A.; Hosako, I. *J. Comput. Electron.* **2017,** *16,* 382–391. doi:10.1007/s10825-017-0962-2
22. Suchalkin, S.; Jung, S.; Tober, R.; Belkin, M. A.; Belenky, G. *Appl. Phys. Lett.* **2013,** *102,* 011125. doi:10.1063/1.4774267
23. Zheng, X.; Jiang, T.; Cheng, X.-A.; Jiang, H.-M.; Lu, Q.-S. *Acta Phys. Sin.* **2012,** *61,* 047302. doi:10.7498/aps.61.047302
24. Botez, D.; Shin, J. C.; Kumar, S.; Mawst, L. J.; Vurgaftman, I.; Meyer, J. R. *Opt. Eng. (Bellingham, WA, U. S.)* **2010,** *49,* 111108. doi:10.1117/1.3509368
25. Howard, S. S.; Liu, Z.; Wasserman, D.; Hoffman, A. J.; Ko, T. S.; Gmachl, C. F. *IEEE J. Sel. Top. Quantum Electron.* **2007,** *13,* 1054–1064. doi:10.1109/jstqe.2007.906121
26. Peng, C.; Sun, Y.; Zhu, L.; Chen, T.; Chen, G.; Yu, A.; Zhong, S.; Zhou, P.; Zhai, Z.; Li, Z. *IEEE Photonics J.* **2019,** *11,* 1–10. doi:10.1109/jphot.2019.2896081
27. Liu, Z.; Waserman, D.; Hward, S. S.; Hoffman, A. J.; Gmachl, C. F.; Wang, X.; Tanbun-Ek, T.; Cheng, L.; Chao, F. S. *IEEE Photonics Technol. Lett.* **2006,** *18,* 1347–1349. doi:10.1109/lpt.2006.877006

BEILSTEIN JOURNAL OF NANOTECHNOLOGY

Analytical and numerical design of a hybrid Fabry–Perot plano-concave microcavity for hexagonal boron nitride

Felipe Ortiz-Huerta* and Karina Garay-Palmett

Full Research Paper

Open Access

Address:
Departamento de Óptica, Centro de Investigación Científica y de Educación Superior de Ensenada, Ensenada, Baja California 22860, México

Email:
Felipe Ortiz-Huerta* - fortiz.huerta@gmail.com

* Corresponding author

Keywords:
Fabry–Perot; hBN; microcavities; plano-concave; polymers

Beilstein J. Nanotechnol. **2022,** *13,* 1030–1037.
https://doi.org/10.3762/bjnano.13.90

Received: 31 May 2022
Accepted: 15 September 2022
Published: 27 September 2022

This article is part of the thematic issue "Physics and optical applications of all-dieletric nanostructures".

Guest Editor: Z. Han

Abstract

An efficient single-photon emitter (SPE) should emit photons at a high rate into a well-defined spatio-temporal mode along with an accessible numerical aperture (NA) to increase the light extraction efficiency that is required for effective coupling into optical waveguides. Based on a previously developed experimental approach to fabricate hybrid Fabry–Perot microcavities (Ortiz-Huerta et al. *Opt. Express* **2018**, *26*, 33245), we managed to find analytical and finite-difference time-domain (FDTD) values for the, experimentally achievable, geometrical parameters of a hybrid plano-concave microcavity that enhances the spontaneous emission (i.e., Purcell enhancement) of color centers in two-dimensional (2D) hexagonal boron nitride (hBN) while simultaneously limiting the NA of the emitter. Paraxial approximation and a transfer matrix model are used to find the spotsize of the fundamental Gaussian mode and the resonant modes of our microcavity, respectively. A Purcell enhancement of 6 is found for a SPE (i.e., in-plane dipole) hosted by a 2D hBN layer inside the hybrid plano-concave microcavity.

Introduction

Pure and indistinguishable SPEs are key components needed for their application in upcoming quantum technologies [1] (e.g., quantum computation [2] and quantum networks [3]). Color centers in 2D hBN and diamonds are among the most promising candidates for solid-state single-photon emission at room temperature [4,5]. Nonetheless, in contrast with bulk diamond, the 2D nature of hBN, hosting color centers (i.e., in-plane dipoles), overcomes the necessity for geometrical approaches [6] (i.e., solid immersion lenses [7]) to reduce the angle of emission of the selected SPE.

Challenges still lie ahead for hBN as an ideal SPE [4] and, in order to overcome them, photonic structures such as open-access Fabry–Perot microcavities [8], microdisk resonators [9], and photonic crystals [10,11] have been designed and built around color centers in hBN to increase its spontaneous emis-

sion by means of Purcell effect. An alternative and low-cost approach to build photonic structures uses polymers to embed different types of SPEs (e.g., quantum dots [12], molecules [13]) by a process known as two-photon polymerization (2PP) [14] where a photopolymer resist is illuminated with a focused laser at 780 nm and absorbs two photons simultaneously, which triggers a corresponding chemical reaction that solidifies the material to build the desired shape.

A natural extension to the development of polymer photonic structures consists of the fabrication of hybrid (i.e., metal-dielectric) resonant structures [15] with the potential to enhance the light–matter interactions of such SPEs. This work will focus on finding an optimal design for a hybrid plano-concave microcavity, containing a multilayer of hBN hosting a SPE (Figure 1), by using analytical methods and FDTD simulations.

Fabrication design steps are first shown for our microcavity, afterwards we found the range of geometrical parameters necessary for our stable resonator, followed by a transfer matrix model used to find the resonant modes of the microcavity, which are then corroborated by FDTD simulations.

Results and Discussion

Fabrication design

Hybrid plano-concave microcavity

By using a quarter-wavelength DBR with a multilayer 2D material on top (Figure 2a), we designed our system (2D material + DBR stack) to have a maximum reflectivity at the center wavelength of 637 nm. The selected wavelength of our system falls within the typical emission rates of the zero-phonon line (ZPL) of SPEs in hBN (500–800 nm). A quarter-wavelength thickness is conveniently chosen for the hBN where its value falls between experimentally achievable thicknesses of multilayer 2D materials [6].

A 3D concave shape polymer then could be fabricated on top of the 2D material (Figure 2b) by a direct laser writing system (e.g., Photonic Professional, Nanoscribe GmbH) by use of a 2PP process.

Afterwards an 80 nm silver layer could be added, by thermal evaporative deposition, on top of the concave shape polymer to ensure a high reflectivity inside our microcavity. When designing the concave shape polymer a small rectangular aperture at its edge must be taken into account in the fabrication step (Figure 2b,c) to prevent the accumulation of the photopolymer resist, inside the solidified concave polymer, when the sample is developed (SU-8 developer) and cleaned (IPA) to remove any remaining photoresist and developer, respectively, after the 2PP process is finished.

Analytical design

Geometrical parameters of the plano-concave microcavity

When a polymer layer is added inside a bare microcavity, as in our case, two fundamental Gaussian beams are formed inside the air gap and polymer layer, respectively (Figure 3) [16].

The spotsize W_{02} (Figure 3) of the fundamental Gaussian mode (TEM_{00}) inside the cavity has to be as small as possible, since this means a small modal volume and consequently, a high Purcell factor [17].

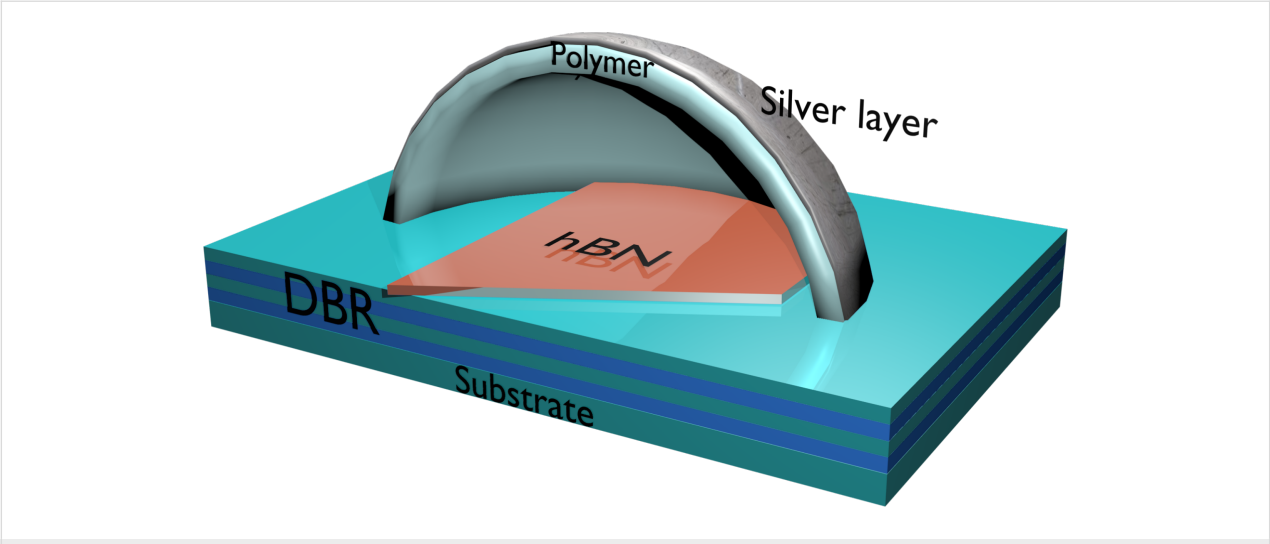

Figure 1: Conceptual design shows cross-section of hybrid plano-concave microcavity with a 2D hBN layer inside on top of a distributed Bragg reflector (DBR).

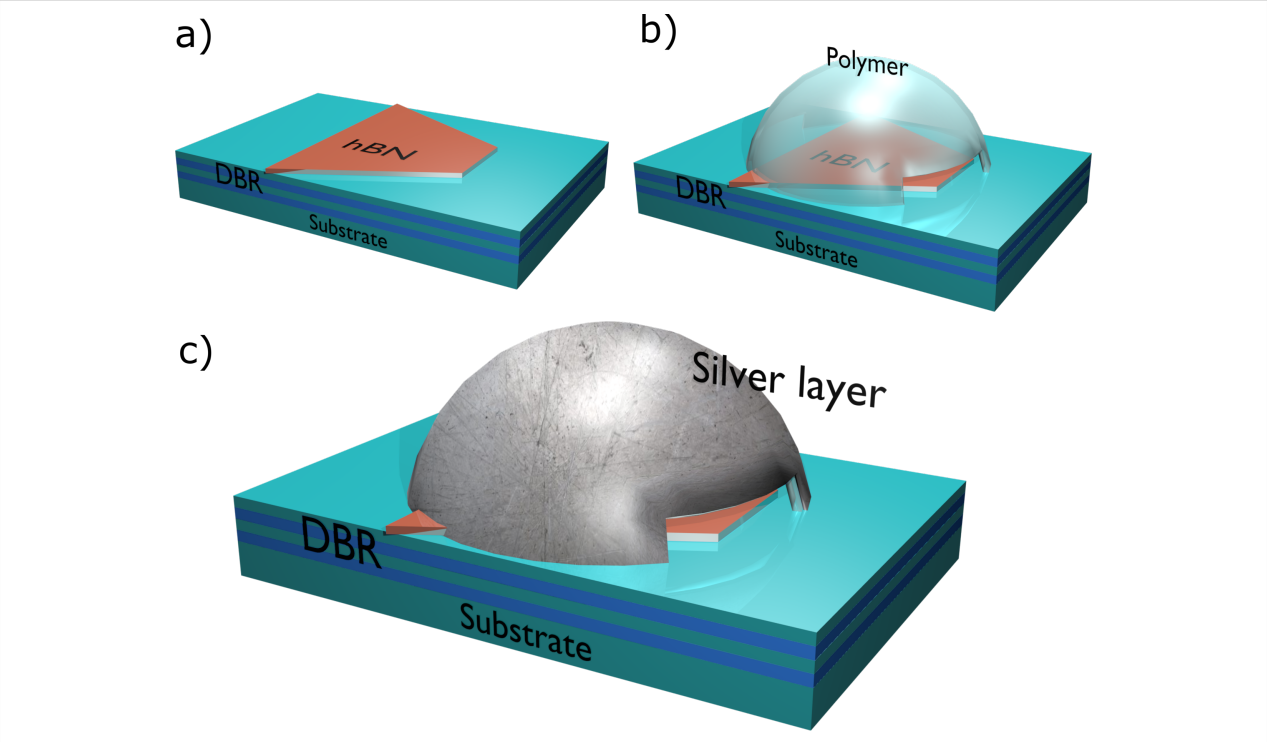

Figure 2: Fabrication steps of hybrid microcavity. (a) hBN layer positioned on top of DBR. (b) Concave polymer shape is fabricated by direct laser writing process. (c) A silver layer is added on top of polymer.

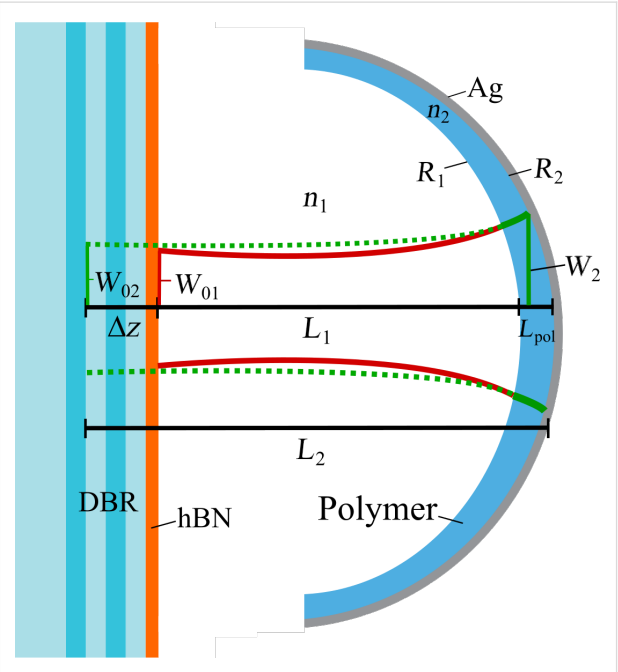

Figure 3: Cross-section of hybrid plano-concave microcavity shows the geometrical parameters and the two Gaussian modes inside.

By setting an arbitrary range of values for the length of the second Gaussian beam L_2 and radius of curvature R_2 of our plano-concave microcavity, Figure 4 shows the spotsizes W_{02} and W_2 corresponding to different pair of values (R_2, L_2) for a hybrid plano-concave cavity. The spotsizes W_{02} and W_2 are calculated by [18]:

$$W_{02}^2 = \frac{L_2\lambda_0}{\pi n_2}\sqrt{\frac{g}{1-g}} \tag{1}$$

and

$$W_2^2 = \frac{L_2\lambda_0}{\pi n_2}\sqrt{\frac{1}{g(1-g)}}, \tag{2}$$

respectively, where $g = 1 - L_2/R_2$ is the stability range for our plano-concave cavity and $\lambda_0 = 637$ nm is the wavelength of the fundamental Gaussian mode, $n_2 = 1.52$ is the refractive index of the polymer layer. The length of the second Gaussian beam is defined as $L_2 = L_1 + L_{pol} + \Delta z$, where L_1 is the length of the Gaussian beam in air, L_{pol} is the polymer thickness and Δz is calculated by the ABCD law [16]:

$$q_2 = \frac{Aq_1 + B}{Cq_1 + D}, \tag{3}$$

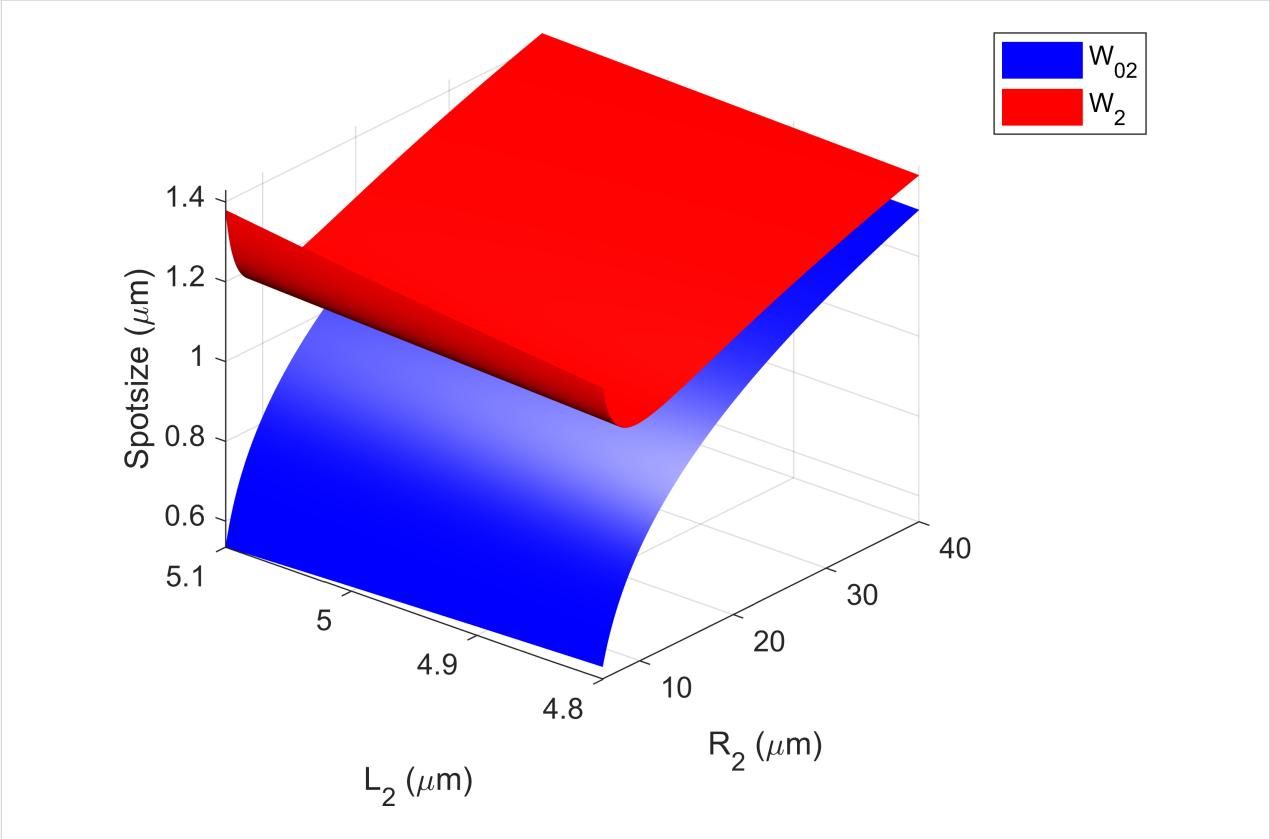

Figure 4: Spotsizes W_{02} and W_2 for different values of R_2 and L_2.

where the complex numbers $q_{1,2} = z_{1,2} + jz_{R,1,2}$ are known as the q-parameters for the Gaussian beams, where $z_2 = L_2 - L_p$, $z_1 = L_1$ and $z_{R,1,2}$ is the Rayleigh length for each beam. For a Gaussian beam passing through a plane dielectric interface, we have $A = B = C = 0$, and $D = n_2/n_1$, where $n_1 = 1$ is the refractive index of the air gap, therefore, by substituting in Equation 3, $q_2 = (n_2/n_1)q_1$. This leads to $z_2 = (n_2/n_1)z_1$ and $W_{01} = W_{02}$. Finally, by defining $\Delta z = z_2 - z_1$ we get:

$$\Delta z = \left(\frac{n_2}{n_1} - 1\right) L_1. \tag{4}$$

As a threshold for R_2 we set $R_2 \geq L_2$ in accordance with the stability range where $0 \leq g \leq 1$. Although work has been done to include the lensing effect of a curved "n_1/n_2" interface (see supplementary material of [19]), the planar surface ($R_1 = \infty$) approximation values (Table 1) fall within the desired range with our FDTD simulations.

We take a transversal cut through a fixed value of L_2 (Figure 5) and observe the dependence of W_{02} and W_2 to the radius of curvature (R_2) of a plano-concave cavity. To achieve a high Purcell factor, and a small NA, R_2 must be as small as possible (small W_{02}), while maintaining the lower boundary condition ($R_2 \geq L_2$), therefore the optimal values of R_2, for any arbitrary L_2, will reside near the vicinity of the minima of the W_2 function (Figure 5), setting the boundary values for R_2, for any given L_2, at $R_2 \approx 2L_2$.

Selecting the R_2 parameter closer to the divergence of the W_2 function ($R_2 = L_2$) could result in unstable resonators that will not hold a stable Gaussian mode inside. Theoretical work has been done with $R_2 \approx L_2$ [20], where a non-paraxial analysis is performed, although diffraction losses have to be considered for an accurate description of the experimental limits of stability [21]. In the unstable regime ($R_2 < L_2$) extensive work has also been done [22,23].

Electric field distribution and resonant modes of the plano-concave microcavity

A $\lambda_0/4n$ thickness layer of hBN ($n = 1.72$) was positioned on top of a 15-pair layer DBR with tantalum oxide (Ta_2O_5) and silicon oxide (SiO_2) as the high- and low-index layers, respectively, on a $(HL)^{15}$ configuration to ensure an electric field antinode at the surface of the hBN layer, making the hBN + DBR system a $L(HL)^{15}$ dielectric stack. A transfer

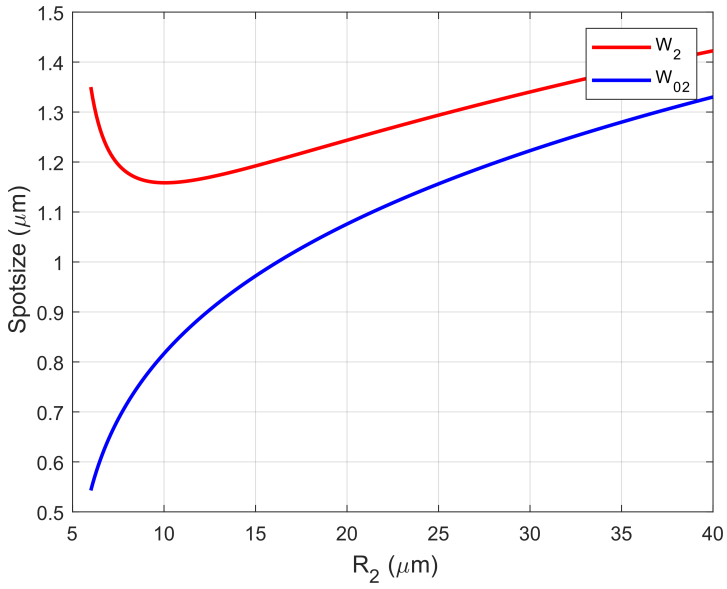

Figure 5: Transverse cut of Figure 4 through length L_2 = 5.03 µm to show dependence of R_2 with spotsizes. As the values of R_2 diminishes, while maintaining a constant L_2, the functions for W_{02} (blue) and W_2 (red) start to diverge, arriving at the limit of the paraxial approximation (stability regime).

matrix model [24] was used to calculate the electric field distribution inside the hBN + DBR system (Figure 6).

The full transfer matrix S of our microcavity is defined as:

$$S = L_{\mathrm{Ag}} I_1 L_{\mathrm{pol}} I_2 L_{\mathrm{air}} I_3 L_{\mathrm{hBN}} I_4 L_{\mathrm{DBR}} I_5, \tag{5}$$

where L and I represent the transfer and interface matrix, respectively, of the silver (Ag), polymer (pol), air, hBN and DBR layer. The transfer matrices L_{pol} and L_{air} are defined as [25]:

$$L_{\mathrm{pol}} = \begin{bmatrix} \exp\left(-\dfrac{i2\pi n_2}{\lambda_0} + iG_2\right) & 0 \\ 0 & \exp\left(-\dfrac{i2\pi n_2}{\lambda_0} + iG_2\right) \end{bmatrix}, \tag{6}$$

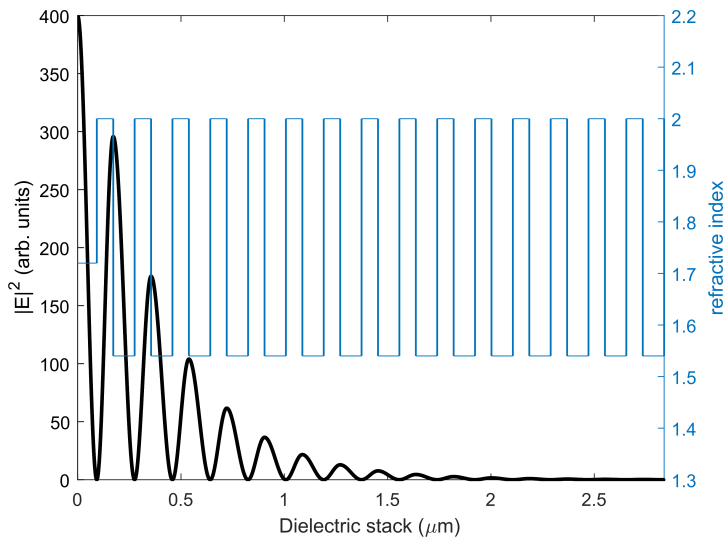

Figure 6: Electric field distribution of a hBN + DBR system on a $L(HL)^{15}$ configuration. Maximum electric field intensity is found at the surface of the hBN layer. Vertical lines (blue) represent the boundaries between each dielectric layer.

$$L_{\text{air}} = \begin{bmatrix} \exp\left(-\frac{i2\pi n_1}{\lambda_0} + iG_1\right) & 0 \\ 0 & \exp\left(-\frac{i2\pi n_1}{\lambda_0} + iG_1\right) \end{bmatrix}, \quad (7)$$

where $G_{1,2} = \arctan(L_{1,2}\lambda_0/n_{1,2}\pi W_{01,02})$ is the Guoy phase shift in the air ($n_1 = 1$) and polymer layer, respectively, where $W_{01} = W_{02}$.

The transmittance of the microcavity is calculated, from the matrix elements of S, to find its fundamental TEM resonant modes (Figure 7). We found the desired TEM modes at $R_2 = 8.1$ µm and $L_2 = L_1 + L_{\text{pol}} + \Delta z = 5.03$ µm, where $L_1 = 3.09$ µm, $L_{\text{pol}} = 0.4$ µm and $\Delta z = 1.54$ µm, which gives a physical cavity length of $L = L_2 - \Delta z = 3.49$ µm. These values fall within the stability range $R_2 \approx 2L_2$.

Numerical design

Resonant modes of hybrid plano-concave microcavity

For the FDTD simulations, we used the Ansys Lumerical FDTD software. The polymer, and DBR stack were treated as lossless and non-dispersive materials [15]. A transmittance $T = 8\%$ at 637 nm is measured for our cavity, with an in-plane dipole inside, for a silver layer thickness of 80 nm. Identical values for the geometrical parameters previously mentioned (R_2, L_2, L_1), except for $R_1 = 7.7$ µm, were taken for the FDTD simulations, where an in-plane dipole emitter sits at the surface of the hBN layer to ensure a higher Purcell factor since the dipole interacts with an electric field antinode [26]. The Purcell factor was calculated by using the classical definition [27]:

$$F_{\text{p}} = \frac{P_{\text{cav}}}{P_{\text{free}}}, \quad (8)$$

where P_{cav} and P_{free} is the power dissipated for the dipole inside the microcavity and in free space, respectively. A Purcell factor of $F_{\text{P}} \approx 6$ was achieved for the TEM mode at the DBR center wavelength. A Q-factor of $Q = 731.4 \pm 102.7$ was also calculated in our simulations where the resonant modes of the microcavity (Figure 8) are shown in good agreement (Table 1) with the resultant modes from the analytical model (Figure 7).

Table 1: Geometrical parameters and fundamental TEM mode values of the designed hybrid plano-concave microcavity.

Parameter	Analytical (µm)	FDTD (µm)
R_2	8.1	8.1
physical cavity length, L	3.49	3.49
$L1$	3.09	3.09
$L2$	5.03	5.03
hBN thickness	$\lambda_0/4n$	$\lambda_0/4n$
polymer thickness	0.4	0.4
1st TEM_{00}	0.595	0.616
2nd TEM_{00}	0.636	0.637
3rd TEM_{00}	0.684	0.684
R_1	∞	7.7

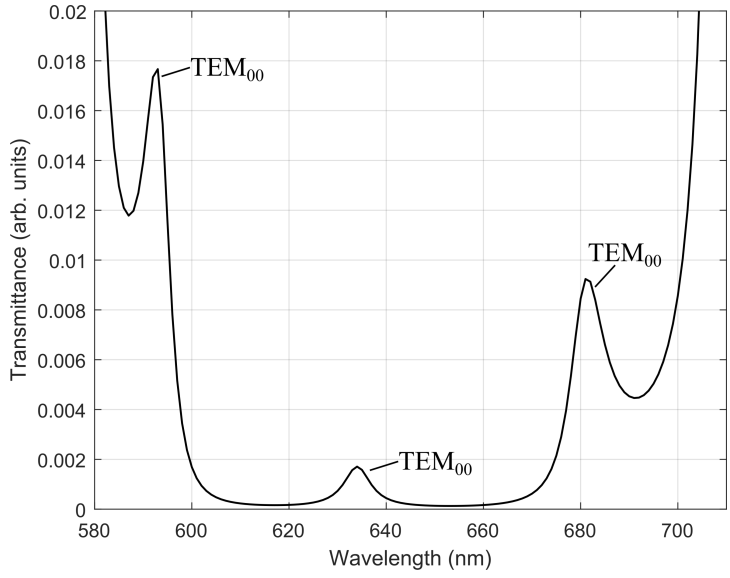

Figure 7: Transmittance of plano-concave cavity shows the fundamental TEM modes at 595 nm, 636 nm and 684 nm.

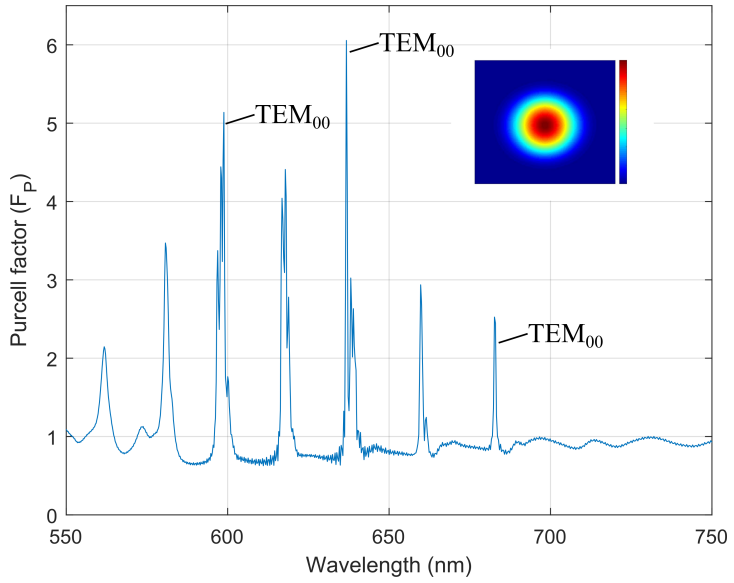

Figure 8: Purcell factor of plano-concave microcavity. Fundamental TEM Gaussian modes are found at 595 nm, 636 nm and 684 nm. Inset shows transverse section of fundamental Gaussian mode at 637 nm.

Conclusion

We have presented the fabrication design steps for a new type of hybrid plano-concave microcavity and found its fundamental resonant modes by using an expanded transfer matrix model to account for the curvature in dielectrics and, by using FDTD simulations, we were able to show the effectiveness of the analytical model and found a Purcell enhancement of 6 for a preselected SPE.

The geometrical parameters of our microcavity are all experimentally achievable with the two-photon absorption fabrication process [13,15] and our modeled cavity could easily be extended to contain and enhance spontaneous emission of arbitrary solid-state SPEs [28]. Although novel approaches have been realized to diminish vibrations for open-access Fabry–Perot microcavities inside a cryostat system [29], in our design, the plano-concave microcavity is integrated directly to the substrate containing the SPE and, therefore, there are no moving parts that could potentially diminish the Purcell factor of a preselected SPE due to vibrations in cavity length [30], although detuning of the selected mode, due to thermally-induced contraction of the polymer by cooling [12], must be taken into account if the desired SPE and the cavity are to be analyzed inside a cryostat system.

The methodology of design of the hybrid Fabry-Perot microcavity is also suited for quantum cryptography applications, provided the emitter's wavelength is within the telecom range [6], and potential chemical sensing applications [31], since our microcavity is also an open-access cavity.

Funding

FO acknowledges financial support from Consejo Nacional de Ciencia y Tecnología (CONACYT) postdoctoral fellowship program, KG from CONACYT Grants (Laboratorios Nacionales 315838/2021).

ORCID® iDs

Felipe Ortiz-Huerta - https://orcid.org/0000-0001-9531-6099
Karina Garay-Palmett - https://orcid.org/0000-0001-9660-843X

Preprint

A non-peer-reviewed version of this article has been previously published as a preprint: https://doi.org/10.48550/arXiv.2205.06307

References

1. Gibney, E. *Nature* **2019,** *574,* 22–24. doi:10.1038/d41586-019-02935-4
2. Arrazola, J. M.; Bergholm, V.; Brádler, K.; Bromley, T. R.; Collins, M. J.; Dhand, I.; Fumagalli, A.; Gerrits, T.; Goussev, A.; Helt, L. G.; Hundal, J.; Isacsson, T.; Israel, R. B.; Izaac, J.; Jahangiri, S.; Janik, R.; Killoran, N.; Kumar, S. P.; Lavoie, J.; Lita, A. E.; Mahler, D. H.; Menotti, M.; Morrison, B.; Nam, S. W.; Neuhaus, L.; Qi, H. Y.; Quesada, N.; Repingon, A.; Sabapathy, K. K.; Schuld, M.; Su, D.; Swinarton, J.; Száva, A.; Tan, K.; Tan, P.; Vaidya, V. D.; Vernon, Z.; Zabaneh, Z.; Zhang, Y. *Nature* **2021,** *591,* 54–60. doi:10.1038/s41586-021-03202-1

3. Janitz, E.; Bhaskar, M. K.; Childress, L. *Optica* **2020,** *7,* 1232–1252. doi:10.1364/optica.398628
4. Aharonovich, I.; Englund, D.; Toth, M. *Nat. Photonics* **2016,** *10,* 631–641. doi:10.1038/nphoton.2016.186
5. Caldwell, J. D.; Aharonovich, I.; Cassabois, G.; Edgar, J. H.; Gil, B.; Basov, D. N. *Nat. Rev. Mater.* **2019,** *4,* 552–567. doi:10.1038/s41578-019-0124-1
6. Vogl, T.; Lecamwasam, R.; Buchler, B. C.; Lu, Y.; Lam, P. K. *ACS Photonics* **2019,** *6,* 1955–1962. doi:10.1021/acsphotonics.9b00314
7. Hadden, J. P.; Harrison, J. P.; Stanley-Clarke, A. C.; Marseglia, L.; Ho, Y.-L. D.; Patton, B. R.; O'Brien, J. L.; Rarity, J. G. *Appl. Phys. Lett.* **2010,** *97,* 241901. doi:10.1063/1.3519847
8. Häußler, S.; Bayer, G.; Waltrich, R.; Mendelson, N.; Li, C.; Hunger, D.; Aharonovich, I.; Kubanek, A. *Adv. Opt. Mater.* **2021,** *9,* 2002218. doi:10.1002/adom.202002218
9. Wang, Y.; Lee, J.; Berezovsky, J.; Feng, P. X.-L. *Appl. Phys. Lett.* **2021,** *118,* 244003. doi:10.1063/5.0046080
10. Fröch, J. E.; Kim, S.; Mendelson, N.; Kianinia, M.; Toth, M.; Aharonovich, I. *ACS Nano* **2020,** *14,* 7085–7091. doi:10.1021/acsnano.0c01818
11. Kim, S.; Toth, M.; Aharonovich, I. *Beilstein J. Nanotechnol.* **2018,** *9,* 102–108. doi:10.3762/bjnano.9.12
12. Sartison, M.; Portalupi, S. L.; Gissibl, T.; Jetter, M.; Giessen, H.; Michler, P. *Sci. Rep.* **2017,** *7,* 39916. doi:10.1038/srep39916
13. Colautti, M.; Lombardi, P.; Trapuzzano, M.; Piccioli, F. S.; Pazzagli, S.; Tiribilli, B.; Nocentini, S.; Cataliotti, F. S.; Wiersma, D. S.; Toninelli, C. *Adv. Quantum Technol.* **2020,** *3,* 2000004. doi:10.1002/qute.202000004
14. Kawata, S.; Sun, H.-B.; Tanaka, T.; Takada, K. *Nature* **2001,** *412,* 697–698. doi:10.1038/35089130
15. Ortiz-Huerta, F.; Chen, L.; Taverne, M.; Hadden, J. P.; Johnson, M.; Ho, Y. L. D.; Rarity, J. G. *Opt. Express* **2018,** *26,* 33245. doi:10.1364/oe.26.033245
16. Nemoto, S. *Appl. Opt.* **1989,** *28,* 1643. doi:10.1364/ao.28.001643
17. Kristensen, P. T.; Van Vlack, C.; Hughes, S. *Opt. Lett.* **2012,** *37,* 1649. doi:10.1364/ol.37.001649
18. Siegman, A. E. *Lasers;* University Science Books: Sausalito, CA, USA, 1986.
19. van Dam, S. B.; Ruf, M.; Hanson, R. *New J. Phys.* **2018,** *20,* 115004. doi:10.1088/1367-2630/aaec29
20. Laabs, H.; Friberg, A. T. *IEEE J. Quantum Electron.* **1999,** *35,* 198–207. doi:10.1109/3.740741
21. Benedikter, J.; Hümmer, T.; Mader, M.; Schlederer, B.; Reichel, J.; Hänsch, T. W.; Hunger, D. *New J. Phys.* **2015,** *17,* 053051. doi:10.1088/1367-2630/17/5/053051
22. Wang, W.; Qin, Y.; Xiao, Y.; Zhong, L.; Wu, C.; Wang, Z.; Wan, W.; Tang, X. *Appl. Opt.* **2016,** *55,* 5497–5504. doi:10.1364/ao.55.005497
23. Siegman, A.; Arrathoon, R. *IEEE J. Quantum Electron.* **1967,** *3,* 156–163. doi:10.1109/jqe.1967.1074471
24. Pettersson, L. A. A.; Roman, L. S.; Inganäs, O. *J. Appl. Phys.* **1999,** *86,* 487–496. doi:10.1063/1.370757
25. Janitz, E.; Ruf, M.; Dimock, M.; Bourassa, A.; Sankey, J.; Childress, L. *Phys. Rev. A: At., Mol., Opt. Phys.* **2015,** *92,* 043844. doi:10.1103/physreva.92.043844
26. Johnson, S.; Dolan, P. R.; Grange, T.; Trichet, A. A. P.; Hornecker, G.; Chen, Y. C.; Weng, L.; Hughes, G. M.; Watt, A. A. R.; Auffèves, A.; Smith, J. M. *New J. Phys.* **2015,** *17,* 122003. doi:10.1088/1367-2630/17/12/122003
27. Novotny, L. *Principles of Nano-Optics;* Cambridge University Press: Cambridge, UK, 2007. doi:10.1017/cbo9780511813535
28. Bathen, M. E.; Vines, L. *Adv. Quantum Technol.* **2021,** *4,* 2100003. doi:10.1002/qute.202100003
29. Fontana, Y.; Zifkin, R.; Janitz, E.; Rodríguez Rosenblueth, C. D.; Childress, L. *Rev. Sci. Instrum.* **2021,** *92,* 053906. doi:10.1063/5.0049520
30. Ruf, M.; Weaver, M. J.; van Dam, S. B.; Hanson, R. *Phys. Rev. Appl.* **2021,** *15,* 024049. doi:10.1103/physrevapplied.15.024049
31. Bitarafan, M. H.; DeCorby, R. G. *Sensors* **2017,** *17,* 1748. doi:10.3390/s17081748

License and Terms

BEILSTEIN JOURNAL OF NANOTECHNOLOGY

A super-oscillatory step-zoom metalens for visible light

Yi Zhou[*,‡1], Chao Yan[‡2], Peng Tian[‡3], Zhu Li[*2], Yu He[4], Bin Fan[4], Zhiyong Wang[2], Yao Deng[2] and Dongliang Tang[5]

Full Research Paper

Open Access

Address:
[1]Key Laboratory of Optoelectronic Technology and Systems (Chongqing University), Ministry of Education, School of Optoelectronic Engineering, Chongqing University, 174 Shazheng Street, Shapingba, Chongqing 400044, China, [2]Sichuan Jiuzhou Electric Group Co., Ltd, Mianyang 621000, China, [3]School of Mechanical Engineering, Sichuan University, Chengdu, Sichuan, 610065, China, [4]State Key Laboratory of Optical Technologies for Micro-fabrication, Institute of Optics and Electronics, Chinese Academy of Sciences, Chengdu, Sichuan 610209, China and [5]The Key Laboratory for Micro/Nano Optoelectronic Devices of Ministry of Education & Hunan Provincial Key Laboratory of Low-Dimensional Structural Physics and Devices, School of Physics and Electronics, Hunan University, Changsha 410082, China

Email:
Yi Zhou[*] - yi_zhou@cqu.edu.cn; Zhu Li[*] - 1025035201@qq.com

* Corresponding author ‡ Equal contributors

Keywords:
geometric phase; phase-change material; step-zoom lens; super-oscillatory

Beilstein J. Nanotechnol. **2022,** *13,* 1220–1227.
https://doi.org/10.3762/bjnano.13.101

Received: 20 June 2022
Accepted: 10 October 2022
Published: 28 October 2022

This article is part of the thematic issue "Physics and optical applications of all-dieletric nanostructures".

Guest Editor: Z. Han

Abstract

In recent years, the super-oscillation method based on the fine interference of optical fields has been successfully applied to sub-diffraction focusing and super-resolution imaging. However, most previously reported works only describe static super-oscillatory lenses. Super-oscillatory lenses using phase-change materials still have issues regarding dynamic tunability and inflexibility. Therefore, it is vital to develop a flexible and tunable modulation approach for super-oscillatory lenses. In this paper, we propose a super-oscillatory step-zoom lens based on the geometric phase principle, which can switch between two focal lengths within a certain field of view. The designed device consists of nanopillars with high efficiency of up to 80%, and the super-resolution focusing with 0.84 times of diffraction limit is verified by the full-wave simulation. The proposed method bears the potential to become a useful tool for label-free super-resolution microscopic imaging and optical precision machining.

Introduction

Due to the diffraction limit, conventional optical imaging systems are unable to surpass a theoretical resolution of 0.5 λ/NA, where λ is the wavelength and NA is the numerical aperture [1]. Super-resolution optical imaging is of significant scientific and application value, which may lead to a revolution in various fields, such as optical microscopy, optical remote

sensing, subwavelength lithography, and ultra-high-density data storage. Thus, overcoming the barrier of diffraction limit and achieve super-resolution optical imaging has become a hot topic in the research field of optics.

In recent years, a variety of super-resolution optical microscopy techniques have been developed. For instance, stimulated emission depletion microscopy (STED) can realize the localization of single fluorescent molecules with 1 nm accuracy [2], albeit with the disadvantages of required fluorescence labeling and slow image reconstruction. Super-resolution microscopy based on structured light illumination (SIM) can realize a spatial resolution of λ/5 [3]. However, it requires additional designed illumination patterns and image reconstruction. Near-field scanning optical microscopy can achieve super-resolution imaging by detecting surface evanescent fields of objects [4]. Near-field focusing lenses [5] based on surface plasmons can reach a spatial resolution of 22 nm, but the imaging range is limited to the sample surface, causing difficulties in biomedical imaging. Although negative refractive superlenses and hyperbolic metamaterials [6,7] have been experimentally verified for super-resolution imaging, they exhibit high optical loss and are not suitable for far-field imaging. As a result, it is still a huge challenge to achieve unlabeled far-field imaging without image post processing.

Optical super-oscillation is a unique optical phenomenon in which an optical signal can oscillate faster locally than its maximum Fourier frequency in an optical field with low spatial frequency [8]. In principle, there is no theoretical limit of resolution for the super-oscillation field, which provides a novel way to overcome the diffraction limit and realize far-field super-resolution focusing and imaging. Lately, super-oscillatory lenses, through fine modulation of the amplitude and phase of the optical field, have been used in super-resolution imaging [9-11], heat-assisted magnetic recording [12], and optical metrology [13]. In order to form the specific super-oscillatory optical field, common super-oscillatory lenses usually employ simple binary amplitude and binary phase modulation [14,15] to modulate the incident optical field, thus realizing a specific coherent superposition of the output optical field. This modulation method is relatively simple and accessible for fabrication; however, it significantly weakens the device's ability to modulate the optical field effectively, which, in turn, limits the performance of super-oscillatory lenses (e.g., efficiency and large sidelobe). The development of metasurfaces has provided an effective approach to modulating amplitude, phase, and polarization of the optical field at the subwavelength scale [16-22]. Compared with metallic metasurfaces, all-dielectric metasurfaces are characterized by high amplitude transmittance, which is important for super-oscillatory lenses with comparatively low focusing efficiency. Generally, for all-dielectric metasurfaces, the larger the refractive index of the material is, the higher the efficiency will be. Meanwhile, a material with a high refractive index is also beneficial to reduce the aspect ratio of a metasurface device. Therefore, for various optical wavebands, a medium with a high refractive index and low extinction coefficient is usually preferred to be the structural material for super-oscillatory lenses. Nonetheless, most of the previous works only describe invariant super-oscillatory lenses, which only work in a limited number of situations. Researchers have demonstrated achromatic super-resolution focusing at several wavelengths with specifically designed amplitude masks. To achieve a broader waveband, the phase modulation of a super-oscillatory lens is divided into two parts: a super-oscillatory phase with a value of 0 or π from a metasurface and a focusing phase from a commercial achromatic lens [14,15]. However, the focal length of those super-oscillatory lenses is fixed. When super-oscillatory lenses are applied in microscopic imaging, the spatial resolution can be improved a lot, while the field of view decreases proportionally. Under these circumstances, it can be hard to locate the target rapidly within the field of view after switching to the super-oscillatory lens. Although dynamically tunable super-oscillatory lenses could be realized by utilizing phase-change materials [23], the problem of inflexibility still exists.

Here, we propose a super-oscillatory step-zoom lens (SSL) that enables super-resolution focusing with two working modes corresponding to different focal lengths. The designed SSL is composed of a fused silica substrate sandwiched by two metasurfaces based on the geometric phase principle. The optical powers with opposite sign of the front and back metasurfaces can be switched by controlling the polarization state of the incident light. The metasurfaces in our SSL consist of high-aspect-ratio nanopillars with different orientations, which can generate the desired super-oscillation light field with high efficiency. The performance of the proposed SSL is analyzed by electromagnetic simulations to verify the super-resolution focusing capability corresponding to two different focal lengths. Additionally, with our method, the focal plane can be changed by switching the polarization of the incident light instead of moving the lens. We believe this unique property bears a great potential to applied in super-resolution microscopic imaging system.

Design of the Super-Oscillatory Zoom Lens

Similar to previous works [24-26], our proposed SSL can also be designed in two steps: first, a double-layer step-zoom metalens with diffraction-limited imaging performance is designed; second, a super-oscillatory phase is optimized and then superimposed on the stop pupil plane (i.e., the front surface) of

the double-layer step-zoom metalens to realize sub-diffraction step-zoom imaging. For the proof-of-concept example, stop aperture, working wavelength, focal length, and field of view (FOV) of the SSL are 20 μm, 632.8 nm, 20 or 40 μm and 3.2°, respectively.

Essentially, the designed double-layer step-zoom metalens can be regarded as a metasurface doublet cemented by a glass substrate. As illustrated in Figure 1, based on the geometric phase principle, the double-layer step-zoom metalens can be switched between two different focal lengths by controlling the handedness of the incident circularly polarized light. It is superior to the traditional zoom lens since there is no mechanical movement and the image plane of the double-layer step-zoom metalens keeps unchanged. With the geometric optics theory [27], one can get

$$\begin{cases} f_1'\left(f_1'+f_2'\right)=\left(\frac{d}{n}\right)^2 \\ M=\frac{d+nf_1'+nf_2'}{d-nf_1'-nf_2'} \end{cases}, \quad (1)$$

where f_1' and f_2' are the focal lengths of front and rear metasurfaces, d and n are the thickness and refractive index of the glass substrate, and M is the zoom ratio. Here, we choose fused silica glass (the refractive index is about 1.457 at a wavelength of 632.8 nm) as the substrate material. M and d are set to be 2 and 4.86 μm, respectively. The substrate thickness is optimized by ZEMAX for the best optical performance. Certainly, for the practical application, there are more realistic factors that need to be considered. It is worth noting that there is always a tradeoff between performance and practical conditions. f_1' and f_2' were calculated to be ±10 μm and ±8.9 μm. In this way, a double-layer step-zoom lens has been obtained by combining two metasurfaces with opposite optical powers. In order to correct the optical aberration more effectively, we use the even aspherical phase profile rather than the parabolic phase profile for the phase modulation in these two metasurfaces, which can be denoted as:

$$\varphi(r)=\sum_{i=1}^{n} a_i\left(\frac{r}{R}\right)^{2i}, \quad (2)$$

where r is the radial coordinate, R is the normalized radius of the metasurface, n represents the number of polynomial coefficients, and a_i is the optimized phase coefficient.

We used the optical design software ZEMAX to optimize the phase coefficients a_i. In detail, the Binary 2 surface type was

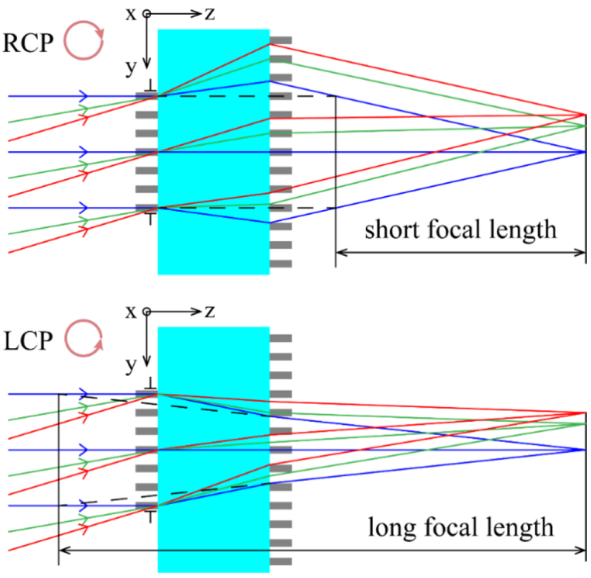

Figure 1: The layout of the double-layer step-zoom metalens.

used to simulate the phase modulation of metasurfaces. Also, we employed the multiple configuration function in ZEMAX to set opposite diffraction orders of the Binary 2 surface type so that the step-zoom focusing can be achieved. The RMS spot of the focal plane for various configurations and FOVs were used as the evaluation criterion. The optimization process was as follows: First, the system parameters, including entrance diameter, FOV, and working wavelength were set. The effective focal length and working F-number operands were added in the merit function as constraints. Then, we set the back focal length and phase coefficients as optimization variables. Two metasurfaces corresponding to the previously calculated focal lengths were designed. It should be noted that more phase coefficients will improve the system performance in theory, whereas this strategy hardly works as the focusing performance is close to the diffraction limit. Therefore, five phase coefficients were used for a good balance between system performance and optimization efficiency referring to the previous work. Second, the two designed metasurfaces are cemented with the fused silica substrate. In turn, the back focal length, phase coefficients, and substrate thickness were added as optimization variables in order to minimize the RMS focal spot size for different configurations and FOVs. Finally, the optimized substrate thickness is 3.4 μm, and the back focal length is 23.7 μm. The phase coefficients for the phase modulation of the front and back metasurfaces with a normalized radius of 10 μm are presented in Table 1.

Now, the double-layer step-zoom metalens was obtained by the optimization process above. This lens can achieve diffraction-

Table 1: Optimized phase coefficients of the front and back metasurfaces.

	Diameter	a_1	a_2	a_3	a_4	a_5
front metasurface	20 μm	−48.8883	−0.3008	2.1089	0.3695	−0.7718
rear metasurface	30 μm	55.0949	2.7000	−4.2203	1.7344	−0.2596

limited imaging with two working modes corresponding to different focal lengths.

Referring to a previously reported work [28], if a specially designed super-oscillatory phase is superimposed on the stop pupil surface (i.e., the front metasurface) of this double-layer step-zoom metasurface, the proposed SSL will be realized. The intensity distribution in the image plane of the SSL can be calculated by diffraction propagation methods, such as angular spectrum diffraction. To obtain a specific sub-diffraction focal spot, we developed a multiply constrained optimization model with a single objective. The objective function is defined as the central intensity of the sub-diffraction focal spot with constraints of the full width at half maximum (FWHM) of the focal spot, the maximum relative intensity of the sidelobe within the local field of view, and the super-oscillation phase distribution. The mathematical expression of this model is as follows:

$$\begin{aligned} &\text{Objective:} \quad \max I(0) \\ &\text{Constraints:} \quad \mathrm{FWHM} \le G \cdot \frac{0.5145\lambda}{\mathrm{NA}} \\ &\qquad \frac{I(\rho)}{I(0)} \le M, \frac{0.61\lambda}{\mathrm{NA}} < \rho \le L \\ &\qquad \varphi_{\mathrm{so}}(r_i) \in \{0, \pi\}, \end{aligned} \tag{3}$$

where G is the sub-diffraction factor, M indicates the ratio between the maximum intensity of the sidelobe in the local region L and the central intensity of the sub-diffraction focal spot, ρ is the radial coordinate in the focal plane, and r_i represents the radius of the i-th annular ring of the super-oscillatory phase profile. To ensure the optimization efficiency, the super-oscillation phase distribution is divided into N rings equally along the radial direction. Each annular ring takes a phase value of 0 or π. In our proposed SSL, the FWHM is set to be 0.84 times of the diffraction limit (calculated by 0.5145λ/NA, G is set to be 0.84), and M is set to be 0.2. According to the particle swarm optimization algorithm [29], the final radially normalized π-phase-jump positions of the super-oscillation phase are 0.15, 0.2 and 0.4, respectively.

The phase modulation of the super-oscillatory step-zoom metalens can be divided in two parts, namely focusing phase and super-oscillatory phase. Phase modulation is achieved by TiO_2 nanopillars based on the geometric phase, which is inherently polarization-sensitive. The front and rear metasurfaces have the opposite optical power and work as a concave lens and a convex lens for the incident right-handed circularly polarized (RCP) light, or a convex lens and a concave lens for the incident left-handed circularly polarized (LCP) light. For the super-oscillatory phase, it takes the value of 0 or π, so the modulation remains invariant for incident left-handed or right-handed circularly polarized light. It means that the super-oscillatory step-zoom metalens can achieve super-resolution focusing for both left-handed and right-handed circularly polarized light. The proposed SSL can be achieved with the optimization method above. The phase distribution, in turn, of the front metasurfaces is finally obtained by superimposing the optimized super-oscillatory phase. As the LCP light impinges on the SSL, it works with a long focal length. It can switch to the short focal length with incident RCP light. As shown in Figure 2, the front and rear metasurfaces have the opposite optical powers. In this way, we can realize sub-diffraction step-zoom focusing with the designed SSL.

To dynamically modulate the phase distribution, we designed a unit cell structure based on the geometric phase (i.e., Pancharatnam–Berry phase) principle [30,31]. Generally, metasurfaces based on geometric phases are easier to process, and the phase modulation in the whole 2π range can be achieved by simply changing the orientation of the unit cell. Also, the higher the refractive index of the material in the visible band is, the weaker the coupling among the unit cells will be, which leads to a higher efficiency of the metasurface. Thus, rectangular nanopillars composed of titanium dioxide (the refractive index is 2.87 at a wavelength of 632.8 nm) are used as unit cells of the two metasurfaces. The fused silica glass is used as substrate in the SSL. Theoretically, for the metasurface based on the geometric phase principle, the phase modulation of the transmitted RCP light is exactly twice of the orientation of the unit cell under the LCP incidence. The field modulation of the unit cells with various orientations and sizes were numerically simulated by CST Microwave Studio. After a parameter sweep, as illustrated in Figure 3a, the unit cell was selected to obtain high polarization conversion efficiency with length L = 200 nm, width W = 80 nm, height H = 600 nm, and period

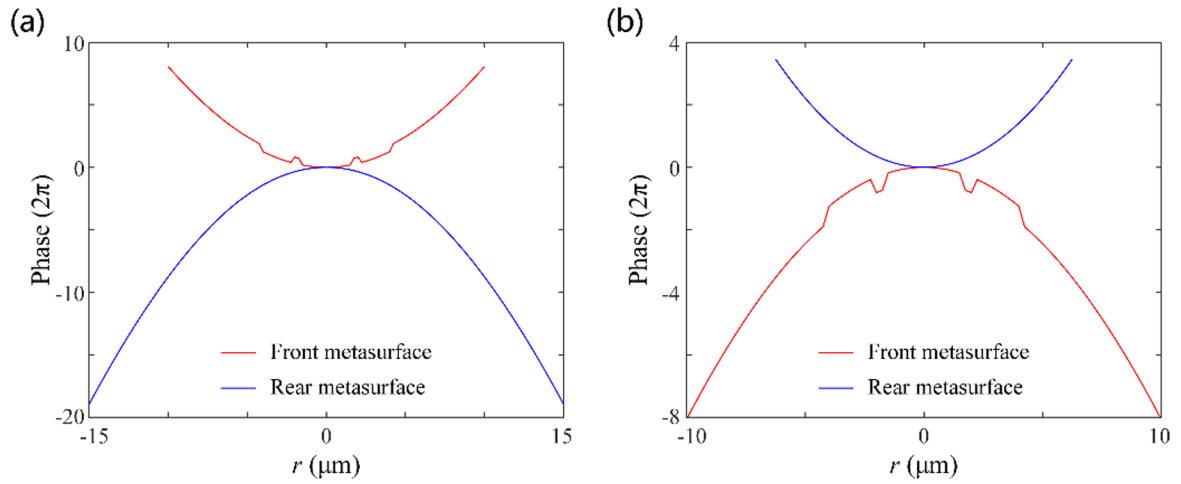

Figure 2: Phase profiles of the front and rear metasurfaces for (a) short and (b) long focal lengths.

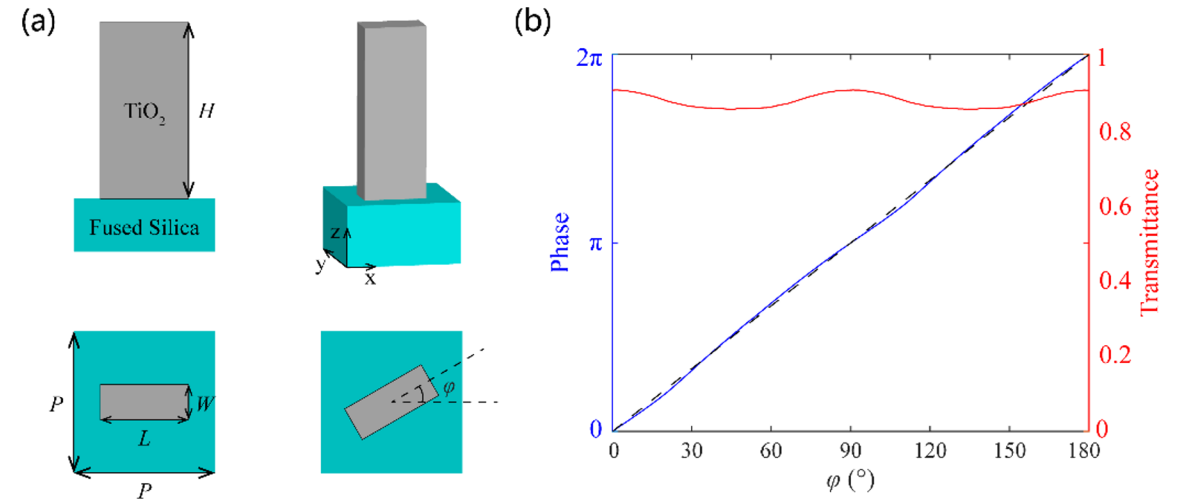

Figure 3: (a) Schematic of a TiO_2 rectangular nanopillar. (b) Simulated transmittance and phase modulations of the unit cells with different orientations. The black dashed line represents the theoretical modulated phase.

P = 250 nm × 250 nm. It is demonstrated in Figure 3b that the transmittance varies only little for different orientation angles and the modulated phase changes almost linearly with a factor of two, which also proves the geometric phase principle and the excellent performance of the designed unit cells.

Simulation Results and Performance Analysis

We also use CST to perform the full-wave simulation for the designed SSL, setting the wavelength to 632.8 nm and incident angle of 0°, 1.1°, and 1.6° along the x-axis direction. Since the whole simulation area is too large and time-consuming for a calculation, we employed the following method to improve the simulation speed: First, we simulated the interaction between the light and the metasurface structure by CST and extracted the optical field at 0.3 μm from the back surface of the SSL. Then, we utilized the scalar angular spectrum diffraction method to calculate the diffraction propagation behind the extracted field, and thus obtained the optical field distribution at a specific plane.

As shown in Figure 4 and Figure 5, we calculated the intensity distribution of the optical field along the propagation direction for various polarization states (corresponding to different focal lengths) and incident angles. The sub-diffraction spots are all well formed in the designed image plane for all cases. In Figure 4d–i and Figure 5d–i, the calculated intensity distributions for the image plane of z = 23.7 μm are shown. It is clearly

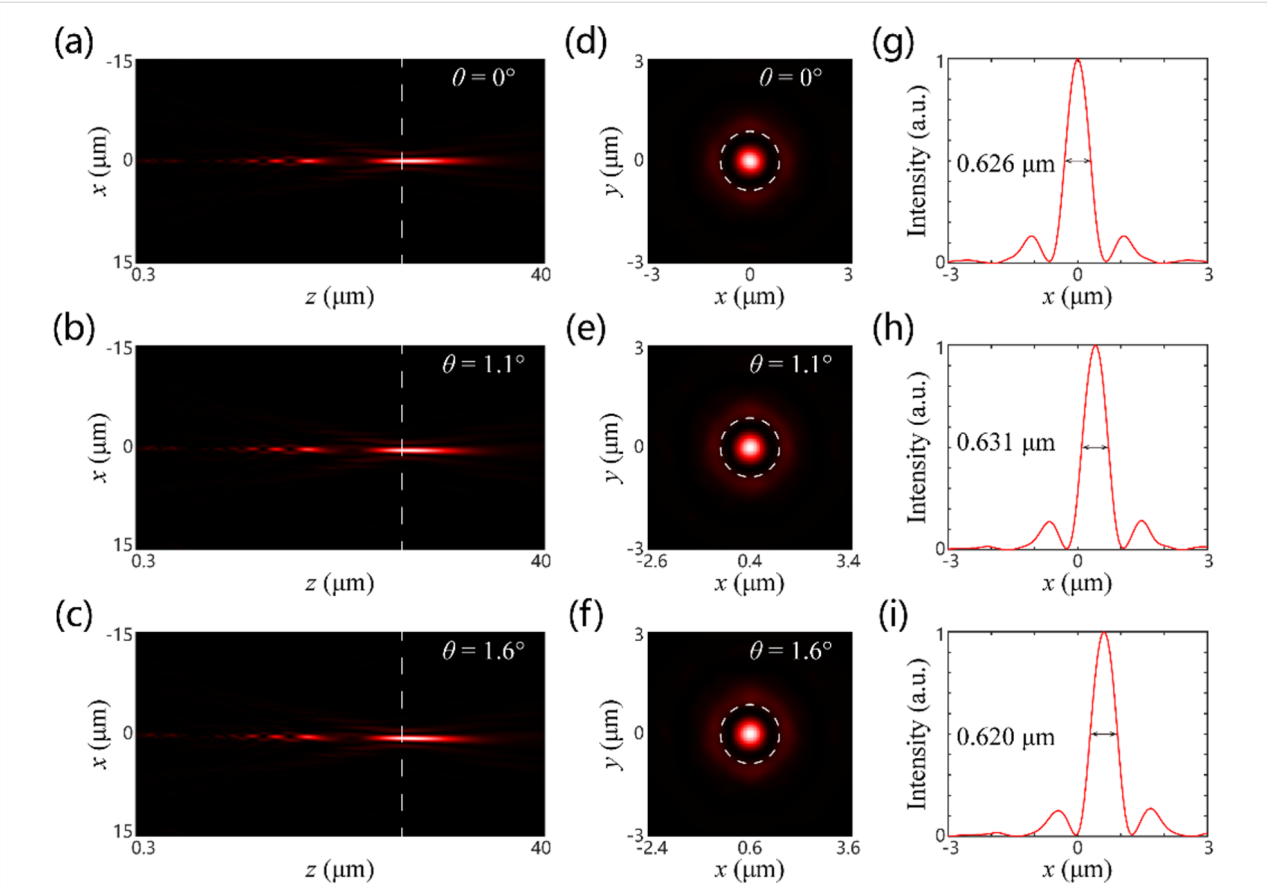

Figure 4: Simulated intensity distributions for different incident angles with RCP incidence corresponding to the SSL with short focal length. (a–c) Intensity distributions along the propagating direction. The dashed white lines represent the focal plane of the SSL. (d–f) Intensity distributions in the focal plane. The dashed white circles represent the diffraction-limited focal spot (Airy disk). (g–i) Intensity distributions of the sub-diffraction spot along the *x*-direction.

indicated that the FWHMs of the sub-diffraction focal spots are very close to the designed value (0.612 and 1.128 μm for the short and long focal lengths, respectively). The difference between the simulation results and the theoretical values is mainly attributed to the insufficient sampling and optical modulation deviation of metasurface. Nevertheless, the simulation results still demonstrate the super-diffraction focusing performance of the SSL for two different focal lengths, which illustrates the effectiveness of our proposed method. The transverse displacements of the sub-diffraction focal spots were calculated for various incident angles, as illustrated in Figure 4g–i and Figure 5g–i. The values are 0, 0.4 and 0.6 μm, and 0, 0.7 and 1 μm, respectively. They are consistent with the theoretical results of 0, 0.38 and 0.56 μm, and 0, 0.77 and 1.12 μm, respectively. In addition, the focusing efficiencies were calculated to be, respectively, 9.98%, 6.45% and 4.99%, and 22.24%, 13.27% and 7.10% for different incident angles. Here, the focusing efficiency is defined as the ratio between the intensity in the main lobe region of the super-diffraction focal spot and the total incident intensity. It is found that the focusing efficiencies for the short focal length of the SSL are all smaller than those for the long focal length of SSL. Also, the focusing efficiency decreases with the increase of the incident angle. This suggests that there is a more pronounced optical aberration of the short focal length than of the long focal length, which corresponds well with the traditional geometric optical theory. It should be noted that the low focusing efficiency of the SSL arises from the redistribution of the optical field energy. This is a typical feature of the optical super-oscillation phenomenon in which the main lobe of the super-diffraction spot is often surrounded by some sidelobes with considerable intensity, leading to the unavoidable energy loss.

Discussion

For simplification, we did not take into consideration the influence of factors such as the amplitude and phase modulation deviation of the metasurface, which may lead to the degradation of the sub-diffraction focusing performance. The first is the phase modulation error due to discrete sampling. In the design, it is assumed that the physical size of the unit cell could be infi-

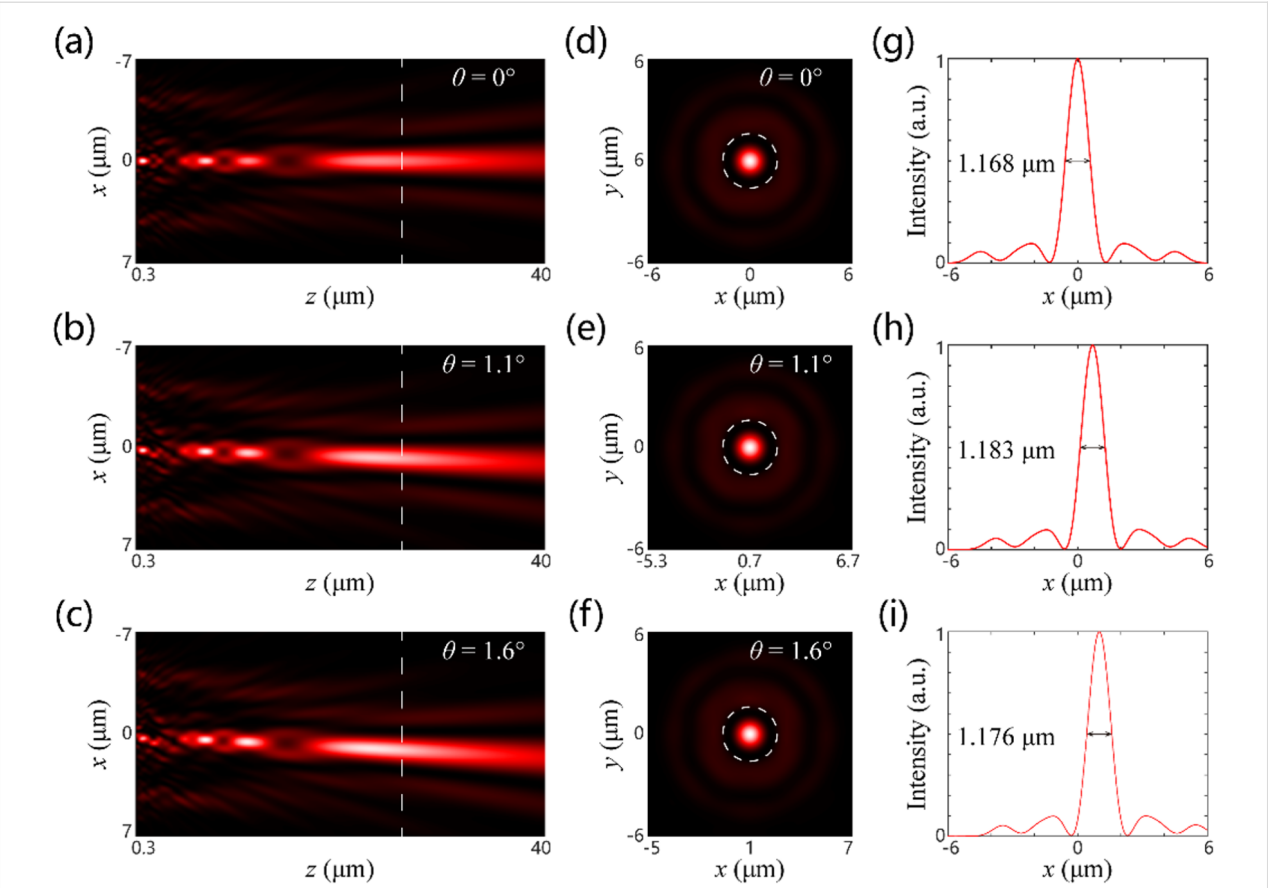

Figure 5: Simulated intensity distributions for different incident angles with LCP incidence corresponding to the SSL with long focal length. (a–c) Intensity distributions along the propagating direction. The dashed white lines represent the focal plane of the SSL. (d–f) Intensity distributions in the focal plane. The dashed white circles represent the diffraction-limited focal spot (Airy disk). (g–i) Intensity distributions of the sub-diffraction spot along the *x*-direction.

nitely small for the convenience of optimization. In fact, a unit cell has a specific size and could only achieve a step-like discrete phase, which, in turn, deviates from the desired phase modulation. Second, the inhomogeneous amplitude modulation also contributes to performance degradation. In our design, it is assumed that only phase modulation with uniform amplitude is achieved by the metasurface. Nonetheless, due to the shadowing effect and coupling phenomenon among unit cells, the transmittance of the unit cells is affected by the incident angle and the orientation of unit cells. Third, the residual co-polarization component could lead to noticeable stray light. As we used a double-layer metasurface based on the geometric phase principle, there are two polarization conversions. For the ideal case, the incident LCP will be converted to RCP, and then converted to LCP again. However, the polarization conversion efficiency cannot reach 100%, which would cause some stray light in the SSL. To address these problems, the influence of discrete sampling errors could be relieved using a catenary structure, while the influence of stray light could be minimized by using a metasurface design based on the propagation phase principle.

In principle, there are always inevitable sidelobes around the sub-diffraction hotspot in the super-oscillatory phenomenon, which are detrimental to imaging and render low efficiency and limited FOV. To solve the problem, some methods have been used in super-oscillatory imaging, such as confocal scanning imaging and specially designed super-oscillatory spots [9,10]. Nevertheless, the low efficiency may be tolerable for some specific applications, such as observing target objects with high illumination intensity in microscopic systems. High-sensitivity detectors and long exposure time would be also advantageous.

Conclusion

In summary, we have proposed a super-oscillatory step-zoom lens composed of titanium dioxide nanopillars. The device operates at a wavelength of 632.8 nm and has two working modes with long or short focal lengths, corresponding to the telescopic and wide-angle application scenarios, respectively. In the proof-of-principle, the super-oscillatory step-zoom lens can achieve super-resolution focusing in two separate focusing cases. The simulation results show good agreement with the

theory. This paper provides a novel method for constructing a dynamically tunable super-oscillatory lens, which has great potential applications in the field of super-resolution microscopic imaging and optical precision machining.

Funding

National Natural Science Foundation of China (62105046); Natural Science Foundation of Chongqing (cstc2021jcyj-msxmX0796), Entrepreneurship and Innovation Support Plan for the Returned Overseas Chinese Scholars (cx2021103), the Sichuan Science and Technology Program (2022YFQ0007).

ORCID® iDs

Yi Zhou - https://orcid.org/0000-0003-1529-1114

References

1. Abbe, E. *Arch. Mikrosk. Anat.* **1873,** *9,* 413–468. doi:10.1007/bf02956173
2. Wildanger, D.; Medda, R.; Kastrup, L.; Hell, S. W. J. *J. Microsc. (Oxford, U. K.)* **2009,** *236,* 35–43. doi:10.1111/j.1365-2818.2009.03188.x
3. Gustafsson, M. G. L. *J. Microsc. (Oxford, U. K.)* **2000,** *198,* 82–87. doi:10.1046/j.1365-2818.2000.00710.x
4. Courjon, D.; Bainier, C. *Rep. Prog. Phys.* **1994,** *57,* 989–1028. doi:10.1088/0034-4885/57/10/002
5. Liu, Z.; Lee, H.; Xiong, Y.; Sun, C.; Zhang, X. *Science* **2007,** *315,* 1686. doi:10.1126/science.1137368
6. Zhang, X.; Liu, Z. *Nat. Mater.* **2008,** *7,* 435–441. doi:10.1038/nmat2141
7. Lee, D.; So, S.; Hu, G.; Kim, M.; Badloe, T.; Cho, H.; Kim, J.; Kim, H.; Qiu, C.-W.; Rho, J. *eLight* **2022,** *2,* 1. doi:10.1186/s43593-021-00008-6
8. Berry, M. V.; Popescu, S. *J. Phys. A: Math. Gen.* **2006,** *39,* 6965–6977. doi:10.1088/0305-4470/39/22/011
9. Rogers, E. T. F.; Lindberg, J.; Roy, T.; Savo, S.; Chad, J. E.; Dennis, M. R.; Zheludev, N. I. *Nat. Mater.* **2012,** *11,* 432–435. doi:10.1038/nmat3280
10. Qin, F.; Huang, K.; Wu, J.; Teng, J.; Qiu, C.-W.; Hong, M. *Adv. Mater. (Weinheim, Ger.)* **2017,** *29,* 1602721. doi:10.1002/adma.201602721
11. Tang, D.; Wang, C.; Zhao, Z.; Wang, Y.; Pu, M.; Li, X.; Gao, P.; Luo, X. *Laser Photonics Rev.* **2015,** *9,* 713–719. doi:10.1002/lpor.201500182
12. Yuan, G.; Rogers, E. T. F.; Roy, T.; Shen, Z.; Zheludev, N. I. *Opt. Express* **2014,** *22,* 6428–6437. doi:10.1364/oe.22.006428
13. Yuan, G. H.; Zheludev, N. I. *Science* **2019,** *364,* 771–775. doi:10.1126/science.aaw7840
14. Yuan, G. H.; Rogers, E. T.; Zheludev, N. I. *Light: Sci. Appl.* **2017,** *6,* e17036. doi:10.1038/lsa.2017.36
15. Li, Z.; Zhang, T.; Wang, Y.; Kong, W.; Zhang, J.; Huang, Y.; Wang, C.; Li, X.; Pu, M.; Luo, X. *Laser Photonics Rev.* **2018,** *12,* 1800064. doi:10.1002/lpor.201800064
16. Zhang, Q.; Dong, F.; Li, H.; Wang, Z.; Liang, G.; Zhang, Z.; Wen, Z.; Shang, Z.; Chen, G.; Dai, L.; Chu, W. *Adv. Opt. Mater.* **2020,** *8,* 1901885. doi:10.1002/adom.201901885
17. Lalanne, P.; Chavel, P. *Laser Photonics Rev.* **2017,** *11,* 1600295. doi:10.1002/lpor.201600295
18. Huang, K.; Qin, F.; Liu, H.; Ye, H.; Qiu, C.-W.; Hong, M.; Luk'yanchuk, B.; Teng, J. *Adv. Mater. (Weinheim, Ger.)* **2018,** *30,* 1704556. doi:10.1002/adma.201704556
19. Luo, X. *Sci. China: Phys., Mech. Astron.* **2015,** *58,* 594201. doi:10.1007/s11433-015-5688-1
20. Dou, K.; Xie, X.; Pu, M.; Li, X.; Ma, X.; Wang, C.; Luo, X. *Opto-Electron. Adv.* **2020,** *3,* 19000501. doi:10.29026/oea.2020.190005
21. Wang, Y.; Fan, Q.; Xu, T. *Opto-Electron. Adv.* **2021,** *4,* 200008. doi:10.29026/oea.2021.200008
22. Gao, H.; Fan, X.; Xiong, W.; Hong, M. *Opto-Electron. Adv.* **2021,** *4,* 210030. doi:10.29026/oea.2021.210030
23. Wang, Q.; Rogers, E. T. F.; Gholipour, B.; Wang, C.-M.; Yuan, G.; Teng, J.; Zheludev, N. I. *Nat. Photonics* **2016,** *10,* 60–65. doi:10.1038/nphoton.2015.247
24. Buralli, D. A.; Morris, G. M. *Appl. Opt.* **1989,** *28,* 3950–3959. doi:10.1364/ao.28.003950
25. Arbabi, A.; Arbabi, E.; Kamali, S. M.; Horie, Y.; Han, S.; Faraon, A. *Nat. Commun.* **2016,** *7,* 13682. doi:10.1038/ncomms13682
26. Groever, B.; Chen, W. T.; Capasso, F. *Nano Lett.* **2017,** *17,* 4902–4907. doi:10.1021/acs.nanolett.7b01888
27. Goodman, J. W. *Introduction to Fourier Optics;* W. H. Freeman, 2005.
28. Li, Z.; Wang, C.; Wang, Y.; Lu, X.; Guo, Y.; Li, X.; Ma, X.; Pu, M.; Luo, X. *Opt. Express* **2021,** *29,* 9991–9999. doi:10.1364/oe.417884
29. Jin, N.; Rahmat-Samii, Y. *IEEE Trans. Antennas Propag.* **2007,** *55,* 556–567. doi:10.1109/tap.2007.891552
30. Berry, M. V. *J. Mod. Opt.* **1987,** *34,* 1401–1407. doi:10.1080/09500348714551321
31. Chen, X.; Huang, L.; Mühlenbernd, H.; Li, G.; Bai, B.; Tan, Q.; Jin, G.; Qiu, C.-W.; Zhang, S.; Zentgraf, T. *Nat. Commun.* **2012,** *3,* 1198. doi:10.1038/ncomms2207

License and Terms

BEILSTEIN JOURNAL OF NANOTECHNOLOGY

Double-layer symmetric gratings with bound states in the continuum for dual-band high-*Q* optical sensing

Chaoying Shi[1], Jinhua Hu[*2], Xiuhong Liu[*1], Junfang Liang[2], Jijun Zhao[2], Haiyan Han[1] and Qiaofen Zhu[1]

Full Research Paper

Open Access

Address:
[1]School of Mathematics and Physics Science and Engineering, Hebei University of Engineering, Handan, Hebei 056038, P. R. China and [2]School of Information and Electrical Engineering, Hebei University of Engineering, Handan, Hebei 056038, P. R. China

Email:
Jinhua Hu[*] - hujh84@hebeu.edu.cn; Xiuhong Liu[*] - liuxiuhong@hebeu.edu.cn

* Corresponding author

Keywords:
bound states in the continuum; dual band; high quality factor; localized optical field; nonlinear optics; optical sensing

Beilstein J. Nanotechnol. **2022,** *13,* 1408–1417.
https://doi.org/10.3762/bjnano.13.116

Received: 09 July 2022
Accepted: 11 November 2022
Published: 25 November 2022

This article is part of the thematic issue "Physics and optical applications of all-dieletric nanostructures".

Guest Editor: Z. Han

Abstract

Herein, we theoretically demonstrate that a double-layer symmetric gratings (DLSG) resonator consisting of a low-refractive-index layer sandwiched between two high-contrast gratings (HCG) layers, can host dual-band high-quality (*Q*) factor resonance. We find that the artificial bound states in the continuum (BIC) and Fabry–Pérot BIC (FP-BIC) can be induced by optimizing structural parameters of DLSG. Interestingly, the artificial BIC is governed by the spacing between the two rectangular dielectric gratings, while the FP-BIC is achieved by controlling the cavity length of the structure. Further, the two types of BIC can be converted into quasi-BIC (QBIC) by either changing the spacing between adjacent gratings or changing the distance between the upper and lower gratings. The simulation results show that the dual-band high-performance sensor is achieved with the highest sensitivity of 453 nm/RIU and a maximum figure of merit (FOM) of 9808. Such dual-band high-*Q* resonator is expected to have promising applications in multi-wavelength sensing and nonlinear optics.

Introduction

High quality (*Q*) factor resonance in nanophotonics has attracted considerable attention in the past decades due to its wide applications in narrow-band filters [1], nonlinear optics [2], optical sensors [3] and lasers [4]. To date, most researchers have focused their interests on the single high-*Q* resonance of various structures and proposed different types of structures to achieve high-*Q*-factors, such as metallic structures based on surface plasmon resonances [5,6], Mie resonance-based dielectric structures [7,8], and high-contrast grating (HCG) structures in periodic subwavelengths [9,10]. Among them, HCG structures built on silicon-on-insulator (SOI) substrates establish a new platform for integrated optics as well as optical sensing

[11,12] owing to its high reflectivity in bandwidth (>99%) and compatibility with the complementary metal oxide semiconductor (CMOS) processes [13,14]. It has been shown that the HCG system can support the optical bound states in the continuum (BICs) [15-18]. BIC plays an important role in determining the characteristics of the radiative high-Q resonance [17]. However, there are fewer reported HCG structures that support dual-band high-Q resonances. Differing from a single high-Q resonance, dual-band high-Q resonances allows for simultaneous modification of the line shape at two spectral locations [19], which provides multiple detection points for sensing applications.

In 1929, von Neumann and Wigner first proposed the BIC theory shortly after the advent of quantum mechanics [20], which was then extended to acoustics, electromagnetism, and other fields [21-24]. A true BIC has an infinite Q-factor and vanishing resonant linewidth, and this can only exist in an ideal lossless infinite structure or in extreme values of the parameters [25,26]. The structures that are commonly used to induce the BIC include metasurfaces [27,28], dielectric gratings [29,30], photonic crystals [31], and whispering-gallery resonators [32]. In 2016, Wang et al. investigated a symmetry-protected BIC (SP-BIC) supported by a slotted HCG structure in both TE and TM polarization scenarios [17]. When the spatial symmetry of the mode is incompatible with the symmetry of the outgoing wave, the coupling coefficient vanishes thus inducing the SP-BIC. In 2019, Doskolovich et al. reported that a Fabry–Pérot BIC (FP-BIC) can be excited by varying the distance of the same grating ridge on the surface of a single-mode dielectric slab waveguide [33]. Generally speaking, an FP-BIC can be formed when the spacing between two resonances is changed so that the sum of the round-trip phase shifts is an integer multiple of 2π. In 2020, Lee et al. showed that photonic lattices with a symmetric cladding structure support Friedrich–Wintgen BIC (FW-BIC), which occurs due to the destructive interference of two resonances coupled to the same radiation channel [18]. From a practical application perspective, the BIC must be converted to quasi-BIC (QBIC) with a finite Q-factor or the full width at half maximum (FWHM) so they can be accessed by an external excitation, such as a plane wave [34,35]. QBIC has been extensively utilized in optical absorbers [36,37], lasers [38], filters [30], and sensors [39]. Particularly, the QBIC sensor enables highly accurate detection of environmental changes by reading variations in the spectrum. However, numerous research works have focused on the BIC mechanism of single-mode resonance [26,28], which may limit its application.

In this work, we proposed a double-layer symmetric gratings (DLSG) structure supporting artificial BIC and FP-BIC, which is composed of highly reflecting HCG layers surrounding a low refractive index layer. The artificial BIC was excited by tuning the spacing between two adjacent dielectric gratings. More importantly, we found that the modes can be evolved by controlling the grating gaps. Then, the FP-BIC is induced by varying the cavity length of the structure. Finally, we achieved a dual-band high-Q resonator for optical sensing, which is potentially valuable for applications in multi-wavelength sensing.

Structure and Principle

The geometry of our designed structure is shown in Figure 1, where the high refractive index rectangular dielectric gratings (RDGs) are periodically arranged at the top/bottom of the low refractive index layer and are symmetrical. Besides, the structure possesses a translational period (Λ) along the x-direction and an infinite ridge along the y-direction. A unit cell contains two RDGs, and the spacing between the two RDGs in a period and not in a period are d and l, respectively. The side length of the RDG is w and the thickness of the low refractive layer is h. Moreover, the rigorous coupled-wave analysis (RCWA) [40,41] is used to design the structure of the device and analyze the spectral information, which is combined with the finite element method (FEM) [42] to compute the complex eigenfrequencies.

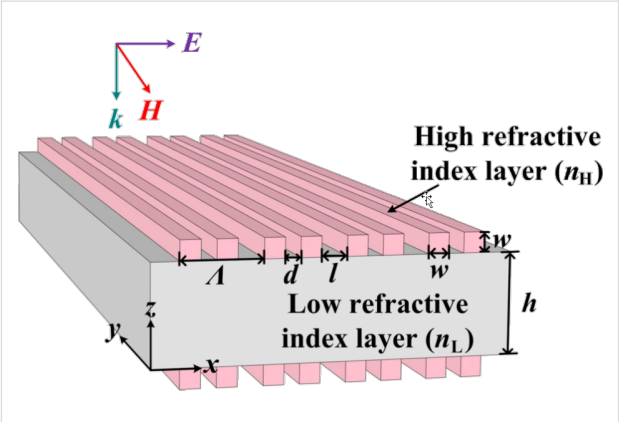

Figure 1: Schematic of the double-layer symmetric gratings structure.

In order to investigate the resonance properties of dielectric gratings, we used here a dimensionless parameter α to measure the grating spacing of the DLSG structure by varying the distance between adjacent RDGs, which is defined as follows [26,43]:

$$\alpha = \frac{d-l}{d+l}. \quad (1)$$

The complex eigenfrequencies of the DLSG structure were then obtained by the FEM, and can be described as $N = \omega - i\gamma$, where ω and γ are the real and imaginary parts of N, respectively. The ω indicates the resonant frequency, and the γ refers to the radiative leakage of the electromagnetic energy stored in the leaky

mode [44]. It allows expressing the radiative Q-factor in the following form:

$$Q = \frac{\omega}{2\gamma}. \tag{2}$$

The BIC induced based on the structure of the HCG gratings can be divided into two categories, one is the BIC that is forbidden due to the coupling of symmetry with free space at normal incidence, and the other is the BIC that can occur by changing any structural parameter independent of the symmetry type [45]. In the proposed symmetric structure, we were able to find the artificial BIC by the Brillouin band folding phenomenon resulting from changing the spacing of the grating. Interestingly, the FP-BIC is obtained by varying the cavity length of the DLSG to satisfy the transverse resonance principle.

Results and Discussion

As an example, the high refractive index layer of the structure depicted in Figure 1 is silicon (n_H = 3.47) and the low refractive index layer is SU-8 (n_L = 1.57). The other structural parameters are w = 200 nm, h = 1000 nm, and Λ = 800 nm. Besides, the whole structure is suspended in vacuum (n_c = 1.0) and normally incident by a TM-polarized plane wave (H//y).

By varying the spacing d of the RDGs, the reflection spectra were obtained for resonances with different α values, as shown in Figure 2. The mode of the resonances can be regulated by controlling the spacing between the two RDGs, which is essentially a splitting of the simple mode. It can be seen from Figure 2 that the linewidth of the spectrum completely disappears when α = 0, which means that the Q-factor is infinite and the ideal BIC appears (points A and B). Furthermore, it is noticed that the evolution of the two modes is symmetric with respect to α = 0. Here, we take α > 0 as an example to analyze. The resonance evolves into two modes (referred to as the nonsimple state) when 0 < α < 0.5, and the QBIC near the points A and B possess a high Q-factor. When 0.5 < α < 0.75, the two resonances start to merge into a single one (referred to as the simple state), and the Q-factor is lower at this time. Therefore, the evolution of single and double resonances can be controlled by changing the spacing of RDGs. Moreover, changing the grating spacing allows the emergence of BIC.

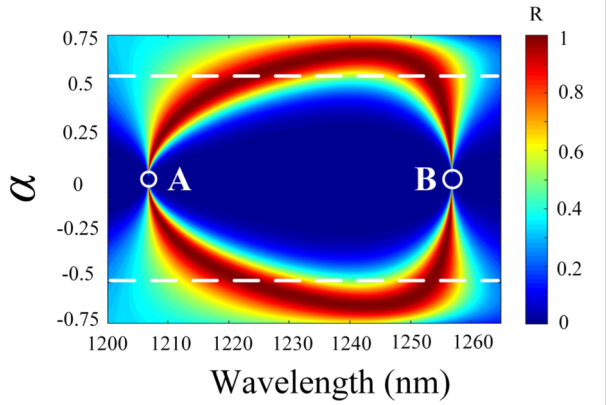

Figure 2: Reflection spectra mapping of the DLSG-based structure with respect to wavelength and α.

The reflection spectra calculated using RCWA when α = 0.1, 0.35, 0.55, 0.75 are given in Figure 3a, which shows in more detail the tuning of the RDGs spacing on single and double resonances. As α decreases, the linewidth of the resonance also

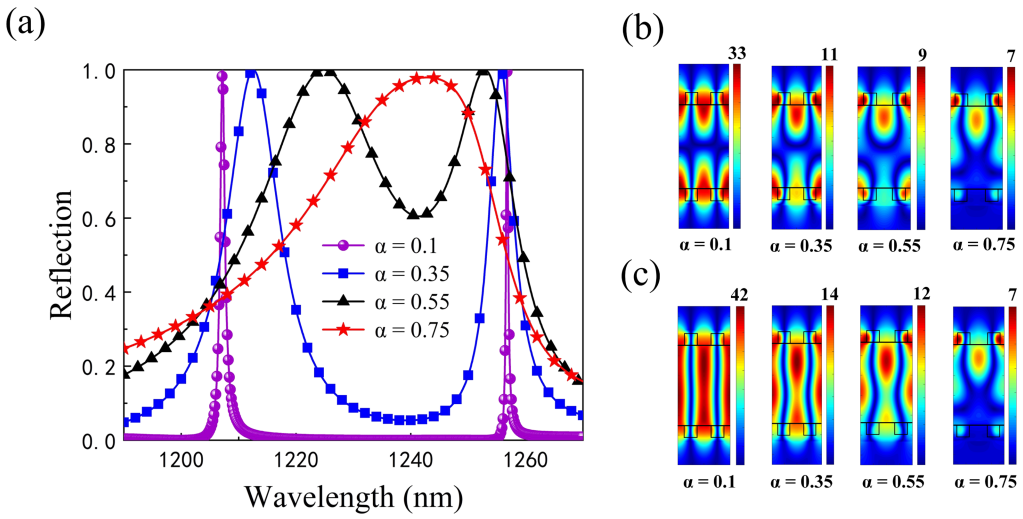

Figure 3: a) Reflection spectra of the structure with different α values. The magnetic field contours |Hy| for b) mode 1 and c) mode 2 at different α values, respectively.

decreases and evolves from the simple state to the nonsimple state until α = 0. At that time, the spectral linewidths of the two resonance peaks almost completely disappear and the ideal BIC is obtained. Furthermore, the magnetic field distributions of the two modes under resonance are calculated as shown in Figure 3b and Figure 3c. The localized field energy of both modes decreases as α increases, and the magnetic field distributions of both modes gradually converge to an identical one, thus achieving the simple merged state for the two modes (α = 0.75).

Figure 4 shows the complex eigenfrequencies of the two modes at different α values. As seen in Figure 4, the ω value of mode 1 shows a tendency to increase and then it decreases as α grows; however, the trend of mode 2 is exactly the opposite. Moreover, the ω values of the two modes are symmetrical at α = 0. An increase of α from 0 to 0.75 implies the evolution of the two resonances, and the ω values of the two modes overlap when α = 0.75, realizing the simple state of the mode. When α = 0, the complex eigenfrequencies of mode 1 and mode 2 are 248.08 and 238.35 THz, respectively. In addition, it is apparent that the γ value of both modes are close to zero, which means that there is almost no radiation loss resulting in an infinite value for the *Q*-factor (the ideal BIC). Here, the spacing between each RDG is completely equal and exactly the same as the side length of the RDG ($d = l = w$ = 200 nm), at which time the device is a periodic structure with a double-layer single grating. Moreover, the γ value of both modes increases with α, which leads to an increase in the radiation loss of the device and a decrease in the *Q*-factor. By physically varying the spacing of the RDG, the modes at the edge of the first Brillouin zone now lie at the gamma point (the center of the first Brillouin zone), thus resulting in an artificial BIC caused by the Brillouin folding phenomenon [45]. Such BIC is dominated by the electric toroidal dipole rather than the SP-BIC dominated by the magnetic dipole [46]. As a result, instead of having to break the symmetry of the structure, as in the case of SP-BIC, a simple change in the grating spacing can transform the BIC into a QBIC, leading to high-*Q* resonance.

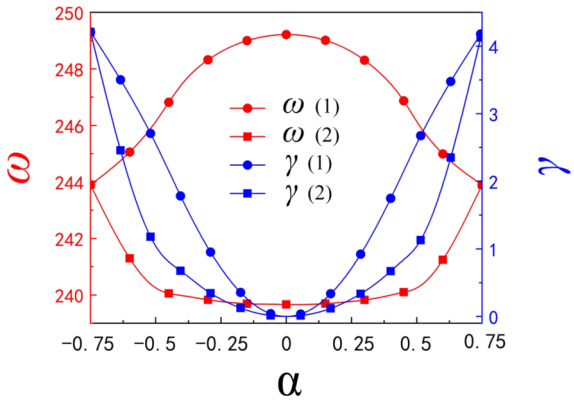

Figure 4: The complex eigenfrequencies of the two modes with respect to α.

The relationship between the radiative *Q*-factors calculated according to Equation 2 and the α values for both modes is investigated in Figure 5. It can be found that our calculated radiative *Q*-factor (dots) shows an inverse square dependence on α and agrees well with the theoretical prediction ($Q_0 = C\alpha^{-2}$, solid

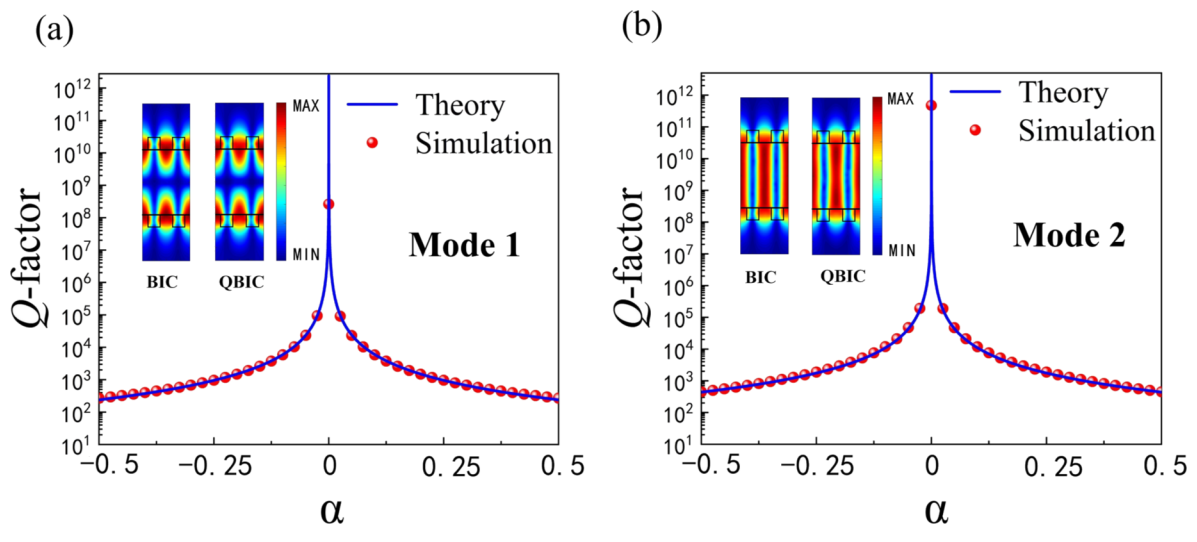

Figure 5: The *Q*-factor as a function of α of a) mode 1 and b) mode 2. The insets show the field distributions of the corresponding BIC and QBIC for the two modes.

line. Here, C is a constant determined by the design of the structure surface) [26]. In addition, the Q-factors of mode 1 and mode 2 are 2.6285×10^8 and 4.7754×10^{11}, respectively. It is noted that the Q-factor of mode 1 is always lower than that of mode 2 for the same value of α, which is attributed to different distributions of the localized optical field in the two modes. As seen in Figure 3b and Figure 3c, the optical field of mode 1 is mainly localized near the upper and lower gratings at the same α value, whereas most of the optical field in mode 2 is confined to the cavity. To physically obtain a high Q-factor, it is required that the optical field is trapped in a grating-based resonant cavity.

Theoretically, the BIC is a completely confined bound mode and cannot be excited [17]. However, the simulation results show that the artificial BIC can be transformed into a high-Q resonance with a Q-factor controlled by the spacing of the grating. The artificial BIC is perturbed by changing the grating spacing, and when overly perturbed (the spacing between the gratings is large) the two modes evolve into a simple mode with low-Q resonance. Notably, the high Q-factor appears in the near artificial BIC region (the insets in Figure 5), which is the region of enhanced field effects at energy points close to the BIC with limited but high Q-factors (QBIC) [47].

The change in spacing between RDGs can tune the evolution of the two modes and achieve artificial BIC. Then we fixed α and investigated the reflection spectra at different cavity lengths h by using RCWA. On the one hand, the two modes start to evolve into one mode when $\alpha > 0.5$, and on the other hand, a smaller α value can ensure a higher Q-factor. Therefore, we fixed $\alpha = 0.15$, and studied the reflection spectra for different cavity lengths at the same α in the presence of two modes, which is shown in Figure 6.

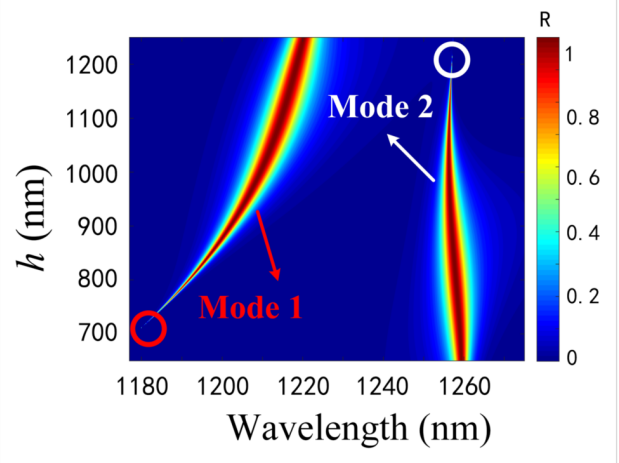

Figure 6: Reflection spectra mapping of the sensor with respect to wavelength and different h values at $\alpha = 0.15$.

The FWHM of mode 1 increases with h and the spectrum almost disappears at approx. $h = 700$ nm (red circles). When h changes from 700 to 1200 nm, the spectrum of mode 2 gradually becomes narrower until it disappears (white circles). This implies that mode 1 and mode 2 can induce the BIC through the control of cavity length. Accordingly, the change of the cavity length enables the modulation of the two modes of FWHM for the purpose of tuning the Q-factor. If a system contains two resonances whose positions and FWHM can be changed by a physical parameter, then there may exist a value within a certain parameter range that will make one of the resonances become a bound state [48]. A single grating layer in the proposed structure is 100% reflective, and the two identical gratings at the top and bottom of the structure are equivalent to two identical parallel reflectors (separated by a spacing of h) in the Fabry–Pérot cavity model, where the modes trapped between the two identical gratings are decoupled from the continuum [49,50]. In other words, the resonance in the single-layer grating is split into an extremely narrow and a wide resonance in the double-layer gratings for a given cavity length h. Without external driving sources, the two resonance amplitudes $A = (A_1, A_2)^T$ in the DLSG structure evolve in time as $i\partial A/\partial t = HA$ with Hamiltonian [51-53]:

$$H = \begin{bmatrix} \omega_0 & \kappa \\ \kappa & \omega_0 \end{bmatrix} - i\gamma_0 \begin{bmatrix} 1 & e^{i\psi} \\ e^{i\psi} & 1 \end{bmatrix}, \tag{3}$$

where κ is the near-field coupling between the two modes, ω_0 and γ_0 are the resonant frequency and radiation rate of the single grating resonance, respectively, and ψ is the propagation phase shift between the two resonators, satisfying the relation $\psi = kh$, where k is the transverse wave number. Then the two complex eigenfrequencies of H can be solved from Equation 3:

$$\omega_{\pm} = \omega_0 \pm \kappa - i\gamma_0 \left(1 \pm e^{i\psi}\right). \tag{4}$$

Tuning the cavity length h, when the round-trip phase shift is $2m\pi$ ($m = 0, 1, 2, \ldots$), the complex eigenfrequency of one mode in Equation 4 is $\omega_0 \pm \kappa - 2i\gamma$ with twice as much radiation loss as before. And the complex eigenfrequency of the other mode is $\omega_0 \pm \kappa$ with a pure real number, which indicates that it is an FP-BIC with an infinite Q-factor. The corresponding radiative Q-factors of the two modes at different h values when other structural parameters are constant are given in Figure 7. It can be found that mode 1 and mode 2 have infinite Q-factors at approx. 700 and 1200 nm, respectively. Consequently, both modes of the FP-BIC are governed by h. We can tune the linewidth and the corresponding Q-factor by changing the cavity length. The insets in Figure 7 show the optical field dis-

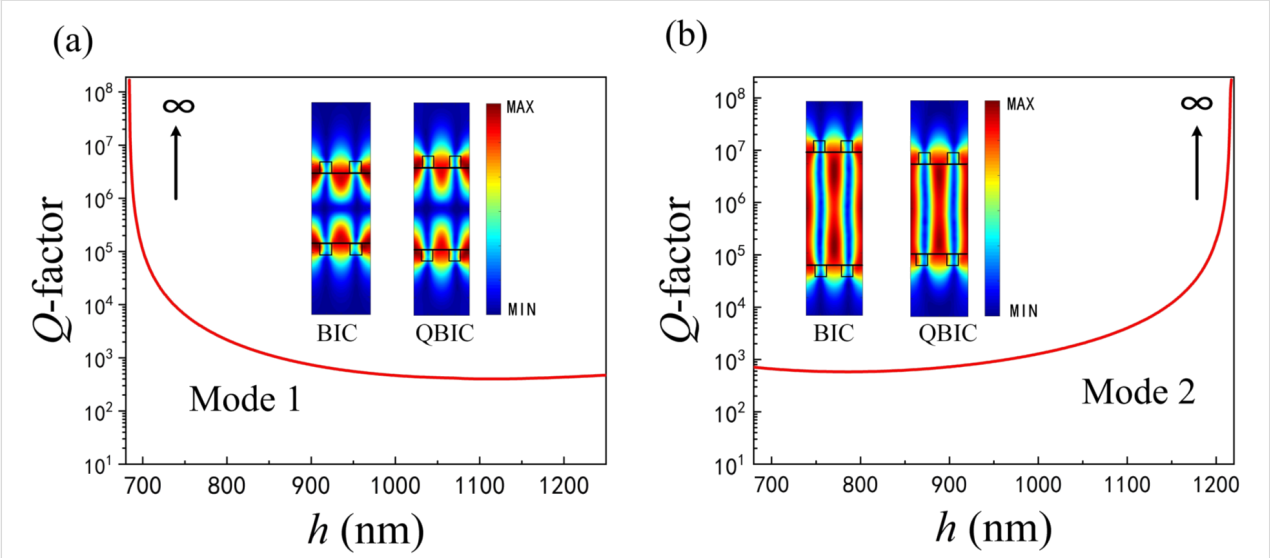

Figure 7: The *Q*-factor as a function of cavity length *h* of a) mode 1 and b) mode 2. The insets show the field distributions of the corresponding BIC and QBIC for the two modes.

tributions of the ideal BIC and the QBIC corresponding to the two modes. It is clear that the QBIC near the ideal BIC also possesses a strong localized optical field. Therefore, the FP-BIC can be perturbed by the variation on the cavity length.

To further understand the capability of different cavity lengths of the two modes to confine the localized optical field, the energy ratio of the cavity to the unit cell is analytically calculated from the perspective of the complex eigenfrequencies, which is defined as follows [54]:

$$\Gamma = \frac{\int_C |H_{\text{norm}}|^2 \, \mathrm{d}x\mathrm{d}z}{\int_U |H_{\text{norm}}|^2 \, \mathrm{d}x\mathrm{d}z}, \tag{5}$$

where C and U represent the integration domain for the cavity and the unit cell, respectively. H_{norm} represents the magnetic field intensity distributions of the complex eigenfrequencies.

It can be concluded from Equation 5 that the larger the confinement factor Γ the stronger the capacity of the cavity to confine the optical field. The calculation results are presented in Table 1. With respect to mode 1, the increase in cavity length leads to a decrease in the confinement capacity of the cavity to light (Γ decreases from 0.5381 to 0.3782). On the contrary, since most of the light in mode 2 is trapped inside the cavity, the increase of *h* improves the confinement capacity of the cavity (Γ increases from 0.6344 to 0.7513). Here, the flexible choice of cavity length enables to compress the effective volume for the resonant mode, which results in an enhanced confinement of the cavity to the optical field and an improved *Q*-factor.

Table 1: Confinement factors for two modes with different cavity lengths *h* at TM polarization.

Mode type	*h* (nm)	Γ
mode 1	700	0.5381
	900	0.4806
	1200	0.3782
mode 2	700	0.6344
	900	0.7157
	1200	0.7513

As discussed above, we can obtain a high-*Q*-factor resonance by reducing α. In addition, the high *Q*-factor can also be achieved by varying the cavity length *h*, which is necessary for refractive index sensing applications. When the QBIC is applied to refractive index sensing, it enables more sensitive detection owing to its high figure of merit (FOM), the physical mechanism of which uses resonant position variations to detect changes in the refractive index of the surrounding medium. In this section, we will investigate the sensing performance of the proposed structure through the variation of two key structural parameters (α and *h*). Besides the *Q*-factor, the sensitivity (*S*) and FOM are also two important parameters for a refractive index sensor, which are defined as the ratio of the resonant wavelength drift to the change in refractive index of the surrounding environment ($S = \Delta\lambda_{\text{res}}/\Delta n_{\text{c}}$) and the ratio of sensitivity to the FWHM (FOM = S/FWHM), respectively [55].

Taking the structural parameters previously mentioned as an example, the proposed structure can be fabricated as follows [56]. At first, the gratings of the bottom layer are fabricated using electron beam lithography (EBL) and reactive ion etching (RIE) on a SOI chip with a single crystalline silicon device layer and a buried oxide (BOX), where this SOI chip serves as the receiving substrate in an adhesive bonding process. Next, another bare SOI chip was bonded to the previously fabricated recipient substrate as a donor substrate, which is spin-coated using SU-8 on both the recipient and donor substrates. The silicon handle of the donor substrate is then removed by mechanical polishing and deep RIE, followed by removal of the BOX layer of the donor substrate by wet etching using hydrofluoric acid. Finally, the gratings are fabricated on the top layer with EBL and RIE, while the silicon handle and BOX layer on top are removed in the same way. It should be pointed out that the fabrication of the device requires removing the silicon handle and BOX layer twice (it makes the structure symmetrical), which makes the fabrication challenging to some extent. However, the simulation results show that the symmetrical structure of the device can improve the performance of the sensor.

The h value is fixed at h = 1000 nm and Figure 8a and Figure 8b demonstrate the S and FOM for the two modes with different α values. It is obvious that the FOM values of both modes decrease as α reduces. The FOM values for the two modes are 6770 and 9808 at α = 0.025, respectively. Furthermore, the highest sensitivity of the two modes is 413 and 265 nm/RIU, respectively. Here, we observe that although the FOM of mode 1 is lower than that of mode 2, which can be found from the normalized magnetic field distribution diagram that the light of mode 1 leaks more into vacuum (Figure 3b and Figure 3c), light is relatively less trapped inside the cavity, leading to more sensitivity to the refractive index change of the surrounding medium and thus higher sensitivity compared to

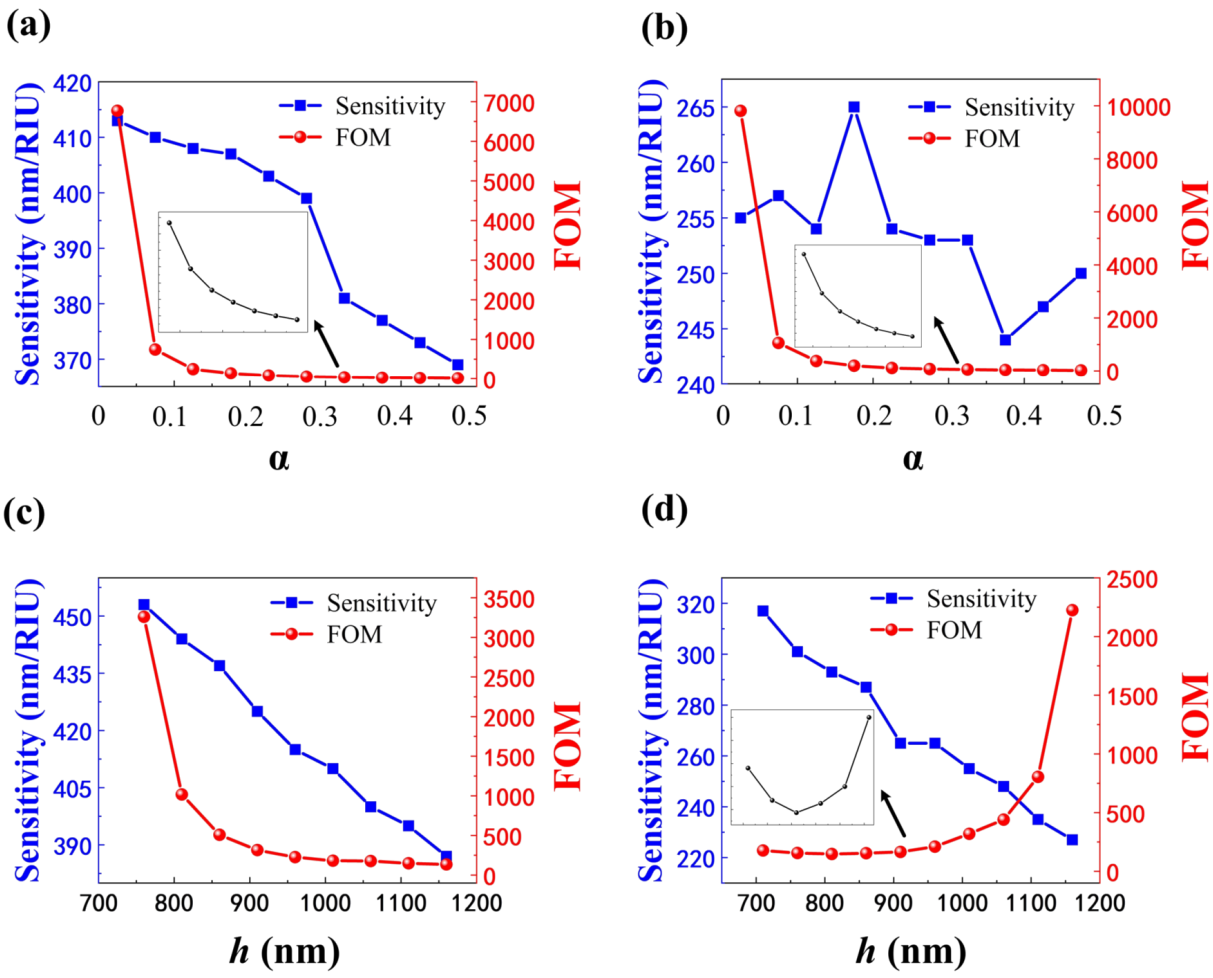

Figure 8: The S and FOM of a) mode 1 and b) mode 2 at different α values and h = 1000 nm. The S and FOM of c) mode 1 and d) mode 2 at different h values and α = 0.15.

mode 2. We then choose α = 0.15 to investigate the effect of the cavity length h on the sensing performance, as presented in Figure 8c and Figure 8d. It can be found that the sensitivity of both modes decreases with the increase in h. This is because an increase in h increases light trapping inside the cavity, decreasing light–matter interaction and sensitivity. On the contrary, the FOM values of the two modes do not have the same trend with increasing h. This is mainly attributed to the fact that the change in the cavity length of the Fabry–Pérot cavity has different magnetic field distributions for the two modes (the insets in Figure 7). The S is physically determined by the spatial overlap between the analyte and the evanescent waves, while the FOM is proportional to the Q-factor, which ultimately represents the ability of the sensor to track small changes in the refractive index of the environment [39,57].

We also found that the S of mode 1 at different α and h values follows the same trend as the FOM. The simulation results show that the values of α and h need to be decreased as much as possible to obtain high sensitivity and FOM of mode 1. The results were slightly different from those of mode 2, where one of the most sensitive regions exists, as shown in Figure 8b. This is may be due to the insignificant phase difference in the DLSG structure considered here [58]. Therefore, we can optimize the sensing performance by controlling the structural parameters, such as α and h, which are essentially the result of perturbing the artificial BIC and FP-BIC. The high sensitivity and FOM can be obtained thanks to the nearly symmetrical structure in vacuum which allows the optical field to be uniformly located in the grating and environment layers. This way, the confinement ability of the grating to the optical field is achieved while enhancing the relationship between light and matter.

Finally, the performance of the DLSG-based sensor is analyzed by choosing the structural parameters as an example: Λ = 800 nm, h = 1000 nm, w = 200 nm, α = 0.025 (the spacing between the two RDGs in a period is 205 nm). The Q-factors of mode 1 and mode 2 are 2.01×10^4 and 4.19×10^4, respectively. We summarized the S and FOM of QBIC when utilized for sensing as reported in other references in Table 2. One can find that although the S in this work is lower than that of some reported ones, it has a higher FOM and supports dual-band resonance.

Table 2: QBIC-based sensor performances. The description indicates the resonant mode in the reference.

Reference	Description	S (nm/RIU)	FOM
[3]	single-mode	657	9112
[16]	single-mode	221	4420
[25]	dual-band	526 312	8092 3387
[41]	dual-band	680 1143	183.8 317.5
this work	dual-band	413 255	6770 9808

Figure 9a shows the simulated reflection spectra of the proposed sensor when placed in a gas medium with different refractive indexes from 1.01 to 1.09 under a TM-polarized incident plane wave. The sharp reflection peaks of both mode 1 and mode 2 show a significant red shift, despite a small fluctuation (Δn_c = 0.02). By extracting the positions of the reflection peaks of the two modes from Figure 9a and plotting them as a func-

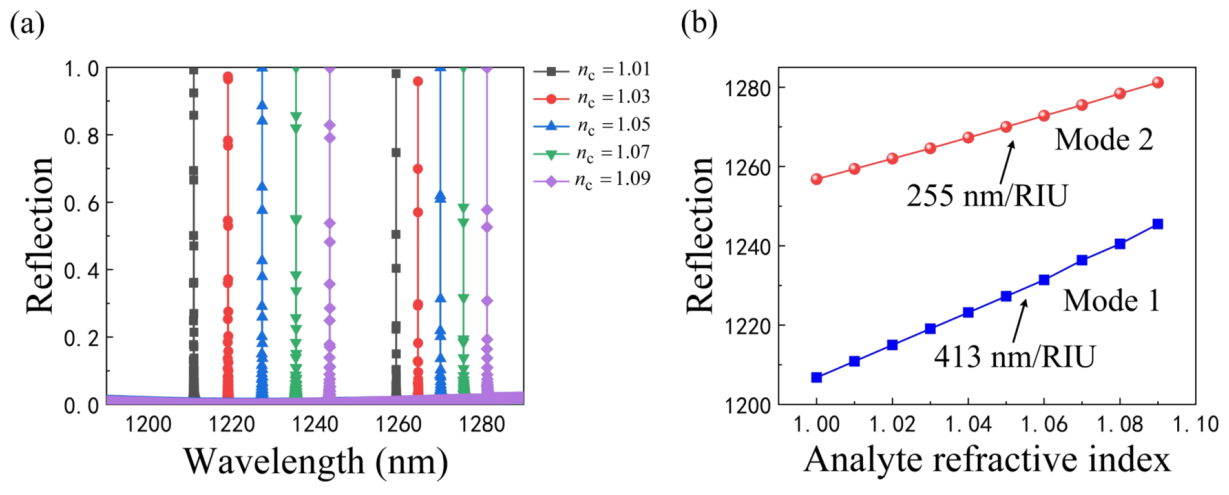

Figure 9: a) Reflection spectra of the sensor at different refractive indices of the gas medium. b) Positions of the two-mode reflection resonance peaks.

tion of the refractive index of the analyte, the fitted curves exhibit a good linearity as seen in Figure 9b.

Conclusion

In summary, a DLSG-based structure is proposed, which can support dual-band high-Q resonances governed by BIC. Particularly, the evolution of single and double resonances can be controlled by changing the spacing of the RDGs. The artificial BIC and FP-BIC can be induced by optimizing two key structural parameters (the spacing of two gratings in a unit cell and cavity length). Specifically, we calculated the reflection spectra using RCWA for different grating spacings and cavity lengths, respectively, with the artificial BIC and FP-BIC exhibiting vanishing linewidths in the spectra. The complex eigenfrequencies of the BIC induced by different parameters were then analyzed using FEM and the corresponding radiative Q-factors were calculated. The two BICs were perturbed to convert an infinite Q-factor (ideal BIC) into a finite but high Q-factor (QBIC), which exhibited a dual-band high-Q resonance when used for optical sensing, allowing for more sensitive detection. The designed resonator has potential prospects for applications such as multi-wavelength sensing and nonlinear optics, which are important for practical nano-optics utilization.

Funding

National Natural Science Foundation of China (61905060, 21976049); National Natural Science Foundation of Hebei Province (F2019402063, F2019402240, B2021402006); Scientific Research Project of the Department of Education of Hebei Province (ZD2021019); Open Project of Shandong Key Laboratory of Optics and Photonic Device (K202104); and Graduate Student Innovation Ability Funding Project of the Department of Education of Hebei Province (CXZZSS2022026).

References

1. Liu, H.; Sun, Z. *Opt. Express* **2021,** *29,* 13590–13599. doi:10.1364/oe.424296
2. Koshelev, K.; Kruk, S.; Melik-Gaykazyan, E.; Choi, J.-H.; Bogdanov, A.; Park, H.-G.; Kivshar, Y. *Science* **2020,** *367,* 288–292. doi:10.1126/science.aaz3985
3. Mesli, S.; Yala, H.; Hamidi, M.; BelKhir, A.; Baida, F. I. *Opt. Express* **2021,** *29,* 21199–21211. doi:10.1364/oe.424930
4. Jiang, B.; Zhu, S.; Ren, L.; Shi, L.; Zhang, X. *Adv. Photonics* **2022,** *4,* 046003. doi:10.1117/1.ap.4.4.046003
5. Dayal, G.; Chin, X. Y.; Soci, C.; Singh, R. *Adv. Opt. Mater.* **2016,** *4,* 1295–1301. doi:10.1002/adom.201600356
6. Wang, B.; Yu, P.; Wang, W.; Zhang, X.; Kuo, H.-C.; Xu, H.; Wang, Z. M. *Adv. Opt. Mater.* **2021,** *9,* 2001520. doi:10.1002/adom.202001520
7. Jahani, S.; Jacob, Z. *Nat. Nanotechnol.* **2016,** *11,* 23–36. doi:10.1038/nnano.2015.304
8. Tonkaev, P.; Kivshar, Y. *JETP Lett.* **2020,** *112,* 615–622. doi:10.1134/s0021364020220038
9. Chang-Hasnain, C. J.; Yang, W. *Adv. Opt. Photonics* **2012,** *4,* 379–440. doi:10.1364/aop.4.000379
10. Zhou, Y.; Moewe, M.; Kern, J.; Huang, M. C. Y.; Chang-Hasnain, C. J. *Opt. Express* **2008,** *16,* 17282–17287. doi:10.1364/oe.16.017282
11. Chang-Hasnain, C. J. *Semicond. Sci. Technol.* **2011,** *26,* 014043. doi:10.1088/0268-1242/26/1/014043
12. Finco, G.; Bideskan, M. Z.; Vertchenko, L.; Beliaev, L. Y.; Malureanu, R.; Lindvold, L. R.; Takayama, O.; Andersen, P. E.; Lavrinenko, A. V. *Nanophotonics* **2021,** *10,* 4289–4296. doi:10.1515/nanoph-2021-0347
13. Karagodsky, V.; Sedgwick, F. G.; Chang-Hasnain, C. J. *Opt. Express* **2010,** *18,* 16973–16988. doi:10.1364/oe.18.016973
14. Karagodsky, V.; Chang-Hasnain, C. J. *Opt. Express* **2012,** *20,* 10888–10895. doi:10.1364/oe.20.010888
15. Joseph, S.; Sarkar, S.; Khan, S.; Joseph, J. *Adv. Opt. Mater.* **2021,** *9,* 2001895. doi:10.1002/adom.202001895
16. Zhang, H.; Wang, T.; Tian, J.; Sun, J.; Li, S.; De Leon, I.; Zaccaria, R. P.; Peng, L.; Gao, F.; Lin, X.; Chen, H.; Wang, G. *Nanophotonics* **2022,** *11,* 297–304. doi:10.1515/nanoph-2021-0368
17. Wang, Y.; Song, J.; Dong, L.; Lu, M. *J. Opt. Soc. Am. B* **2016,** *33,* 2472–2479. doi:10.1364/josab.33.002472
18. Lee, S.-G.; Kim, S.-H.; Kee, C.-S. *Nanophotonics* **2020,** *9,* 4373–4380. doi:10.1515/nanoph-2020-0346
19. Wang, M.; Li, B.; Wang, W. *J. Opt. (Bristol, U. K.)* **2020,** *22,* 125102. doi:10.1088/2040-8986/abc1fb
20. Neumann, J. V.; Wigner, E. *Phys. Z.* **1929,** *30,* 465–467.
21. Hsu, C. W.; Zhen, B.; Stone, A. D.; Joannopoulos, J. D.; Soljačić, M. *Nat. Rev. Mater.* **2016,** *1,* 16048. doi:10.1038/natrevmats.2016.48
22. Zheng, Z.; Zhu, Y.; Duan, J.; Qin, M.; Wu, F.; Xiao, S. *Opt. Express* **2021,** *29,* 29541–29549. doi:10.1364/oe.438180
23. Qin, M.; Xiao, S.; Liu, W.; Ouyang, M.; Yu, T.; Wang, T.; Liao, Q. *Opt. Express* **2021,** *29,* 18026–18036. doi:10.1364/oe.427141
24. Huang, L.; Chiang, Y. K.; Huang, S.; Shen, C.; Deng, F.; Cheng, Y.; Jia, B.; Li, Y.; Powell, D. A.; Miroshnichenko, A. E. *Nat. Commun.* **2021,** *12,* 4819. doi:10.1038/s41467-021-25130-4
25. Cai, Y.; Huang, Y.; Zhu, K.; Wu, H. *Opt. Lett.* **2021,** *46,* 4049–4052. doi:10.1364/ol.432117
26. Koshelev, K.; Lepeshov, S.; Liu, M.; Bogdanov, A.; Kivshar, Y. *Phys. Rev. Lett.* **2018,** *121,* 193903. doi:10.1103/physrevlett.121.193903
27. Xiao, S.; Qin, M.; Duan, J.; Wu, F.; Liu, T. *Phys. Rev. B* **2022,** *105,* 195440. doi:10.1103/physrevb.105.195440
28. Overvig, A.; Alù, A. *Adv. Photonics* **2021,** *3,* 026002. doi:10.1117/1.ap.3.2.026002
29. Bulgakov, E. N.; Maksimov, D. N.; Semina, P. N.; Skorobogatov, S. A. *J. Opt. Soc. Am. B* **2018,** *35,* 1218–1222. doi:10.1364/josab.35.001218
30. Foley, J. M.; Young, S. M.; Phillips, J. D. *Phys. Rev. B* **2014,** *89,* 165111. doi:10.1103/physrevb.89.165111
31. Gao, X.; Hsu, C. W.; Zhen, B.; Lin, X.; Joannopoulos, J. D.; Soljačić, M.; Chen, H. *Sci. Rep.* **2016,** *6,* 31908. doi:10.1038/srep31908
32. Ahumada, M.; Orellana, P. A.; Retamal, J. C. *Phys. Rev. A* **2018,** *98,* 023827. doi:10.1103/physreva.98.023827
33. Doskolovich, L. L.; Bezus, E. A.; Bykov, D. A. *Photonics Res.* **2019,** *7,* 1314–1322. doi:10.1364/prj.7.001314
34. Huang, L.; Xu, L.; Rahmani, M.; Neshev, D.; Miroshnichenko, A. E. *Adv. Photonics* **2021,** *3,* 016004. doi:10.1117/1.ap.3.1.016004
35. Al-Ani, I. A. M.; As'Ham, K.; Huang, L.; Miroshnichenko, A. E.; Lei, W.; Hattori, H. T. *Adv. Opt. Mater.* **2022,** *10,* 2101120. doi:10.1002/adom.202101120

36. Wang, X.; Duan, J.; Chen, W.; Zhou, C.; Liu, T.; Xiao, S. *Phys. Rev. B* **2020,** *102,* 155432. doi:10.1103/physrevb.102.155432
37. Masoudian Saadabad, R.; Huang, L.; Miroshnichenko, A. E. *Phys. Rev. B* **2021,** *104,* 235405. doi:10.1103/physrevb.104.235405
38. Lin, J.; Farajollahi, S.; Fang, Z.; Yao, N.; Gao, R.; Guan, J.; Deng, L.; Lu, T.; Wang, M.; Zhang, H.; Fang, W.; Qiao, L.; Cheng, Y. *Adv. Photonics* **2022,** *4,* 036001. doi:10.1117/1.ap.4.3.036001
39. Maksimov, D. N.; Gerasimov, V. S.; Romano, S.; Polyutov, S. P. *Opt. Express* **2020,** *28,* 38907–38916. doi:10.1364/oe.411749
40. Moharam, M. G.; Grann, E. B.; Pommet, D. A.; Gaylord, T. K. *J. Opt. Soc. Am. A* **1995,** *12,* 1068–1076. doi:10.1364/josaa.12.001068
41. Moharam, M. G.; Pommet, D. A.; Grann, E. B.; Gaylord, T. K. *J. Opt. Soc. Am. A* **1995,** *12,* 1077–1086. doi:10.1364/josaa.12.001077
42. Huang, L.; Yu, Y.; Cao, L. *Nano Lett.* **2013,** *13,* 3559–3565. doi:10.1021/nl401150j
43. Liu, C.; Bai, Y.; Zhou, J.; Chen, J.; Qiao, L. *Opt. Express* **2021,** *29,* 42978–42988. doi:10.1364/oe.446937
44. Yu, Y.; Cao, L. *Opt. Express* **2012,** *20,* 13847–13856. doi:10.1364/oe.20.013847
45. Overvig, A. C.; Shrestha, S.; Yu, N. *Nanophotonics* **2018,** *7,* 1157–1168. doi:10.1515/nanoph-2017-0127
46. Al-Ani, I. A. M.; As'Ham, K.; Huang, L.; Miroshnichenko, A. E.; Hattori, H. T. *Laser Photonics Rev.* **2021,** *15,* 2100240. doi:10.1002/lpor.202100240
47. Azzam, S. I.; Shalaev, V. M.; Boltasseva, A.; Kildishev, A. V. *Phys. Rev. Lett.* **2018,** *121,* 253901. doi:10.1103/physrevlett.121.253901
48. Ndangali, R. F.; Shabanov, S. V. *J. Math. Phys.* **2010,** *51,* 102901. doi:10.1063/1.3486358
49. Marinica, D. C.; Borisov, A. G.; Shabanov, S. V. *Phys. Rev. Lett.* **2008,** *100,* 183902. doi:10.1103/physrevlett.100.183902
50. Wu, F.; Fan, C.; Zhu, K.; Wu, J.; Qi, X.; Sun, Y.; Xiao, S.; Jiang, H.; Chen, H. *Phys. Rev. B* **2022,** *105,* 245417. doi:10.1103/physrevb.105.245417
51. Fan, S.; Villeneuve, P. R.; Joannopoulos, J. D.; Khan, M. J.; Manolatou, C.; Haus, H. A. *Phys. Rev. B* **1999,** *59,* 15882–15892. doi:10.1103/physrevb.59.15882
52. Manolatou, C.; Khan, M. J.; Fan, S.; Villeneuve, P. R.; Haus, H. A.; Joannopoulos, J. D. *IEEE J. Quantum Electron.* **1999,** *35,* 1322–1331. doi:10.1109/3.784592
53. Wang, Z.; Fan, S. *Phys. Rev. E* **2003,** *68,* 066616. doi:10.1103/physreve.68.066616
54. Hu, J.-H.; Huang, Y.-Q.; Ren, X.-M.; Duan, X.-F.; Li, Y.-H.; Wang, Q.; Zhang, X.; Wang, J. *Chin. Phys. Lett.* **2014,** *31,* 064205. doi:10.1088/0256-307x/31/6/064205
55. Xu, Y.; Bai, P.; Zhou, X.; Akimov, Y.; Png, C. E.; Ang, L.-K.; Knoll, W.; Wu, L. *Adv. Opt. Mater.* **2019,** *7,* 1801433. doi:10.1002/adom.201801433
56. Zhang, Y.; Kwong, D.; Xu, X.; Hosseini, A.; Yang, S. Y.; Rogers, J. A.; Chen, R. T. *Appl. Phys. Lett.* **2013,** *102,* 211109. doi:10.1063/1.4808208
57. Bao, Y.; Liu, X.; Hu, J.; Zou, J.; Han, H.; Wang, C. *Opt. Express* **2021,** *29,* 29458–29465. doi:10.1364/oe.435653
58. Lin, S.-F.; Wang, C.-M.; Ding, T.-J.; Tsai, Y.-L.; Yang, T.-H.; Chen, W.-Y.; Chang, J.-Y. *Opt. Express* **2012,** *20,* 14584–14595. doi:10.1364/oe.20.014584

License and Terms

BEILSTEIN JOURNAL OF NANOTECHNOLOGY

Quasi-guided modes resulting from the band folding effect in a photonic crystal slab for enhanced interactions of matters with free-space radiations

Kaili Sun[1], Yangjian Cai[1], Uriel Levy[2] and Zhanghua Han[*1]

Full Research Paper

Open Access

Address:
[1]Shandong Provincial Key Laboratory of Optics and Photonic Devices, Center of Light Manipulation and Applications, School of Physics and Electronics, Shandong Normal University, Jinan 250358, China and [2]Department of Applied Physics, The Hebrew University of Jerusalem, Jerusalem, Israel

Email:
Zhanghua Han[*] - zhan@sdnu.edu.cn

* Corresponding author

Keywords:
guided modes; light–matter interactions; photonic crystal slab

Beilstein J. Nanotechnol. **2023,** *14,* 322–328.
https://doi.org/10.3762/bjnano.14.27

Received: 13 October 2022
Accepted: 14 February 2023
Published: 06 March 2023

This article is part of the thematic issue "Physics and optical applications of all-dieletric nanostructures".

Associate Editor: M. Nolan

Abstract

We elucidate that guided modes supported by a regular photonic crystal slab structure composed of a square lattice of air holes in a silicon slab will transition into quasi-guided (leaky) modes when the radius of every second column of air holes is changed slightly. This intentional geometric perturbation will lead to a doubling of the period in one direction and the corresponding shrinkage of the first Brillouin zone. Because of the translational symmetry in the k-space, leaky waves inheriting the spatial dispersion of the original guided modes, which do not interact with external radiation, will appear with the dispersion curves above the light cone. Our results show that ultrahigh Q-factor resonances with large operating bandwidth can be achieved. Interestingly, the perturbation in only one direction of the photonic lattice will lead to an in-plane wave number-dependent resonance characteristic in both directions. Our numerical results demonstrate a local enhancement of the electric field magnitude by the order of 10^2, which is even more significant than those in most plasmonic structures. These quasi-guided modes with superior properties will provide a new platform for efficient light–matter interactions.

Introduction

Photonic resonances with the possibility of free-space excitation (i.e., leaky modes) and large local electromagnetic field enhancement are central for the manipulation of light–matter interactions. Optical resonators of various forms have been exploited for this purpose. What follows are a few representative examples investigated in the last several decades: Photonic crystal cavities are realized when small disorders or defects are introduced into large-scale periodic structures [1]. Extremely high Q-factors can be achieved thanks to the bandgap associated with the periodic structure, which prevents the leakage of radiation into the surrounding environment. Whispering gallery modes supported by dielectric spheres or suspended disks made of high-index materials are another example of resonances to provide ultrahigh Q-factors [2]. However, above structures are

still bulky. For example, the photonic crystal cavities need the surrounding periods to provide the bandgap, which is not favorable for nanoscale applications. Plasmonic nanoantennas [3], although with relatively low Q-factors resulting from material dissipation, still provide a large level of field enhancement due to the deep-subwavelength level of mode confinement. As new alternatives to plasmonic nanostructures, all-dielectric nanostructures supporting Mie resonances [4] and quasi-bound state in the continuum (QBIC) modes [5] have attracted significant attention in nanophotonic research, with the latter proposed to address the problem of radiation losses associated with the former. A large variety of novel applications benefiting from such optical resonances have been demonstrated in all aspects of light–matter interactions, ranging from optical generation [6], propagation [7], nonlinear processes [8] to signal detection [9] and collection, to name a few. Although QBIC resonances in all-dielectric nanostructures have become a popular and mainstream approach to enhance light–matter interactions, as derivatives of ideal BIC resonances, which are associated with isolated or discrete points of high symmetry in the ω–k space [10], they still suffer from very limited operating bandwidth. As a result, the QBIC resonances are not suitable for many important optical applications where multiple or spectrally tunable inputs are required simultaneously. Consequently, new mechanisms are still explored to realize novel photonic components with additional advantages besides a high Q-factor. These are, for example, phase gradient metasurfaces and spatial beam splitters [11], metasurfaces that produce narrow-band spatially tailored wave fronts [12], and zigzag arrays of dielectric disks with ultranarrow bandwidth resonances over a large spectral band [13]. Some new attempts to engineer the radiation environment to achieve so-called lines of BICs have emerged quite recently [14]. But the idea and reported results require very complicated geometries [15], which are challenging to fabricate.

Results and Discussion

In this work, we propose a fundamentally different approach to realize optical leaky resonances that can combine all the advantages of the above resonances, that is, ultrahigh Q-factors, huge local electric enhancement, and intermediate mode volume, while providing a large operation bandwidth. Unlike QBIC resonances, we start from guided modes (GMs) whose optical fields are well confined within the geometry and have no access to external radiation. The GMs have typical continuous and one-dimensional dispersion curves below the light line over a large bandwidth. This leaky resonance is generated through band folding, which occurs when a perturbation is introduced into a regular periodic structure to have its period increased and the first Brillouin zone (FBZ) shrunk. Because of the translational symmetry in the k space, the GMs with infinite Q-factors supported by the original lattice will appear as new leaky resonances with the dispersion curves above the light cone in the new structure. These resonances, termed quasi-guided modes (QGMs), will inherit the spatial dispersion of the original GMs, with Q-factors significantly dependent on the level of perturbation. As a result, they feature ultrahigh Q-factors while the resonance can be tuned by the lateral wave vector. The QGMs outperform QBIC resonances, which can only operate within a narrow bandwidth, even at a wave number largely different from that of the original BIC resonance.

We should note that a similar band-folding effect has been proposed in the literature to improve the angular tolerance in the reflection of resonant grating filters with doubly periodic structures [16,17]. Other structures, such as diatomic [18] or dimerized [19,20] gratings, have been also investigated in recent years, but mainly with emphasis on the far-field spectrum, using one-dimensional (1D) grating structures. In addition, band folding was also employed to realize terahertz radiation from difference frequency generation (DFG) by using 1D leaky modes of binary waveguide gratings [21] and to manipulate the radiation coupling in the vertical directions in some photonic crystal cavities [22,23]. A similar structure of a ZnO photonic crystal slab (PCS) with doubled periods in both directions has been proposed to realize low-threshold polariton lasers [24]. However, we show in this work that, even when the period increase and the accompanied FBZ shrinking occurs only along one direction of the two-dimensional periodicity, the resonance still depends on the in-plane wave vector along both directions. This suggests the possibility of resonance tuning over an extended bandwidth by using the incident angle along two different directions as the tuning mechanism. More importantly, we further illustrate that these QGM resonances have a significantly enhanced local electric field, which is even larger than that of most plasmonic nanoantennas, suggesting the great potential of these QGMs for enhanced light–matter interactions.

We use GMs supported by a regular PCS structure composed of a square lattice of air holes perforating a thin silicon (refractive index: 3.45) film on a silica (refractive index 1.45) substrate as an example to demonstrate that these modes can be switched to QGMs with ultrahigh Q-factors over a large operating bandwidth, as shown in Figure 1. When all air holes have the same radius, the whole structure represents a two-dimensional PCS structure with a square primitive unit cell. With the period $P_x = P_y = a$ along both x and y directions, this structure is known to support a set of well-confined GMs with no external radiation [25], which lay out the foundation for integrated photonic elements in the PCS. The lines of empty circles in Figure 2 present the dispersion curve for the GMs along ΓX and XM directions in the FBZ supported by the square lattice with

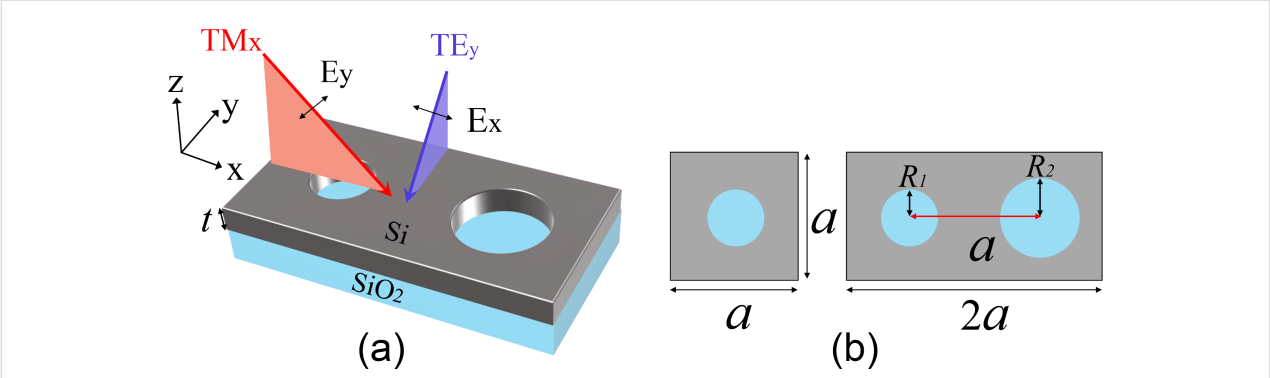

Figure 1: (a) Schematic of the photonic crystal slab structure of air holes in a silicon layer. (b) Top view of the unit cells for two cases. Left: the square lattice of the original structure, right: the distorted rectangular lattice with a period of $2a \times a$.

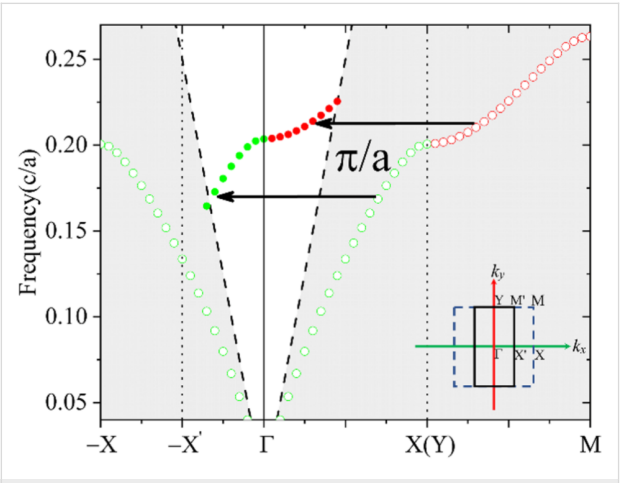

Figure 2: Dispersion curves of the GMs (hollow circles) supported by the PCS of air holes in SOI and the QGMs (solid circles) supported the distorted lattice where the radius of every second column of air holes is changed to R_2. The inset shows the FBZ for the two cases. The green and red colors denote the dispersion along the k_x and k_y direction, respectively.

a = 400 nm, R_1 = 100 nm, and t = 220 nm. The results were obtained by using the eigenfrequency analysis and lateral Fouquet boundary conditions implemented in the commercial finite-element method software Comsol Multiphysics. All numerical models are built with 3D structures. The size of the tetrahedral mesh was tested to ensure the numerical convergence of the calculated results. It is seen that the dispersion curve of the GMs $f_0(k_x, k_y)$ is well below that of the light cone (this region is displayed with a dark background). When the radius of the air holes in every second column is increased by a quantity of δ to R_2 = 120 nm, the period along the x direction will be doubled to be $P_{2x} = 2a$ while it remains unchanged in the y direction. As a result, the FBZ shrinks in the x direction and its shape changes from a square to a rectangle, as shown in the inset of Figure 2. With the period in the k_x direction halved to $2\pi/P_{2x} = \pi/a$, one has the dispersion equation $f(k_x, k_y)$ in the distorted lattice as:

$$f\left(k_x, k_y\right) = f\left(k_x - \pi/a, k_y\right). \tag{1}$$

When the perturbation introduced into the lattice is weak, the distorted lattice remains approximately the same as the undistorted, and so are the supported resonance frequencies. Then we have

$$f\left(k_x - \pi/a, k_y\right) \approx f_0\left(k_x - \pi/a, k_y\right). \tag{2}$$

Combining Equation 1 and Equation 2, we obtain the following equation:

$$f\left(k_x, k_y\right) \approx f_0\left(k_x - \pi/a, k_y\right), \tag{3}$$

which suggests that dispersion curves with similar profiles as the GMs in the PCS around the X point will appear around the Γ point in the distorted lattice. In other words, the dispersion curve of GMs along ΓX and XM directions in the original square unit cell will be translated to the −XΓ and ΓY directions in the new lattice, respectively. Since the wave numbers close to Γ point are relatively small, the majority of the translated dispersion curves will be located above the light cone in the distorted lattice, suggesting leaky resonances.

The curve composed of solid circles in Figure 2 presents the calculated dispersion for the QGMs of the rectangular primitive cell shown on the right side of Figure 1b, where R_2 is set to be 120 nm. The eigenfrequencies are found around the same band as the GMs. The results are entirely consistent with the above predictions from Equation 3. It is quite clear that the dispersion curves of the QGMs around the Γ point have roughly the same profiles as the original GMs around the X point, both in the k_x and k_y directions. As a result, although the period remains un-

changed along the y direction (P_y is still a), the dispersion along k_y is also located above the light cone and resembles the profile of $f_0(k_x, k_y)$ along the XM direction. A weaker spatial dispersion of the QGMs is present in the k_y direction compared to the k_x direction, which is the same as for the GMs.

The total Q-factor (Q_{total}) of a resonance observed in the far-field spectrum is determined by the Q-factors of radiation (Q_{rad}) and absorption (Q_{abs}) [26]:

$$\frac{1}{Q_{total}} = \frac{1}{Q_{rad}} + \frac{1}{Q_{abs}}. \quad (4)$$

Because the absorption loss of materials is not considered here, that is, Q_{abs} is infinite, Q_{total} is determined solely by Q_{rad} of the structure. Its value or the radiation loss can be obtained from the real and imaginary parts of its complex eigenfrequency from the numerical calculations. The calculated Q-factors of these QGMs are presented in Figure 3a. The value is infinite at the Γ point, which arises from an ideal BIC resonance of the symmetry-protected type. This is because the new periodic structure, even with the radius of the air holes in every second column changed, still exhibits a mirror symmetry across the central xz and yz planes of all air holes. Further away from the Γ point, the Q-factor decreases for larger wave numbers but maintains overall large values (above 10^3) for all resonances. To have a moderate level of Q-factors (i.e., measurable in practical experiments) for the transmission spectra presented in the subsequent part, we used intentionally a stronger perturbation with a δ value of 20 nm. We note that the overall Q-factors will be significantly increased if a weaker perturbation is introduced. The dispersion of the GMs is located well below the light line, preventing any outward radiation due to total internal reflection. In other words, the Q-factors of all GMs are infinite since we ignore the material absorption in the lossless dielectrics. When the period-doubling perturbation is applied and the new QGMs are formed because of the folding of the FBZ, the coupling efficiency between free-space radiation and the QGMs is still very low, leading to the occurrence of high Q-factor resonances. Intuitively, the Q-factors highly depend on the level of perturbation. In addition, since the spatial dispersion of the original GMs is retained in the QGMs, one can have ultrahigh Q-factors over a large bandwidth, and the resonance can be tuned by changing the wave vector or, equivalently, the incident angle of external excitations. This is in huge contrast to QBIC resonances, whose frequency is limited within a narrow band close to the frequency of the original BIC resonance from which the QBIC resonances are derived. Similar to QBIC resonances, the Q-factors exhibit a strong dependence on the level of perturbation and increase significantly as the perturbation decreases. The value of the Q-factor will approach infinity as δ approaches zero, where the lattice returns to the regular square lattice of air holes (P_x decreases from $2a$ to a) and the QGMs switch back to GMs. Interestingly, the trend of Q approaching infinity when the perturbation vanishes is true for any resonance along the QGM dispersion curve. Figure 3b presents the calculated Q-factors at two randomly selected points along k_x and k_y for the QGMs and the dependence of Q on the extent of the perturbation is clearly seen. We should note that this behavior is another feature of the QGMs significantly different from those of QBIC resonances. The operating bandwidth of QBIC resonances significantly depends on the level of perturbation

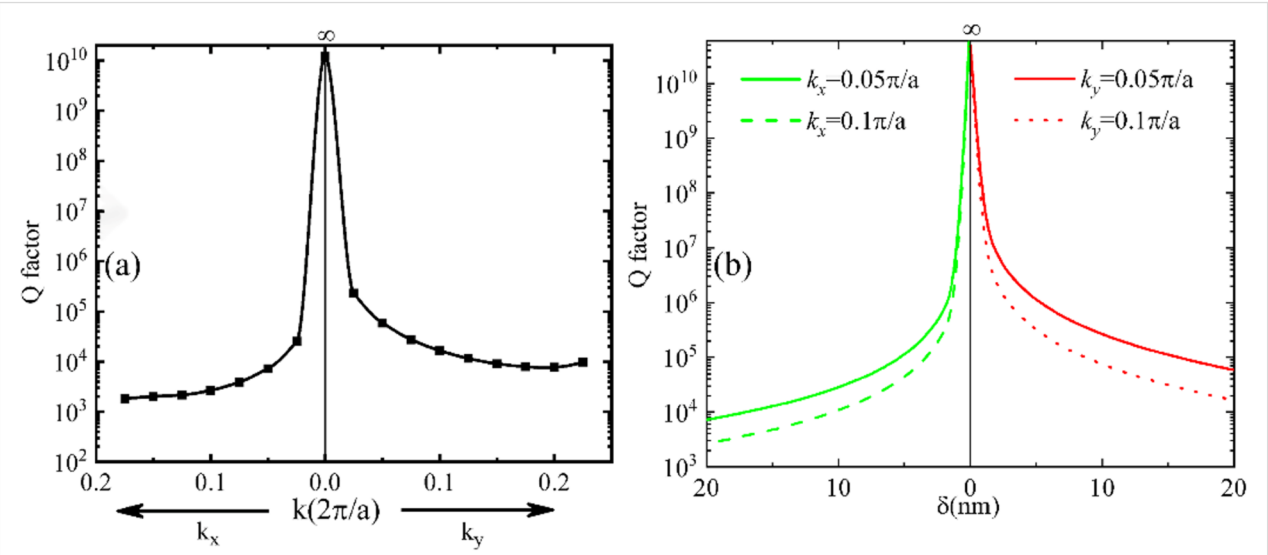

Figure 3: (a) Q-factors along the dispersion curves of QGMs in Figure 2. (b) Q-factor as a function of the level of perturbation at two points along two directions.

introduced into the geometry to transform the BIC resonance into QBICs. The bandwidth is smaller if the perturbation is weaker, which is the case when one aspires for a high Q-factor. As the geometrical perturbation decreases, the dispersion curve of the QBIC resonances will shrink to a single point in the ω–k space, which represents the BIC resonance. For the QGMs, the operating bandwidth is not affected at all by the level of perturbation. Instead, it is determined by the spatial dispersion of the GMs in the PCS. Thus, the ultrahigh Q-factors can be maintained over the same broad bandwidth, regardless of the level of perturbation. All these properties of the QGMs make it possible to realize superior leaky modes with ultrahigh Q-factors and a value of Q completely controlled by the extent of perturbation over the same bandwidth. Compared to the 1D periodic structure, the operation bandwidth of a 2D structure extends by exploiting the changes of the wave number in a direction different from the direction of lattice change.

To have a straightforward demonstration of tuning the resonance via the incident angle, we present in Figure 4 the calculated transmission spectra for three different incident angles of 3°, 6°, and 9° along both x and y directions. We note that when the period-doubling perturbation is absent ($R_1 = R_2$), the structure returns to a regular PCS, which supports the well-known guided mode resonances in a frequency-doubled spectrum range [27]. The guided mode resonances have relatively broad bandwidths compared to QGM resonances, and their properties have been well documented in the literature. In the spectrum of our interest, the regular PCS only supports broadband Fabry–Pérot resonances, and the transmission exhibits no sharp features, because only well-confined GMs are supported. However, when the perturbation is applied, QGMs will be formed and new sharp resonances will be superimposed onto the transmission spectrum. The setup of the incident beams with respect to the structure can be found in Figure 1a, where the electric field of

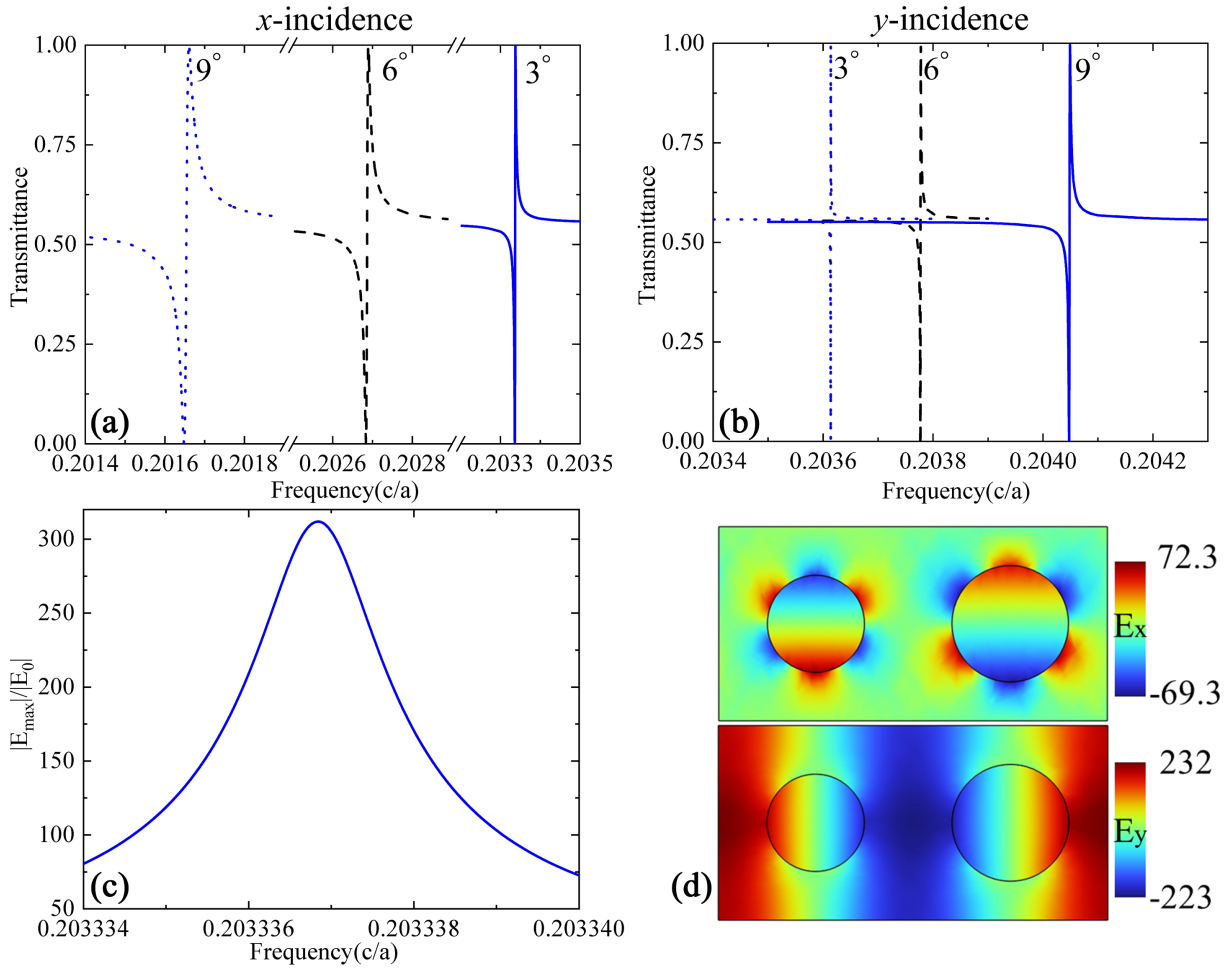

Figure 4: Transmission spectra at different incident angles with the incidence in (a) the xz plane and (b) the yz plane. (c) The maximum electric field magnitude normalized to that of the incident wave across the central plane of the Si layer. (d) Typical distributions of E_x and E_y along the central plane of the silicon layer.

E_y is used to excite the QGMs. A redshift of the resonance for a larger incident angle is observed for TM_x along the x direction, while the trend is opposite for TE_y along the y direction. Judging from the bandwidth of the resonance, one can see that the Q-factor decreases slightly at a larger incident angles for the incidence along the x direction, while it increases for the incidence along the y direction. All these results are consistent with the dispersion curves in Figure 2 and the evolution of Q-factors as a function of the wave number in Figure 3a. Figure 4d presents typical distributions of the real part of both E_x and E_y at the resonance frequency across the central plane of the silicon layer under an incidence angle of 3° along the x direction. It is seen that E_x exhibits a symmetric profile while E_y has the opposite distribution within individual holes along the x direction, where the lattice distortion happens. The distribution of the electric field mainly within the air holes is due to symmetry reasons. For our structure, in which the radius of every second column of holes is changed, mirror symmetry is still retained across the center of each hole the along x direction, which ensures an effective coupling between the modes with x-polarized plane waves. This kind of field distribution in Figure 4d is useful for sensing applications. For other applications where one would like to have the main field within the dielectrics, another kind of perturbation by moving the position of every second column of holes could be used instead. The distributions in Figure 4d confirm that the QGMs around the Γ point inherit the same mode profiles of the original guided mode at the boundary of the FBZ (the X point), where the field distributions are anti-symmetric in the ΓX direction. In addition, it is known that the maximum local field enhancement is determined by the resonance Q-factor and the mode volume [26]. For periodic structures, a discussion of the mode volume calculation can be found in [28]. The intermediate mode confinement within the photonic crystal slab structure and the ultrahigh Q-factors of the QGMs make it possible to obtain a huge electric field enhancement. Figure 4c presents the maximum local electric field magnitude normalized to that of the incident plane wave. It can be seen that an enhancement factor of 312 can be achieved for an incident angle of 3° along the x axis. This number decreases to 156 and 107 for incident angles of 6° and 9° along the x axis, respectively, and increases to 950, 477, and 319, respectively, for incident angles of 3°, 6°, and 9° along the y axis. The trend of the level of enhancement is consistent with that of the Q-factor as a function of the incident angle shown in Figure 3. We should note here that all these values of local electric field enhancement are generally higher than those that can be achieved with a regular guided resonance in a similar PCS structure supporting Fano-type resonances [27] or with most plasmonic nanoantennas [3]. This is because of the high value of Q and the relatively low mode volume of these QGMs [26]. We further note that the maximum electric field enhancement is located within the air holes (from the magnitude of the electric field, which is not shown in Figure 4), where the mirror symmetry results in a large spatial overlap of the mode with the electric field of the incident plane wave [19,20]. If another kind of period-doubling perturbation is used, for example, by shifting the position of every second column of air holes, the mirror symmetry will be maintained within the dielectric material between the air holes, where the local electric field enhancement will occur.

Conclusion

We have presented in this work the superior properties of the QGMs that occur when a perturbation is introduced in a regular PCS. The QGMs inherit the spatial dispersion of the GMs supported by the PCS and consequently feature ultrahigh Q-factors, which can be controlled by the level of perturbation over a large bandwidth. The huge local field enhancement, even higher than that in plasmonic nanoantennas, has been demonstrated using numerical simulations. Although a PCS structure in the form of air holes in a silicon slab is used for demonstration, we note the same physics can be extended to other periodic structures such as arrays of silicon rods. The huge local field enhancement together with the possibility of resonance tuning by the incident angle over a large bandwidth make the QGMs a competitive platform for enhanced light–matter interactions and novel applications. For example, in some nonlinear applications, the interactions between the incident light and the medium need to be enhanced simultaneously at multiple wavelengths with largely different values. This requirement can easily go beyond the capability of QBIC resonances. However, it can be easily fulfilled using QGMs by simply choosing the proper incident angles.

Funding

This work is supported by the National Science Foundation of China (11974221, 12274269).

ORCID® iDs

Kaili Sun - https://orcid.org/0000-0002-4455-5177

References

1. Akahane, Y.; Asano, T.; Song, B.-S.; Noda, S. *Nature* **2003,** *425,* 944–947. doi:10.1038/nature02063
2. Vahala, K. J. *Nature* **2003,** *424,* 839–846. doi:10.1038/nature01939
3. Biagioni, P.; Huang, J.-S.; Hecht, B. *Rep. Prog. Phys.* **2012,** *75,* 024402. doi:10.1088/0034-4885/75/2/024402
4. Kuznetsov, A. I.; Miroshnichenko, A. E.; Brongersma, M. L.; Kivshar, Y. S.; Luk'yanchuk, B. *Science* **2016,** *354,* aag2472. doi:10.1126/science.aag2472
5. Hsu, C. W.; Zhen, B.; Stone, A. D.; Joannopoulos, J. D.; Soljačić, M. *Nat. Rev. Mater.* **2016,** *1,* 16048. doi:10.1038/natrevmats.2016.48

6. Kinkhabwala, A.; Yu, Z.; Fan, S.; Avlasevich, Y.; Müllen, K.; Moerner, W. E. *Nat. Photonics* **2009,** *3,* 654–657. doi:10.1038/nphoton.2009.187
7. Adato, R.; Yanik, A. A.; Amsden, J. J.; Kaplan, D. L.; Omenetto, F. G.; Hong, M. K.; Erramilli, S.; Altug, H. *Proc. Natl. Acad. Sci. U. S. A.* **2009,** *106,* 19227–19232. doi:10.1073/pnas.0907459106
8. Jiang, H.; Cai, Y.; Han, Z. *J. Opt. Soc. Am. B* **2020,** *37,* 3146–3151. doi:10.1364/josab.402624
9. Tang, L.; Kocabas, S. E.; Latif, S.; Okyay, A. K.; Ly-Gagnon, D.-S.; Saraswat, K. C.; Miller, D. A. B. *Nat. Photonics* **2008,** *2,* 226–229. doi:10.1038/nphoton.2008.30
10. Overvig, A. C.; Malek, S. C.; Carter, M. J.; Shrestha, S.; Yu, N. *Phys. Rev. B* **2020,** *102,* 035434. doi:10.1103/physrevb.102.035434
11. Lawrence, M.; Barton, D. R., III; Dixon, J.; Song, J.-H.; van de Groep, J.; Brongersma, M. L.; Dionne, J. A. *Nat. Nanotechnol.* **2020,** *15,* 956–961. doi:10.1038/s41565-020-0754-x
12. Overvig, A. C.; Malek, S. C.; Yu, N. *Phys. Rev. Lett.* **2020,** *125,* 017402. doi:10.1103/physrevlett.125.017402
13. Tittl, A.; Leitis, A.; Liu, M.; Yesilkoy, F.; Choi, D.-Y.; Neshev, D. N.; Kivshar, Y. S.; Altug, H. *Science* **2018,** *360,* 1105–1109. doi:10.1126/science.aas9768
14. Cerjan, A.; Hsu, C. W.; Rechtsman, M. C. *Phys. Rev. Lett.* **2019,** *123,* 023902. doi:10.1103/physrevlett.123.023902
15. Cerjan, A.; Jörg, C.; Vaidya, S.; Augustine, S.; Benalcazar, W. A.; Hsu, C. W.; von Freymann, G.; Rechtsman, M. C. *Sci. Adv.* **2021,** *7,* eabk1117. doi:10.1126/sciadv.abk1117
16. Lemarchand, F.; Sentenac, A.; Giovannini, H. *Opt. Lett.* **1998,** *23,* 1149–1151. doi:10.1364/ol.23.001149
17. Fehrembach, A.-L.; Talneau, A.; Boyko, O.; Lemarchand, F.; Sentenac, A. *Opt. Lett.* **2007,** *32,* 2269–2271. doi:10.1364/ol.32.002269
18. Zeng, B.; Majumdar, A.; Wang, F. *Opt. Express* **2015,** *23,* 12478. doi:10.1364/oe.23.012478
19. Overvig, A. C.; Shrestha, S.; Yu, N. *Nanophotonics* **2018,** *7,* 1157–1168. doi:10.1515/nanoph-2017-0127
20. Vyas, H.; Hegde, R. S. *Opt. Mater. Express* **2020,** *10,* 1616–1629. doi:10.1364/ome.395833
21. Jiang, H.; Han, Z. *J. Phys. D: Appl. Phys.* **2022,** *55,* 385106. doi:10.1088/1361-6463/ac7e07
22. Tran, N.-V.-Q.; Combrié, S.; Colman, P.; De Rossi, A.; Mei, T. *Phys. Rev. B: Condens. Matter Mater. Phys.* **2010,** *82,* 075120. doi:10.1103/physrevb.82.075120
23. Jannesari, R.; Dubois, F.; Pühringer, G.; Stocker, G.; Tortschanoff, A.; Grille, T.; Jakoby, B. Vertical coupling into a photonic crystal waveguide using band folding design. In *2021 IEEE Sensors,* Sydney, Australia, Oct 31–Nov 3, 2021; pp 1–4. doi:10.1109/sensors47087.2021.9639543
24. Solnyshkov, D. D.; Weiss, T.; Malpuech, G.; Gippius, N. A. *Appl. Phys. Lett.* **2011,** *99,* 111110. doi:10.1063/1.3639272
25. Johnson, S. G.; Fan, S.; Villeneuve, P. R.; Joannopoulos, J. D.; Kolodziejski, L. A. *Phys. Rev. B* **1999,** *60,* 5751–5758. doi:10.1103/physrevb.60.5751
26. Seok, T. J.; Jamshidi, A.; Kim, M.; Dhuey, S.; Lakhani, A.; Choo, H.; Schuck, P. J.; Cabrini, S.; Schwartzberg, A. M.; Bokor, J.; Yablonovitch, E.; Wu, M. C. *Nano Lett.* **2011,** *11,* 2606–2610. doi:10.1021/nl2010862
27. Fan, S.; Suh, W.; Joannopoulos, J. D. *J. Opt. Soc. Am. A* **2003,** *20,* 569–572. doi:10.1364/josaa.20.000569
28. Notomi, M. *Proc. IEEE* **2011,** *99,* 1768–1779. doi:10.1109/jproc.2011.2123850

License and Terms

BEILSTEIN JOURNAL OF NANOTECHNOLOGY

A mid-infrared focusing grating coupler with a single circular arc element based on germanium on silicon

Xiaojun Zhu[1], Shuai Li[1], Ang Sun[1], Yongquan Pan[1], Wen Liu[1], Yue Wu[1], Guoan Zhang[1] and Yuechun Shi[*2]

Full Research Paper

Open Access

Address:
[1]School of Information Science and Technology, Nantong University, Nantong 226019, China and [2]Yongjiang Laboratory, Ningbo 315202, China and Nanjing University, Key Lab Intelligent Opt Sensing & Manipulat, Minist Educ, Nanjing University, Nanjing 210093, China

Email:
Yuechun Shi[*] - yuechun-shi@ylab.ac.cn

* Corresponding author

Keywords:
circular arc element; focusing grating coupler; germanium-on-silicon; mid-infrared

Beilstein J. Nanotechnol. **2023,** *14,* 478–484.
https://doi.org/10.3762/bjnano.14.38

Received: 05 December 2022
Accepted: 17 March 2023
Published: 06 April 2023

This article is part of the thematic issue "Physics and optical applications of all-dieletric nanostructures".

Guest Editor: Z. Han

Abstract

A mid-infrared (MIR) focusing grating coupler (FGC) with a single circular arc element (CAE) in the front of the gratings based on a germanium-on-silicon (Ge-on-Si) platform is designed and demonstrated. It can be used equivalently to a traditional FGC with all-focusing gratings. By optimizing the structural parameters of the CAE, the combination of a tapered linear grating and the CAE can improve the coupling efficiency to 8.61%, which is twice as large as that of the traditional MIR grating couplers. To the best of our knowledge, it is the highest coupling efficiency in a full-etch grating coupler based on Ge-on-Si. Moreover, the proposed grating coupler can be used for refractive index (RI) sensing, and the maximum sensitivity is 980.7 nm/RIU when the RI changes from 1 to 1.04. By comparing with traditional grating couplers requiring secondary etching, the proposed full-etch grating coupler structure can reduce the complexity of fabrication and can provide a prospective platform for MIR photonic integration and photonic biosensor detection.

Introduction

The mid-infrared (MIR) spectrum region covers the absorption band of most organic and inorganic matter. Thus, it has a broad application prospect in gas detection, environmental monitoring, lidar, free space optical communication, and remote sensing technologies [1,2]. The recombination of chemical bonds caused by changes in molecular structures can induce significant differences in MIR spectra. Thus, slight differences in the structure of compounds or molecules (such as isomers) can be distinguished by mid-infrared spectroscopy [3]. Therefore, this spectral region is called “fingerprint spectrum region” (FSR) [1,4]. Many small biological molecules have unique and identifiable absorption spectra in the MIR band of 6–15 μm

[1,5]. It is of great application value to develop photonic biosensors in this FSR. The spectral transparency window of germanium can fully cover the wavelength of 6–15 μm. Hence, it is a suitable material for biosensors applications in the MIR band [6].

In recent years, researchers have verified the feasibility of Ge MIR waveguides on various substrate materials, such as germanium on silicon (Ge-on-Si), germanium on silicon-on-insulator (GOSI) [7], germanium on insulating substrate (GOI) [8,9], and germanium on silicon nitride substrate (GOSN) [10]. Among them, Ge-on-Si platforms have been widely applied in on-chip sensors, nonlinear optics, free space communication, and thermal imaging [1,6] because portable, cost-effective, and mass-produced integrated systems can be made from such platforms [6]. One key technology is how to couple the MIR light efficiently into the Ge-based waveguides. Many MIR grating couplers have been proposed and demonstrated to achieve this purpose [1,11]. In 2016, Alonso-Ramos et al. reported a Ge-on-Si grating coupler with an inverse taper excitation, operating near 3.8 μm wavelength with a maximum coupling efficiency of −11 dB (7.9%) [11]. In 2017, Kang et al. designed and experimentally demonstrated a focusing subwavelength grating (SWG) for an efficient coupling of MIR light to a suspended membrane Ge waveguide [1]. The maximum coupling efficiency was −11 dB at the focusing SWG's center wavelength of 2.37 μm. The high coupling efficiency was obtained experimentally. However, the fabrication flow of the suspended membrane Ge waveguide with focusing SWGs greatly increased the complexity of the technological process. Therefore, a focusing grating coupler (FGC) with a simple fabrication process and high coupling efficiency is urgently needed.

In this paper, a MIR FGC with a single circular arc element (CAE) based on Ge-on-Si is demonstrated and simulated. The proposed MIR FGC consists of a section of tapered linear gratings and a single CAE, which can be equivalent to the traditional FGC with all-focusing gratings. Also, it is a full-etch grating coupler, which can be achieved by a single etch step. The maximum coupling efficiency can be up to 8.61% (−10.65 dB) at 6.878 μm by optimizing the structural geometry of the CAE. To the best of our knowledge, it is the highest coupling efficiency in full-etch grating couplers based on Ge-on-Si. Moreover, the proposed MIR FGC can also be used for sensing, and the maximum refractive index (RI) sensitivity is 980.7 nm/RIU. Compared with the suspended membrane Ge waveguide with a focusing subwavelength grating MIR grating coupler, the difficulty of preparation has been considerably reduced.

Principle and Design

Figure 1a shows the tilted view of the proposed MIR FGC. The Ge waveguide layer is built onto the Si substrate forming the Ge-on-Si structure. The proposed MIR FGC consists of a section of tapered linear gratings and a single CAE. Figure 1b shows the cross-sectional view of the proposed MIR FGC. The grating period is Λ, the width of the trenches is w, and the duty cycle is defined as $f = w/\Lambda$. The Ge waveguide thickness is h_{etch}, which is also the etching depth. The incident angle is θ. In our work, the numerical simulations have been performed by using a commercial software of Lumerical FDTD solutions, which is based on the finite-difference time-domain method, and the light source we used for exciting the grating coupler is a Gaussian laser beam. The details of the Gaussian beam are as follows: The injection axis is the z axis, the waist radius is 3 μm, and the center wavelength is 7 μm.

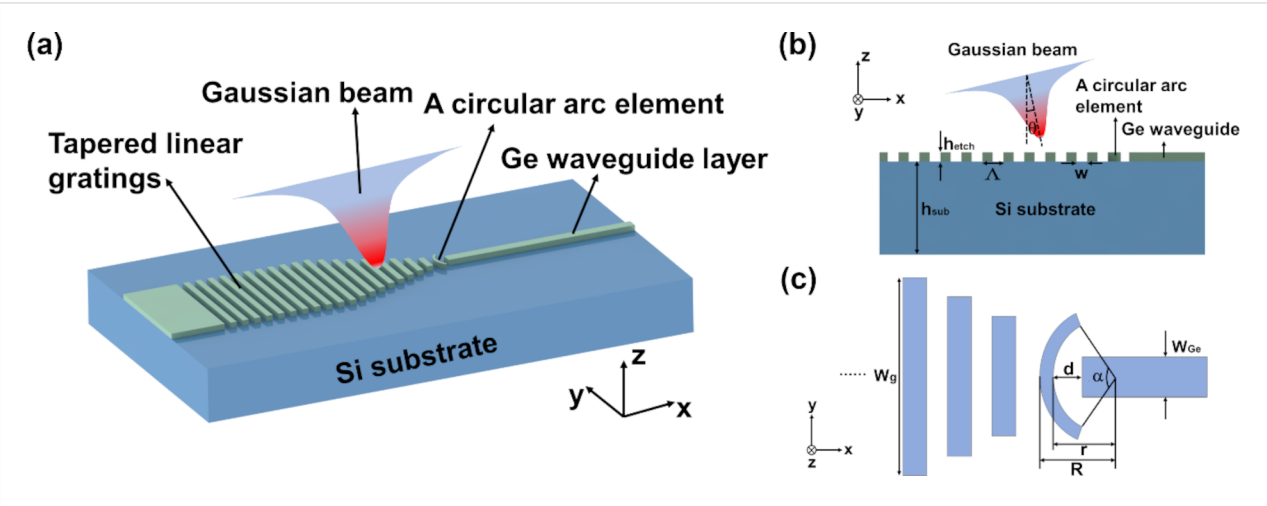

Figure 1: (a) Tilted view and (b) cross-sectional view of the proposed MIR grating coupler. (c) Schematic diagram of the proposed CAE in the MIR grating coupler.

The coupling mechanism of the grating can be characterized as [11]:

$$n_1 \sin(\theta) = n_{\text{eff}} + \frac{k\lambda}{\Lambda}, \quad (1)$$

where n_1 is the refractive index of the surrounding air (n_1 = 1), θ is the coupling angle, λ is the wavelength of the incident light in vacuum, n_{eff} is the effective refractive index of the fundamental mode in the grating, and k is the diffraction order. By convention, the period of the grating couplers is small enough to guarantee that only the first diffraction order (k = −1) satisfies the diffraction condition to produce single-beam diffraction [11]. However, the Ge thickness of Ge-on-Si grating couplers is generally about 2 μm. In addition, if the grating is designed for first-order diffraction (k = −1), it will lead to gratings with a high aspect ratio (defined as the ratio between the etch depth and the width of the grating trench). All these factors increase the difficulty of fabrication in practice. Therefore, Ge-on-Si grating couplers should be designed to work with the second-order diffraction (k = −2) [11].

Figure 1c is the schematic diagram of the proposed CAE in the MIR FGC. The CAE is located between the tapered linear gratings and the output Ge waveguide. R and r are the outer and inner radii of the CAE, respectively. d represents the position of the CAE, and α is the opening angle of the CAE. w_g is the width of the grating in the y direction, which is scanned from 40 to 12 μm in interval steps of 4 μm in the simulation. w_{Ge} is the width of the output Ge waveguide, which is set to 4 μm. The CAE we designed is used to replace a linear grating at the front of the tapered gratings. The focusing effect of the CAE is conducive to coupling the light incident on the surface of the grating coupler to the narrow waveguide. The CAE can also help to reduce reflection and to couple more light into the narrower waveguide to be transmitted forward. In addition, the proposed MIR FGC can be used as a spot-size converter while coupling light from a fiber into the Ge waveguide because of the small size in comparison with a conventional inverted taper grating coupler [12]. Therefore, the combination of the tapered linear gratings and the CAE is not only beneficial to decrease the size of the grating coupler. It also strongly increases the coupling efficiency of the MIR grating coupler.

Results and Discussion

In our work, the incident light angle and the shape of the CAE are the main adjustable parameters when studying the coupling efficiency. The FGC is a full-etch grating with a grating period Λ of 4.5 μm. The Ge waveguide thickness h_{etch} is set to 2 μm, the duty cycle f is 0.5, and k = −2.

Figure 2 shows how the incident angle θ impacts the coupling efficiency when R = 7.15 μm, r = 6.15 μm, d = 3.55 μm, and α = 120°. It can be seen that with the increase of θ, the coupling efficiency first increases, then reaches the maximum value of 8.25% (7.027 μm) when θ = 15°, and finally decreases again. Therefore, an incident angle of θ = 15° yields more light coupled into the Ge waveguide. It should be noted that all coupling efficiencies are above 7% for θ values of 0°–20°, which can be attributed to the fact that the designed MIR grating structure fulfils the Bragg diffraction condition of Equation 1 very well.

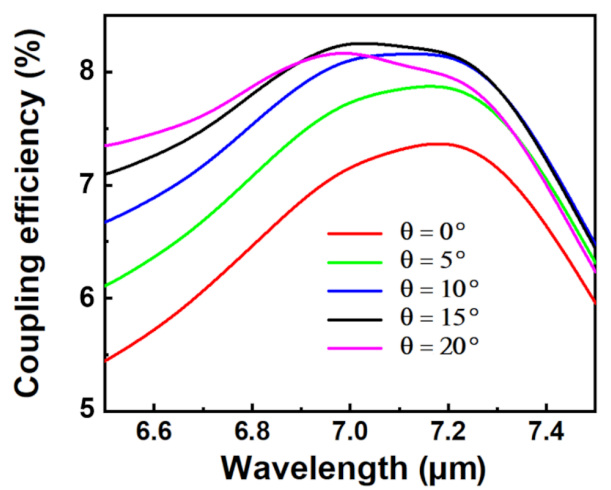

Figure 2: Coupling efficiency of the MIR FGC at different incident angles when R = 7.15 μm, r = 6.15 μm, d = 3.55 μm, and α = 120°.

It is also interesting to see the impacts of the different inner and outer radii of the CAE on the coupling efficiency. The designed parameters are set as θ = 15°, d = 3.55 μm, and α = 120°. Figure 3a shows the coupling efficiency at different R when r is fixed to 6.15 μm. The maximum coupling efficiency of 8.25% (7.027 μm) is obtained when R is 7.15 μm. Figure 3b shows the coupling efficiency at different r when R is fixed to 7.15 μm. The maximum coupling efficiency is 8.25% (7.027 μm) when r is 6.15 μm. It can be seen that the coupling efficiency is almost equal when the values of R and r are changed separately. This is because the changing values of R or r are equivalent to the coupling efficiency with fixed incident angle and position of the CAE.

Figure 4 shows the effects of the CAE opening angle α and position d on the coupling efficiency of the proposed MIR FGC using the parameters θ = 15°, R = 7.15 μm, and r = 6.15 μm. The coupling efficiency changes with the change of α and reaches the maximum of 8.35% (7.017 μm) when α = 110°, as shown in Figure 4a. Figure 4b shows that the parameter d can also affect the coupling efficiency of the proposed MIR FGC,

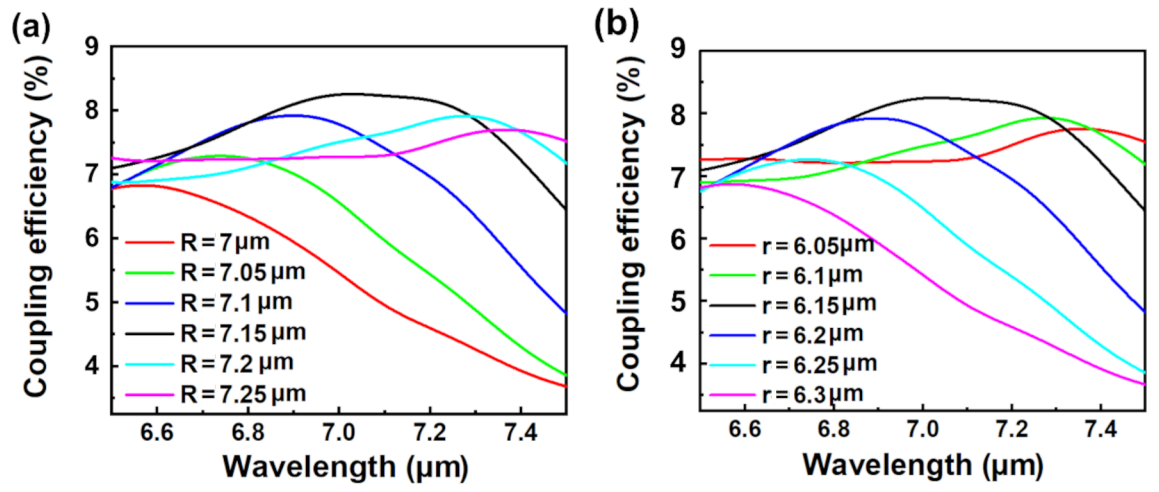

Figure 3: Coupling efficiency of the proposed MIR FGC at different (a) outer radii (r = 6.15 μm) and (b) inner radii (R = 7.15 μm) with θ = 15°, d = 3.55 μm, and α = 120°.

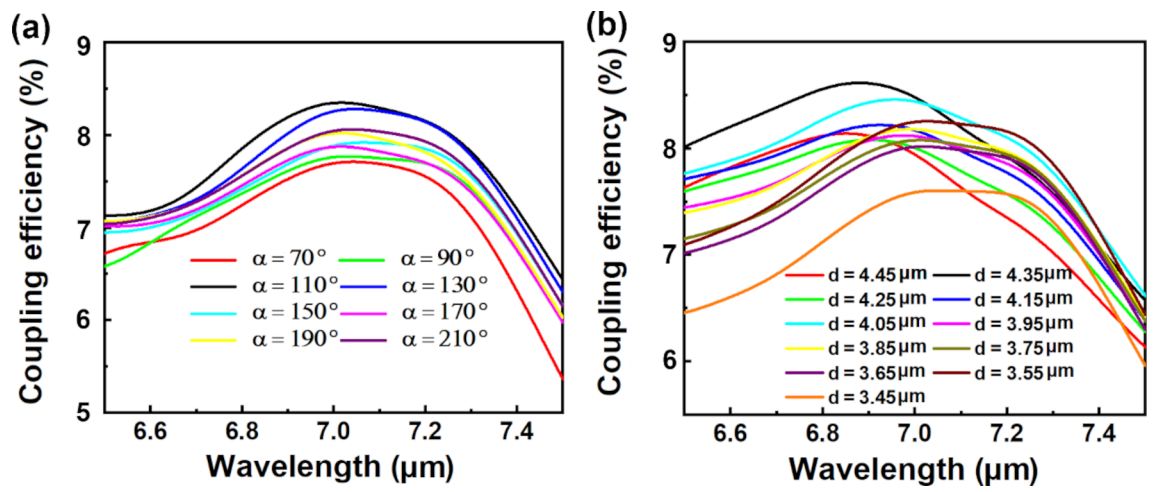

Figure 4: Coupling efficiency of the proposed MIR FGC at different (a) opening angle (d = 3.55 μm) and (b) location (α = 120°) with θ = 15°, R = 7.15 μm, and r = 6.15 μm.

and the maximum coupling efficiency is 8.61% (6.878 μm) when d = 4.35 μm. Furthermore, the total insertion loss (IL) has been estimated, which can be expressed as [13]:

$$\mathrm{IL}\left(\mathrm{dB}\right) = -10\log 10\frac{P_{\mathrm{out}}}{P_{\mathrm{in}}}, \tag{2}$$

where P_{in} and P_{out} stand for input power and output power, respectively. Under the condition of maximum coupling efficiency, the value of $P_{\mathrm{out}}/P_{\mathrm{in}}$ is around 0.647 obtained from simulation. Thus, an IL value of around 8 dB has been calculated using Equation 2.

In order to highlight the advantages of our proposed MIR FGC with a CAE, we have simulated the coupling efficiency of MIR grating couplers with different numbers of CAE and conventional tapered linear gratings, as shown in Figure 5. The simulation conditions are Λ = 4.5 μm, f = 0.5, θ = 15°, and h_{etch} = 2 μm. d of the first CAE is 4.35 μm, α of the CAEs is 120°, and period and duty cycle of the CAEs are 4.25 μm and 0.76, respectively. Comparing the coupling efficiency of MIR FGCs with one CAE, two CAEs, and three CAEs, we can see that the coupling efficiencies are nearly equal, all reaching 8.6%, as shown in Figure 5e. This fact indicates that the coupling efficiency achieved by a single CAE is almost equal to that obtained with multiple CAEs (i.e., with traditionally

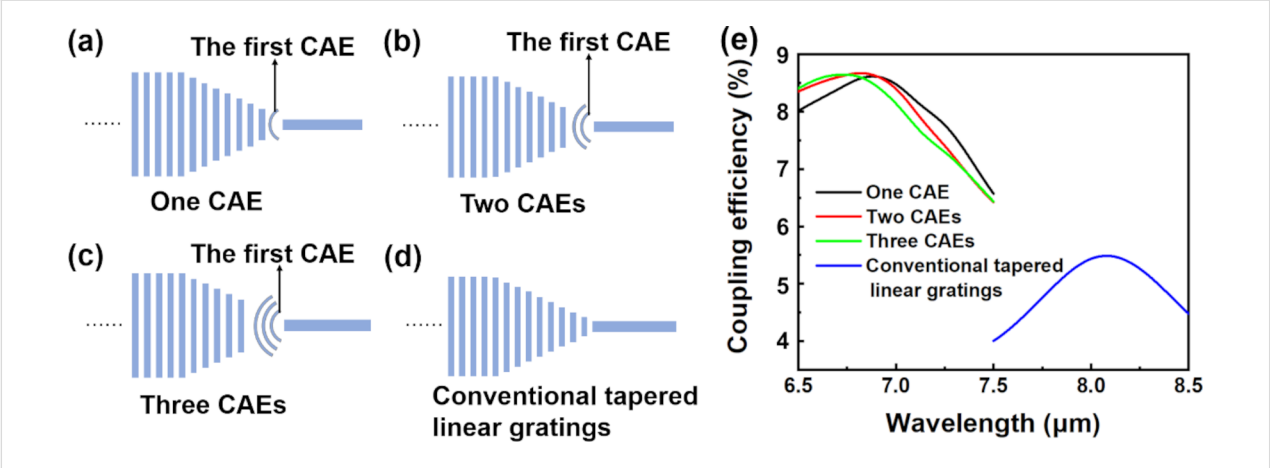

Figure 5: Structures of MIR grating couplers with (a) one single CAE, (b) two CAEs, (c) three CAEs, and (d) conventional tapered linear gratings. (e) Comparison of coupling efficiency of MIR FGCs with different structures.

focusing gratings). This is very significant regarding the practical manufacturing with the requirements of reducing production cost and complexity while pursuing high coupling efficiency. Moreover, it should be emphasized that the coupling efficiency of the proposed MIR FGC with a single CAE (8.61%) is much higher than that of a MIR grating coupler with conventional tapered linear gratings (5.49%). Because the proposed structure is geometrically simple, it is easy to implement experimentally. The proposed MIR FGC based on Ge-on-Si can be fabricated by electron beam lithography (EBL) and inductively coupled plasma etching (ICP). EBL is used to produce lithographically the grating pattern into the resist, which can be further transferred onto the Ge layer by ICP. This is a simple manufacturing process that requires only one single etch step. Then, we can use a continuous-wave single-frequency tunable MIR laser (the center wavelength is ca. 7 μm) as the light source to test the coupling efficiency of the experimental samples. The MIR laser is coupled into a single-mode ZrF_4 optical fiber via a black diamond-2 aspheric lens [1]. The light from the single-mode ZrF_4 optical fiber is coupled into the proposed MIR grating coupler [14]. Finally, the transmission characteristics of the output fiber can be detected using an optical spectrum analyzer.

There is a wide range of sensors for applications in, for example, biosensing, healthcare, disease detection, and gas detection. Therefore, research on those sensors is of great significance. In 2015, Bai et al. reported a flexible healable transparent chemical gas sensing device that exhibited robust flexibility, good transparency, and reliable water-enabled healability of the gas sensing performance at room temperature [15]. Wang proposed a flexible, transparent, and portable wrist strap sensor and a mechano-based transductive sensor in 2017 and 2018, respectively [16,17]. They have good application prospects in healthcare. In 2020, Xue et al. reported a bismuthene-enabled fluorescence quenching biosensor to detect microRNA, which is relevant to the fields of biosensors and medicine [18]. In 2022, Chen et al. demonstrated a methodology of photonic clustered regularly interspaced short palindromic repeat (CRISPR) sensing for rapid and specific diagnosis of the Omicron variant of SARS-CoV-2 [19]. This innovative CRISPR-empowered surface plasmon resonance platform will further contribute to the field of biomedical sensors. We also studied the sensing performance of our proposed MIR FGC when it worked as a sensor rather than a coupler, as shown in Figure 6. When RI increases from 1 to 1.04, the peak of coupling efficiency shows a redshift from 6877.8 nm to 6917.1 nm. The RI sensitivity is 980.7 nm/RIU obtained from a linear fit of the peak wavelength and RI, as shown in Figure 6b. The sensitivity is twice as large as that in [20]. Furthermore, the proposed sensor is a full-etch structure based on Ge-on-Si, which can be achieved by a single etch step. The manufacture is simple compared with multiple etching [1]. Therefore, after considering the production process, production cost and sensitivity, our proposed sensor based on Ge-on-Si is expected to have commercially available applications in the future.

Conclusion

In summary, we designed and demonstrated a full-etch MIR FGC with a single CAE. The coupling efficiency could be tuned by changing the structural parameters of the CAE and the incident angle of light. The maximum coupling efficiency of 8.61% (−10.65 dB) was obtained at a wavelength of 6.878 μm. Moreover, the coupling efficiency of the single CAE was equivalent to that of multiple CAEs, such as in focusing gratings, which could significantly reduce the production cost and complexity while keeping high coupling efficiency. In addition, the RI sensing performance of the proposed MIR grating coupler was

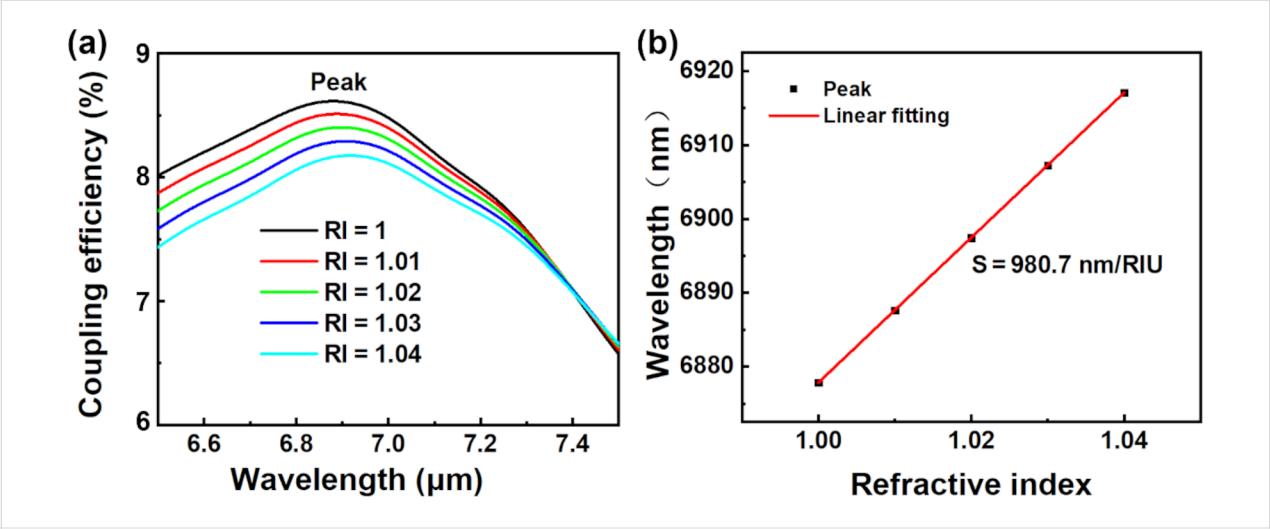

Figure 6: Sensing performance of the proposed MIR FGC.

also simulated when it was used as a sensor. The RI sensitivity of the sensor was 980.7 nm/RIU. Therefore, the proposed MIR FGC would provide a potential platform for MIR photonic integration and photonic biosensors detection based on chips.

Funding

Six Talent Peaks Project in Jiangsu Province under Grant KTHY-052; Science and Technology program of Nantong under Grant JC2021037; Fundamental Research Funds for the Central Universities under Grant 021314380095; National Natural Science Foundation of China under Grant 61975075 and Grant 61971245; Science and Technology Project and Natural Science Foundation of Jiangsu province under Grant BE2019101; Key Lab of Advanced Optical Manufacturing Technologies of Jiangsu Province & Key Lab of Modern Optical Technologies of Education Ministry of China, Soochow University under Grant KJS1858; Postgraduate Research & Practice Innovation Program of Jiangsu Province under Grant KYCX22_3345.

References

1. Kang, J.; Cheng, Z.; Zhou, W.; Xiao, T.-H.; Gopalakrisna, K.-L.; Takenaka, M.; Tsang, H. K.; Goda, K. *Opt. Lett.* **2017,** *42,* 2094–2097. doi:10.1364/ol.42.002094
2. Nedeljkovic, M.; Penades, J. S.; Mittal, V.; Murugan, G. S.; Khokhar, A. Z.; Littlejohns, C.; Carpenter, L. G.; Gawith, C. B. E.; Wilkinson, J. S.; Mashanovich, G. Z. *Opt. Express* **2017,** *25,* 27431–27441. doi:10.1364/oe.25.027431
3. Hirano-Iwata, A.; Yamaguchi, R.-t.; Miyamoto, K.-i.; Kimura, Y.; Niwano, M. *J. Appl. Phys.* **2009,** *105,* 102039. doi:10.1063/1.3116611
4. Mittal, V.; Nedeljkovic, M.; Carpenter, L. G.; Khokhar, A. Z.; Chong, H. M. H.; Mashanovich, G. Z.; Bartlett, P. N.; Wilkinson, J. S. *ACS Sens.* **2019,** *4,* 1749–1753. doi:10.1021/acssensors.9b00215
5. Shankar, R.; Lončar, M. *Nanophotonics* **2014,** *3,* 329–341. doi:10.1515/nanoph-2013-0027
6. Hu, T.; Dong, B.; Luo, X.; Liow, T.-Y.; Song, J.; Lee, C.; Lo, G.-Q. *Photonics Res.* **2017,** *5,* 417–430. doi:10.1364/prj.5.000417
7. Younis, U.; Lim, A. E.-J.; Lo, P. G.-Q.; Bettiol, A. A.; Ang, K.-W. *IEEE Photonics Technol. Lett.* **2016,** *28,* 2447–2450. doi:10.1109/lpt.2016.2600503
8. Kang, J.; Takenaka, M.; Takagi, S. *Opt. Express* **2016,** *24,* 11855–11864. doi:10.1364/oe.24.011855
9. Li, W.; Anantha, P.; Bao, S.; Lee, K. H.; Guo, X.; Hu, T.; Zhang, L.; Wang, H.; Soref, R.; Tan, C. S. *Appl. Phys. Lett.* **2016,** *109,* 241101. doi:10.1063/1.4972183
10. Li, W.; Tan, C. S.; Anantha, P.; Lee, K. H.; Qiu, H. D.; Guo, X.; Goh, S. C. K.; Zhang, L.; Wang, H.; Soref, R. A. *IEEE Photonics J.* **2018,** *10,* 1–7. doi:10.1109/jphot.2018.2829988
11. Alonso-Ramos, C.; Nedeljkovic, M.; Benedikovic, D.; Penadés, J. S.; Littlejohns, C. G.; Khokhar, A. Z.; Pérez-Galacho, D.; Vivien, L.; Cheben, P.; Mashanovich, G. Z. *Opt. Lett.* **2016,** *41,* 4324–4327. doi:10.1364/ol.41.004324
12. Yang, B.; Li, Z.-Y.; Yu, Y.-D.; Yu, J.-Z. *Chin. Phys. B* **2014,** *23,* 114206. doi:10.1088/1674-1056/23/11/114206
13. Guo, Z.; Xiao, J. *Opt. Commun.* **2021,** *488,* 126850. doi:10.1016/j.optcom.2021.126850
14. Dong, B.; Hu, T.; Luo, X.; Chang, Y.; Guo, X.; Wang, H.; Kwong, D.-L.; Lo, G.-Q.; Lee, C. *Nanomaterials* **2018,** *8,* 893. doi:10.3390/nano8110893
15. Bai, S.; Sun, C.; Yan, H.; Sun, X.; Zhang, H.; Luo, L.; Lei, X.; Wan, P.; Chen, X. *Small* **2015,** *11,* 5807–5813. doi:10.1002/smll.201502169
16. Wang, T.; Guo, Y.; Wan, P.; Sun, X.; Zhang, H.; Yu, Z.; Chen, X. *Nanoscale* **2017,** *9,* 869–874. doi:10.1039/c6nr08265c
17. Wang, T.; Yang, H.; Qi, D.; Liu, Z.; Cai, P.; Zhang, H.; Chen, X. *Small* **2018,** *14,* 1702933. doi:10.1002/smll.201702933
18. Xue, T.; Bongu, S. R.; Huang, H.; Liang, W.; Wang, Y.; Zhang, F.; Liu, Z.; Zhang, Y.; Zhang, H.; Cui, X. *Chem. Commun.* **2020,** *56,* 7041–7044. doi:10.1039/d0cc01004a
19. Chen, Z.; Li, J.; Li, T.; Fan, T.; Meng, C.; Li, C.; Kang, J.; Chai, L.; Hao, Y.; Tang, Y.; Al-Hartomy, O. A.; Wageh, S.; Al-Sehemi, A. G.; Luo, Z.; Yu, J.; Shao, Y.; Li, D.; Feng, S.; Liu, W. J.; He, Y.; Ma, X.; Xie, Z.; Zhang, H. *Natl. Sci. Rev.* **2022,** *9,* nwac104. doi:10.1093/nsr/nwac104

20. Prokop, C.; Irmler, N.; Laegel, B.; Wolff, S.; Mitchell, A.; Karnutsch, C. *Sens. Actuators, A* **2017,** *263,* 439–444. doi:10.1016/j.sna.2017.07.014

License and Terms

BEILSTEIN JOURNAL OF NANOTECHNOLOGY

Investigations on the optical forces from three mainstream optical resonances in all-dielectric nanostructure arrays

Guangdong Wang and Zhanghua Han*

Full Research Paper

Open Access

Address:
Shandong Provincial Key Laboratory of Optics and Photonic Devices, Center of Light Manipulation and Applications, School of Physics and Electronics, Shandong Normal University, Jinan 250358, China

Email:
Zhanghua Han* - zhan@sdnu.edu.cn

* Corresponding author

Keywords:
all-dielectric nanostructures; anapole; optical force; quasi-bound states in the continuum; toroidal dipole

Beilstein J. Nanotechnol. **2023,** *14,* 674–682.
https://doi.org/10.3762/bjnano.14.53

Received: 31 December 2022
Accepted: 16 May 2023
Published: 02 June 2023

This article is part of the thematic issue "Physics and optical applications of all-dieletric nanostructures".

Associate Editor: A. Gölzhäuser

Abstract

Light can exert radiation pressure on any object it encounters, and the resulting optical force can be used to manipulate particles at the micro- or nanoscale. In this work, we present a detailed comparison through numerical simulations of the optical forces that can be exerted on polystyrene spheres of the same diameter. The spheres are placed within the confined fields of three optical resonances supported by all-dielectric nanostructure arrays, including toroidal dipole (TD), anapoles, and quasi-bound states in continuum (quasi-BIC) resonances. By elaborately designing the geometry of a slotted-disk array, three different resonances can be supported, which are verified by the multipole decomposition analysis of the scattering power spectrum. Our numerical results show that the quasi-BIC resonance can produce a larger optical gradient force, which is about three orders of magnitude higher than those generated from the other two resonances. The large contrast in the optical forces generated with these resonances is attributed to a higher electromagnetic field enhancement provided by the quasi-BIC. These results suggest that the quasi-BIC resonance is preferred when one employs all-dielectric nanostructure arrays for the trapping and manipulation of nanoparticles by optical forces. It is important to use low-power lasers to achieve efficient trapping and avoid any harmful heating effects.

Introduction

Optical forces have two components (i.e., scattering force and gradient force [1]) and the motion of tiny particles within an optical field is determined by both of them. The scattering force originates from the photon momentum transferred to the particle caused by the scattering and absorption of photons. As a result, the scattering force is along the direction of light propagation, which is not conducive for object capturing. The gradient force is along the gradient direction of the non-uniform distribution of the light intensity in space, and is well-known for its application in optical tweezers [2]. Therein a strong laser

beam generates a piconewton level of force, which can be used to manipulate small dielectric particles, including biological entities such as DNA, enzymes, and cells. The underlying physics of nanoparticle manipulation by optical tweezers can be interpreted as the trend of the particle to move to a region of high field strength to reduce its energy [3]. Unfortunately, due to the diffraction limit, light cannot be focused onto the subwavelength volume; so it is very difficult for optical tweezers to capture nanoscale objects. Recently, plasmonic nanotweezers have proved their capability to effectively capture subwavelength nanoparticles by overcoming the diffraction limit [4], which has aroused broad research interest. However, due to the high loss of metals, the Joule heating effect caused by the absorption of light leads to increasing temperatures of plasmonic nanotweezers, and may generate a detrimental effect to the captured particles. In this context, all-dielectric nanostructures made from lossless materials are preferable to be used. With the possibility to support various types of electromagnetic resonances (e.g., toroidal dipole (TD), anapole, or bound state in the continuum (BIC)) which are current in focus nanophotonics research topics, all-dielectric nanostructures have proved themselves to be a good platform for light–matter interactions and an advantageous alternative to their plasmonic counterparts.

A TD resonance is produced by the flow of electric currents on the surface of a torus along its meridians, which excite a set of magnetic dipoles (MDs) arranged head-to-tail into a closed loop [5]. First proposed by Zel'dovich in atomic physics [6], and existing widely in elementary particles and condensed matter, such as multiferroic materials [7], the TD cannot interact directly with electromagnetic waves and is often masked by electric dipoles (EDs) or magnetic dipoles (MDs) with stronger responses. However, the TD has a unique current distribution, which can generate a strong near-field localization effect, so it has broad application scenarios [8]. The anapole [9] mode is produced by nanostructures with both ED and TD excitations at the same time. The ED and TD moments generate radiation fields of the same pattern but with opposite phases, leading to the destructive interference of radiation fields. In the far-field region, it can be observed that the radiation field significantly decreases or even vanishes in the scattering spectrum at a specific wavelength. In dielectric materials, the anapole mode is mainly confined to the interior of the structure and does not strongly extend into the surrounding medium [10].

The BIC is a wave excitation which remains spatially localized while the frequency co-exists within a continuum of radiations. Although this concept was first proposed in the field of quantum mechanics [11], it has also attracted much attention in recent years in photonics [12] due to its ability to achieve high-quality (Q) factor resonance and the associated high-field enhancement. The ideal BIC has an infinite Q-factor and zero resonance linewidth, so it can only exist as a mathematical quantity and cannot be excited by free-space radiations. However, with some intentional perturbations in the geometry or objective loss channels, such as surface roughness, a BIC will turn into a quasi-BIC mode with both the Q-factor and resonant bandwidth becoming limited. Many applications of quasi-BICs have been reported, including ultrasensitive sensing [13], ultranarrow bandwidth filters [14], and enhanced nonlinear effects [15]. The BICs are usually categorized into several types [16], and in this work we are concerned with the symmetry-protected BIC. This type of BIC is formed due to a symmetry mismatch between the mode distribution and the free space radiations (e.g., a plane wave). When a structural perturbation is introduced into the system to break the symmetry, the coupling to external radiations can be enabled with the efficiency controlled by the level of perturbation. These quasi-BICs can provide higher Q-factors and usually higher field enhancement than those of the TD resonance and the anapole mode. As a result, the quasi-BICs are expected to provide a larger field gradient which provides higher capability in the applications of nanoparticle capturing. However, a complete investigation and comparison of the optical forces which can be provided by these resonances is still missing.

In this work, we present some numerical results to compare the optical trapping capability provided by all-dielectric nanostructures based on the excitation of these three different modes. Using an array of high-index silicon disks with elaborately designed slots, all these three resonances can be supported by the same platform. The scattering spectra of these modes are analyzed by the multipole decomposition method, which ensures that strong TD response, the anapole mode composed of simultaneously working TD and ED momentums, and the quasi-BIC resonance arising from an out-of-plane MD mode can all be excited using similar structures. The transmission spectrum through a periodic disk array and the electromagnetic fields in resonance were numerically investigated by the finite element method (FEM) implemented in the commercial software COMSOL Multiphysics. In all calculations, we investigated the generated optical forces on nanoscale polystyrene (PS) spheres in the slot of the all-dielectric nanostructures. All these spheres have their own response to the incident radiations (e.g., Mie resonances). However, we noted that due to the small size of the spheres and the relatively lower refractive index of the polymeric material, these resonances by the spheres are beyond the spectrum of our interest. The presence of PS spheres only leads to some spectral shift of the resonances supported by the silicon nanostructure, which have been fully considered. Using the Maxwell stress tensor (MST) technique [17], the generated

optical forces on these spheres placed within the near field of these modes are calculated, analyzed, and compared. We found that the optical force applied on the same PS sphere by the quasi-BIC mode under the same excitation power is about three orders of magnitude larger than those from the other two modes. Furthermore, our calculations show that even for nanoscale spheres, the quasi-BIC resonance can still provide a large optical force that allows for an effective trapping of these spheres.

Results and Discussion

Figure 1a illustrates the schematic of the metasurface structure, where the small green objects on top of the silicon disks represent the trapped PS spheres. The metasurface consists of a 225 nm thick array of silicon disks on a quartz substrate with elliptical slots etched perforating each disk. The number and positions of the slots depend on the specific mode to be excited, and may be different for those three kinds of resonances. Figure 1b presents the top view of one unit cell, where the geometrical parameters are described in the caption. A linearly polarized plane wave is normally incident to the metasurface, with the polarization along the x-direction to excite all the TDs, anapoles, and the quasi-BIC resonances. For all cases, the metasurface structure is assumed to be immerged in water (n = 1.31) to model a realistic suspending condition for the PS nanospheres. The optical forces on the PS at the excitation values of those three resonances are all calculated based on the MST technique, with the input power intensity set as 1 mW/μm^2.

Within the framework of classical electrodynamics, the components of the total time-averaged force F acting on an illuminated object can be calculated using the surface integral:

$$\langle F_{\mathbf{i}} \rangle = \oiint_S \langle T_{ij} \rangle n_j \, \mathrm{d}S, \tag{1}$$

where S is a closed surrounding surface, n is the unit vector perpendicular to and pointing toward the outside of the surface, and $\langle T_{ij} \rangle$ is the time-averaged MST [18] defined by

$$\langle T_{ij} \rangle = 0.5\,\mathrm{Re}\left[\begin{array}{l} \varepsilon\varepsilon_{\mathrm{r}}\left(E_{\mathbf{i}}E_{\mathbf{j}}^{*} - 0.5\delta_{ij}|\mathbf{E}|^2\right) + \\ \mu_0\mu_{\mathrm{r}}\left(H_{\mathbf{i}}H_{\mathbf{j}}^{*} - 0.5\delta_{ij}|\mathbf{H}|^2\right) \end{array}\right], \tag{2}$$

where the indices i and j denote x, y, or z components of the electric or magnetic field; ε_{r} and μ_{r} are the relative permittivity and the relative permeability of the surrounding medium, respectively. In this work, we use a small virtual cube to accommodate a small object (i.e., the PS sphere) and all surfaces of the cube are in water. The electromagnetic fields at the six surfaces of the virtual cube are used to calculate the optical force according to Equation 2. With numerical calculations, the local electromagnetic fields within the structure at the excitation value of a specific resonance can be calculated. From this value one can estimate the generated optical forces combining Equation 1 and Equation 2.

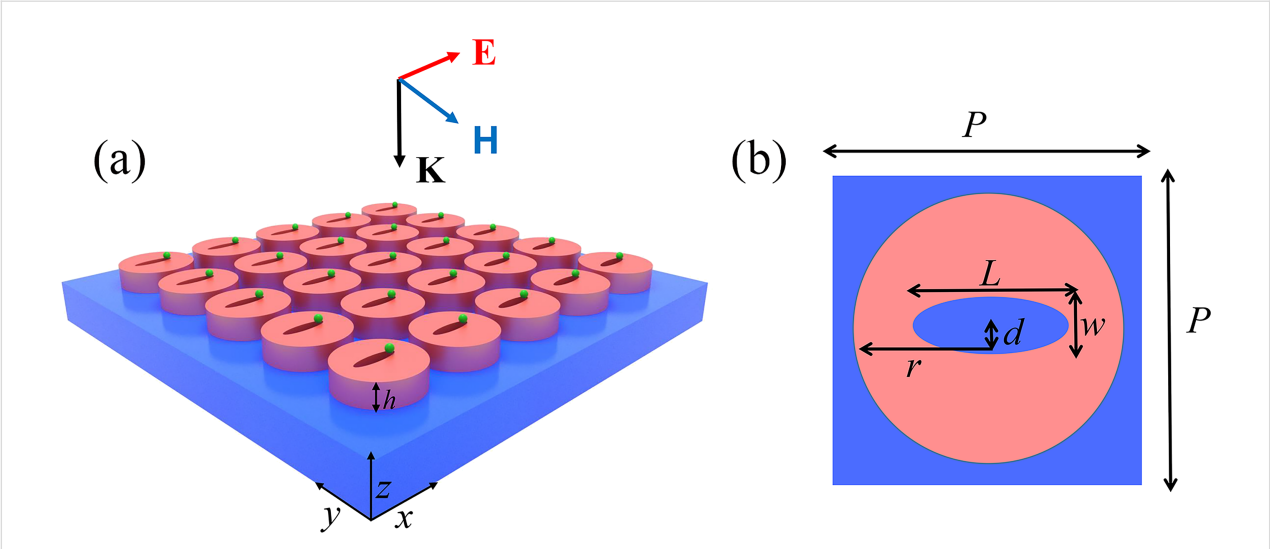

Figure 1: (a) Schematic overview of the metasurface structure composed of a silicon slotted-disk array on a quartz substrate. The trapped nanoscale particles and the incident plane wave are also illustrated. (b) Top view of one unit cell of the slotted-disk array. The geometrical parameters are as follows: array period P = 880 nm, disk radius r = 390 nm, thickness h = 225 nm, slot length L = 420 nm, and slot width w = 90 nm. In this work, all these parameters remain constant while the number of slots and the distance d between the centers of the disk and the slot depend on the specific resonance to be excited, which is discussed in the main text.

Optical force with toroidal dipole excitation

It is known that the excitation of the TD resonance requires the presence of a set of magnetic dipoles arranged head-to-tail to form a closed loop. This kind of TD resonance is usually called magnetic TD. In contrast, the TD response due to a circular configuration of electric dipoles is called electric TD. In this work, we focus only on the magnetic TD and then use only TD instead for simplicity. To fulfill the requirement of using a closed loop of magnetic dipoles, two perforating elliptical slots are used with mirror symmetry with respect to the x–z plane across the center of the disk, and each slot is shifted from the disk center by a distance of d = 80 nm. Figure 2a presents the calculated transmission spectrum through this structure with the incident electric field polarized along the x-direction. It can be seen that a strong asymmetric optical resonance of the Fano-type is located around 1627 nm with a resonance Q-factor of 175. The electric and magnetic field amplitude distributions at the resonance wavelength are plotted in Figure 2b, where the white arrows represent the electric displacement current vectors. It is seen that the electromagnetic field is well confined within the silicon disk. Although the optical force is dependent on the laser power, we should note that the light transmission spectra through the array is not if the nonlinear effect is ignored. So in the calculations of the transmission spectra and the on-resonance field distributions, the electric field magnitude of the incident plane wave is set as 1 [V/m]. Then the maximum electric field in Figures 2b, 3b, and 4b straightforwardly give the enhancement capability of the corresponding resonance. Moreover, two circular displacement currents with reverse rotational directions are formed in the x–y plane of the disk, indicating that two MD resonances with opposite momentum directions are formed. Since the whole structure is symmetric in the y-direction, the two MDs have the same amplitude. These two MDs form a closed loop, leading to a TD momentum along the x-axis (see the left part of Figure 2b). In other words, a plane wave polarized along the x-axis can excite a TD resonance in this structure. In order to further confirm this, we analyzed the contributions to the total scattering power spectrum from five different multipoles, including the ED (P), MD (M), electric quadrupole (QE), magnetic quadrupole (QM), and magnetic toroidal dipole (T) in the Cartesian coordinate system using the multipole decomposition technique. The multipole expansion is

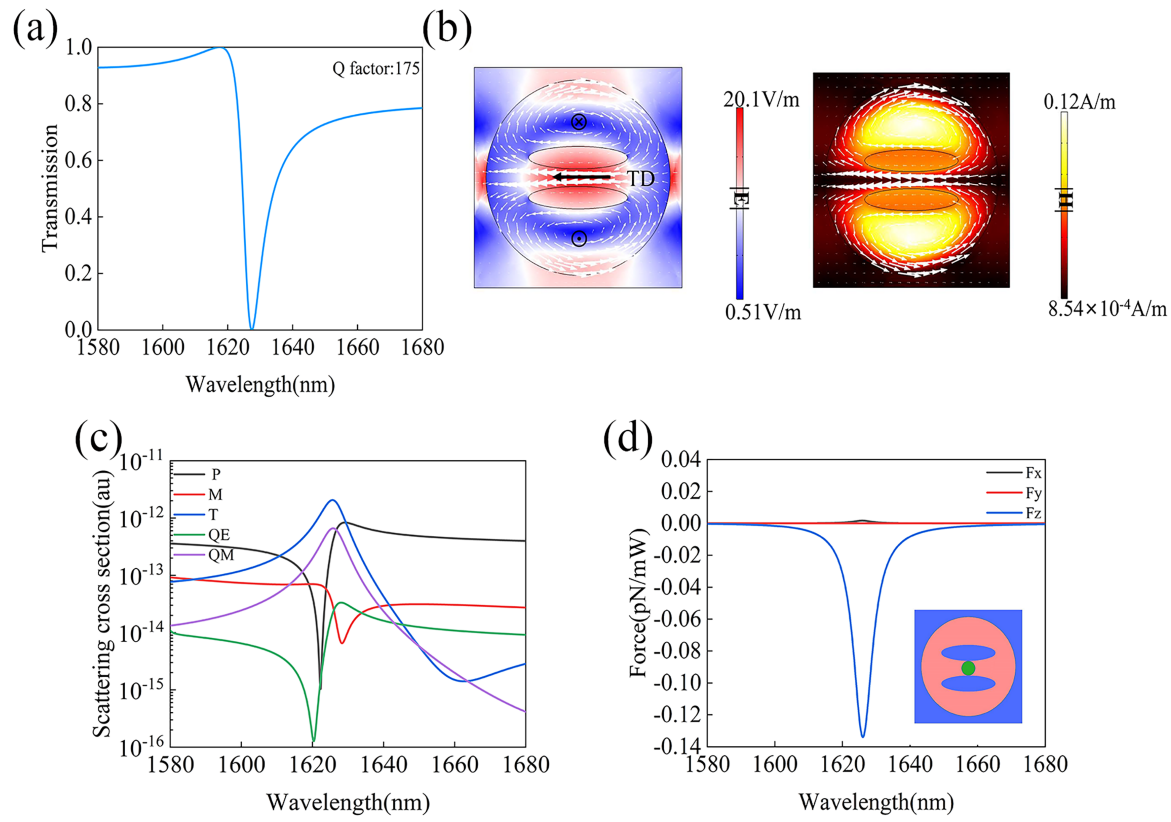

Figure 2: (a) Transmission spectrum through the metasurface supporting the TD resonance. (b) Electric and magnetic field distributions at the TD resonance, where the white arrows represent the displacement current vectors. (c) Multipole analysis of the overall scattering spectrum. (d) The calculated optical force exerted on the PS sphere as a function of the wavelength; the inset shows the geometry of one unit cell of the double-slotted silicon disk array. Both slots are shifted by a distance of d = 80 nm from the center of the disk.

achieved based on the electric displacement current using the following formula:

$$J = i\omega\varepsilon_0\left(\varepsilon_r - n^2\right)E, \tag{3}$$

where ε_0 represents the vacuum dielectric constant, n is the refractive index of the uniform background above the metasurface structure, in which the virtual domain used to calculate the optical force is defined and the displacement currents used for multipole analysis are obtained, and E is the total electric field inside the disk. The multipole analysis is normally used for isolated nanoparticles. However, for periodic nanostructures, especially when the unit cell is much smaller than the incident wavelength and all dipoles can be assumed to oscillate in phase, the formula of the multipole decomposition can also be used [19,20]. The obtained results will provide important insight into the origin of the observed resonances in the transmission/reflection spectra of the periodic structures. Following this approach, we performed the multipole analysis and the results are presented in Figure 2c. It is evident that at the resonance wavelength of 1627 nm, the TD contribution in the scattering power dominates, while the ED and MD contributions are both suppressed. The suppressing is due to the excitation of multiple EDs and MDs in the structure, which will cancel each other out in the far-field radiations. For example, the displacement current distribution vector diagram on the left side of Figure 2b shows that the strong displacement current excited between the two slots will be balanced by the two external displacement currents on the top and bottom sides of the disc (i.e., the ED is weaker in this case). At the same time, we can also see from Figure 2c that the higher-order QE resonance is significantly suppressed, while the QM resonance is slightly lower than the TD resonance. These results confirm that the Fano-type transmission dip in Figure 2a can be considered as resulting from the coupling between the excited TD and QM resonances.

Because the optical gradient force is proportional to the gradient of the local electric field intensity (i.e., $F_{grad} \propto \nabla|E(r)|^2$), the PS sphere gets trapped where the electric field has the highest value. In the metasurface structure supporting the TD resonance, the PS sphere is eventually stabilized between the two elliptical slots. Figure 2d shows the calculated optical force on the PS sphere using Equation 1 as a function of the wavelength. The PS sphere has a diameter of 50 nm and is assumed to be located at the position of (x_0, y_0, z_0) = (0, 0, 260 nm), which is 35 nm above the top surface of the disk, as illustrated by the inset of Figure 2d. It can be seen from the results that the peak of the optical force is achieved at the TD resonance, with the component of F_z being much higher than the other two. The peak value of F_x on the PS sphere is about 0.0017 pN/mW, F_y = 0, and F_z about −0.134 pN/mW. The counterintuitive nonzero F_x value even when the structure is symmetric along the x-direction is associated with the slightly asymmetric field distributions at the peak of a Fano resonance [21], which can be seen in Figure 1b. This indicates that the PS sphere does not get stably trapped at a fixed position above the disk surface, but is pulled towards the center of the disk in the negative z-direction.

Optical force with the anapole excitation

The anapole resonance needs the simultaneous excitations of a TD and an ED, whose radiations into the far field should be out of phase to form a destructive interference to eliminate the overall scattering. We used one elliptical slot at the center of the silicon disk (i.e., d = 0 nm) while the other geometrical parameters remain the same as in Figure 1. Figure 3a presents the simulated transmission spectrum through this metasurface structure with the incident electric field along the x-direction. One can see that a strong optical resonance with similar asymmetric Fano profile as shown in Figure 2a is located around 1680 nm, with a Q-factor of about 106. The results of the multipole analysis to be discussed later confirm the anapole characteristic of this resonance. The electric and magnetic field distributions at the resonance are shown in Figure 3b, where the white arrows also represent the electric displacement current vectors. The enhancement of the electric and magnetic fields at the resonance is smaller compared to those at the TD resonance in Figure 2b. As can be seen from Figure 3b, two current loops with opposite circulation directions are excited on different sides of the elliptical slot, indicating that the TD momentum is along the x-axis. Although similar current loops can be observed in the lower and upper semicircles of the silicon disk in both Figure 2b and Figure 3b, we note that a much stronger current at the upper and lower edges of the silicon disk can be found in Figure 3b, suggesting that a nonzero net ED remains in this metasurface. It is the destructive interference between the TD and the net ED resonances which leads to the excitation of the final anapole mode.

To further analyze the contributions from different multipoles to the observed resonance in Figure 3a, we performed a similar multipole analysis of the scattered power as a function of wavelength. It is clearly seen in Figure 3c that the TD and ED are the two major components in this system. At the resonance wavelength of 1680 nm, the ED and TD have the same magnitude. In addition, we can clearly see in Figure 3d that TD and ED have opposite phases and the phase difference between TD and ED at 1680 nm $|(P)-(ikT)|$ is approximately equal to π. These results confirm that the resonance in Figure 3a is mainly caused by the destructive interference between ED and TD moments, which in turn leads to the anapole response. Figure 3e shows the calculated optical force as a function of wavelength on a PS

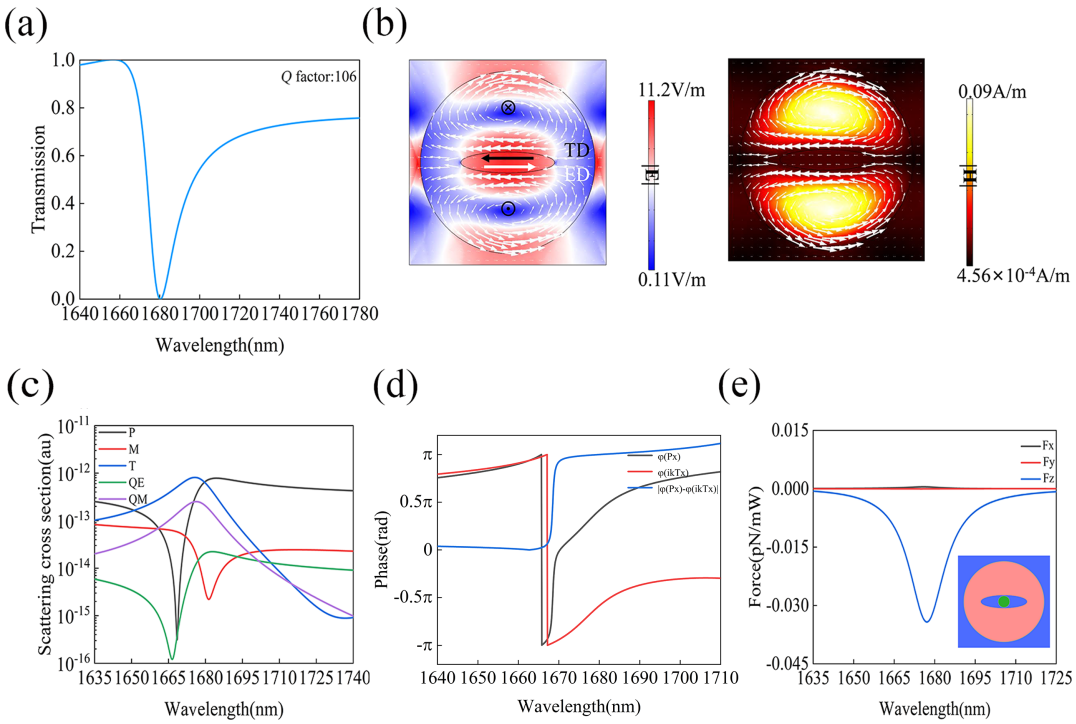

Figure 3: (a) Transmission spectrum through the metasurface supporting the anapole resonance. (b) Electric and magnetic field distributions at the anapole wavelength, where the white arrow represents the displacement current vectors. (c) Multipole analysis of the overall scattering spectrum. (d) The phases of *P*, *ikT*, and their phase difference. (e) The optical force on the PS sphere as a function of wavelength; the inset shows one unit cell of the geometry and the position of the PS sphere.

sphere with a diameter of 50 nm. The position of the PS sphere with respect to the geometry of the anapole system is illustrated by the inset of Figure 3e. The PS sphere is assumed to be at the same position as that in Figure 2 (i.e., (x_0, y_0, z_0) = (0, 0, 260 nm)). It can be seen that the major optical force component is still F_z, which is consistent with the results obtained with the TD resonance presented in Figure 2d. However, both peak values of F_x and F_z achieved with the anapole resonance are slightly smaller than those with the TD resonance. For F_z, the force relative to the TD resonance is −0.134 pN/mW, which is 3.92 times larger than that from the anapole. For F_x, the contrast is about 3.4 times, 0.0017 pN/mW with the TD versus 0.0005 pN/mW with the anapole. The smaller optical force achieved with the anapole compared to that of the TD resonance is attributed to a weaker local field enhancement achieved at the anapole resonance. From Figure 3a and Figure 3b, one can see a smaller Q-factor (106) at the anapole resonance and a weaker local electric field enhancement (11.2) compared to those of the TD resonance.

Optical force with the quasi-BIC excitation

The quasi-BIC mode with unprecedented ultra-high Q-factor and associated ultra-high field enhancement is expected to provide a large optical force, considering that the optical gradient force is directly proportional to the field enhancement. To have a fair comparison, we used the same silicon disk array which supports an out-of-plane MD resonance. This resonance can not be excited by an incident plane wave due to the symmetry incompatibility, giving rise to a BIC resonance of the symmetry-protected type. In order to excite the resonance, we intentionally shifted the elliptical slot in the metasurface structure supporting the anapole by d = 5 nm along the y direction with respect to the disk center. Then the symmetry of the whole system was slightly broken, leading to the transition of the BIC into a quasi-BIC resonance, which has the possibility of being excited by a plane wave. Figure 4a presents the simulated transmission spectrum through this metasurface structure under the excitation of an x-polarized plane wave. A strong and sharp optical resonance with also an asymmetric Fano profile is found located near 1990.63 nm with a Q-factor of about 2.5×10^5. Figure 4b presents the electric and magnetic field distributions at the resonance, where the white arrows still represent the electric displacement current vectors. The field enhancement of the quasi-BIC system is further enlarged by approximately one order of magnitude compared to those achieved at both TD and anapole resonances. Figure 4b also shows that the maximum field enhancement occurs at both ends of the elliptical slot, where the particles are more easily captured. One can also see

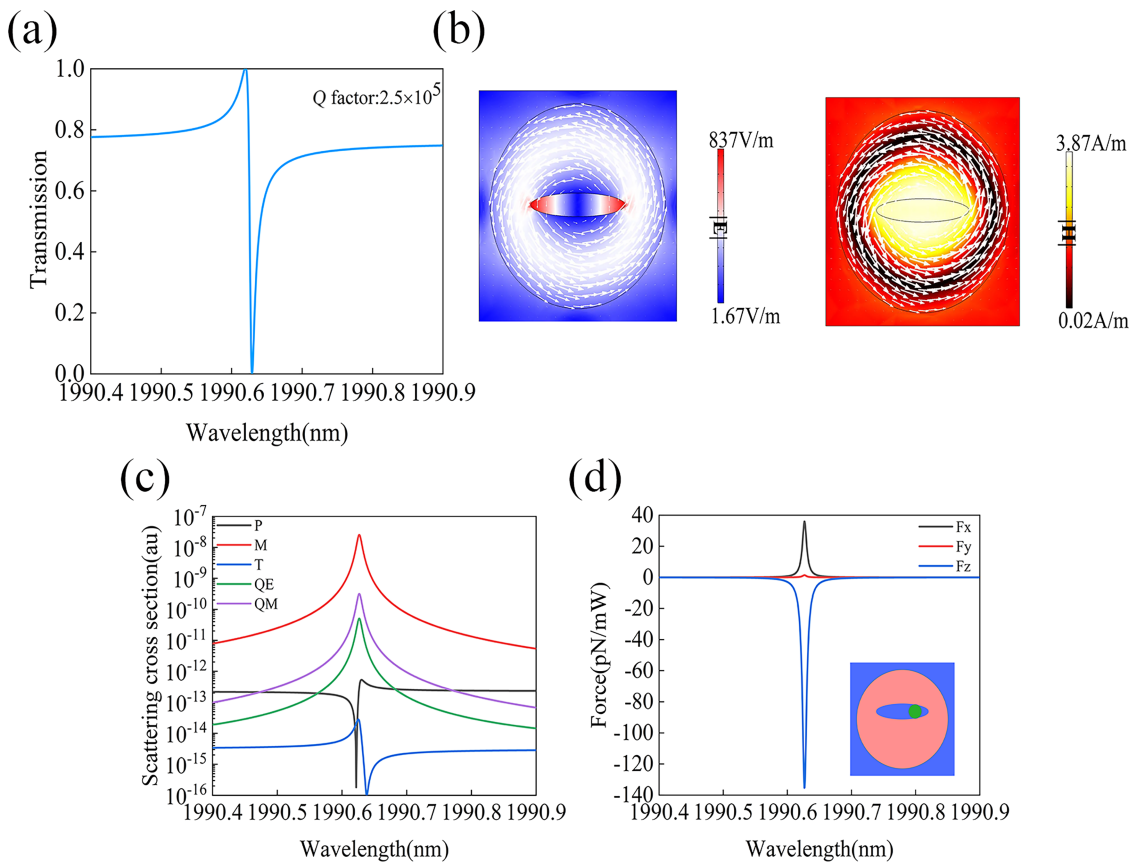

Figure 4: (a) Calculated transmission spectrum through the metasurface supporting the quasi-BIC resonance. (b) Electric and magnetic field distributions at the quasi-BIC resonance, where the white arrows represents the displacement current vectors. (c) Contributions from different multipoles to the overall scattering as a function of wavelength. (d) Calculated optical force spectrum on the PS sphere; the inset shows one unit cell of the geometry and the position of the PS.

from Figure 4b that a counterclockwise loop of the electric displacement current is excited inside the silicon disk, which is related with an MD moment along the z-axis.

To further investigate the origin of the supported quasi-BIC resonance, we calculated the multipole contributions to the overall scattered power at different wavelengths. From the results in Figure 4c, it is clear that the scattered power from the MD resonance dominates the resonance at the wavelength of 1990.63 nm (i.e., the quasi-BIC response is caused by the MD resonance). Under the x-polarized incident light excitation, the dielectric structure generates a displacement current which is roughly, although not exactly, centrosymmetric. So the electric current in one quadrant of the disk will cancel that in the opposite quadrant, leading to the smallest ED moment among all the multipoles. The PS sphere has a diameter of 50 nm and is assumed to be located at the position (x_0, y_0, z_0) = (150 nm, 5 nm, 260 nm), as illustrated by the inset of Figure 4d (i.e., 35 nm above the top surface of the disk). The geometry of the metasurface unit cell and the position of the PS sphere are shown in the inset of Figure 4d. Figure 4d presents the optical force spectrum, which shows that the optical force on the PS sphere at the wavelength of the quasi-BIC is much higher (F_x = 36 pN/mW, F_y = 1.4 pN/mW, F_z = −135 pN/mW) compared to those achieved with the TD resonance and the anapole. This higher optical force is due to a higher Q-factor (2.5×10^5) and the associated much stronger electric field enhancement (837 times) with the quasi-BIC mode. The results show that even at a relatively low laser power intensity, the PS sphere located in the metasurface supporting the quasi-BIC resonance will be subjected to a strong optical force, which means the PS sphere can be stably captured.

Discussion and Conclusion

Table 1 presents a direct comparison of different characteristics at the excitation of three resonances investigated in this work. It can be seen that at the same excitation power intensity, the optical force generated by the quasi-BIC resonance is about

Table 1: Comparison of different characteristics with the three resonances studied in this work.

Resonance	Q-factor	E field enhancement	F_x (pN/mW)	F_y (pN/mW)	F_z (pN/mW)
TD	175	20.1	0.0017	0	−0.134
anapole	106	11.2	0.0005	0	−0.0342
quasi-BIC	2.5×10^5	837	36	1.4	−135

three orders of magnitude larger than those generated by the TD and anapole resonances. The contrast in the achieved optical forces is consistent with the difference in the resonance Q-factor, which is intrinsically connected with the local electromagnetic field enhancement. We should note that all these values in Table 1 are rough numbers with no optimization (e.g., the Q-factor of the quasi-BIC resonance can be controlled by the level of symmetry breaking (the size and position of the elliptical slot)). However, the results in Table 1 with different orders of magnitude in the achieved optical forces still provide a straightforward contrast regarding the characteristics of optical forces with different kinds of resonances supported by all-dielectric nanostructures.

We should note that in the above results summarized in Table 1, the Q-factor of the quasi-BIC is overwhelmingly larger than the other two types of resonances. However, the ultra-high Q-factor of the quasi-BIC mode results from a collective behavior of all array elements. When only a single nanostructure is used the Q-factor can be significantly reduced, although the quasi-BIC mode can also be supported either due to symmetry incompatibility [22] or due to the strong coupling between different modes [23]. In general, to trap multiple nanoparticles using periodic nanostructures the quasi-BIC resonance is usually the first choice. However, to trap a single particle with isolated nanostructures, further investigation needs to be performed for a better comparison.

In conclusion, to the best of our knowledge, we systematically investigated for the first time and compared the optical trapping capability of three mainstream optical resonances that can be supported by all-dielectric nanostructure arrays. The high Q-factor and strong electric field enhancement that can be provided by the quasi-BIC resonance makes it a more suitable option over other resonances for the trapping of multiple nanoparticles using periodic structures. These results will provide useful guidelines when one designs nano-optical tweezers system to capture nanoscale particles. The low absorption losses, high laser power damage threshold as well as the large optical force that can be achieved with lossless all-dielectric nanostructures provide a better choice compared to the metallic counterpart in optical capturing of nanoscale particles and may have broad applications in medicine and biology.

Funding

This work was supported by the National Science Foundation of China under the projects 11974221 and 12274269.

ORCID® iDs

Zhanghua Han - https://orcid.org/0000-0002-4177-2555

References

1. Rodríguez-Fortuño, F. J.; Engheta, N.; Martínez, A.; Zayats, A. V. *Nat. Commun.* **2015,** *6,* 8799. doi:10.1038/ncomms9799
2. Grier, D. G. *Nature* **2003,** *424,* 810–816. doi:10.1038/nature01935
3. Jackson, J. D.; Fox, R. F. *Am. J. Phys.* **1999,** *67,* 841–842. doi:10.1119/1.19136
4. Juan, M. L.; Righini, M.; Quidant, R. *Nat. Photonics* **2011,** *5,* 349–356. doi:10.1038/nphoton.2011.56
5. Papasimakis, N.; Fedotov, V. A.; Savinov, V.; Raybould, T. A.; Zheludev, N. I. *Nat. Mater.* **2016,** *15,* 263–271. doi:10.1038/nmat4563
6. Zel'dovich, I. B. *Sov. Phys. - JETP* **1958,** *6,* 1184–1186.
7. Naumov, I. I.; Bellaiche, L.; Fu, H. *Nature* **2004,** *432,* 737–740. doi:10.1038/nature03107
8. Ahmadivand, A.; Gerislioglu, B.; Ahuja, R.; Mishra, Y. K. *Laser Photonics Rev.* **2020,** *14,* 1900326. doi:10.1002/lpor.201900326
9. Wang, R.; Dal Negro, L. *Opt. Express* **2016,** *24,* 19048–19062. doi:10.1364/oe.24.019048
10. Miroshnichenko, A. E.; Evlyukhin, A. B.; Yu, Y. F.; Bakker, R. M.; Chipouline, A.; Kuznetsov, A. I.; Luk'yanchuk, B.; Chichkov, B. N.; Kivshar, Y. S. *Nat. Commun.* **2015,** *6,* 8069. doi:10.1038/ncomms9069
11. von Neumann, J.; Wigner, E. P. Über das Verhalten von Eigenwerten bei adiabatischen Prozessen. In *The Collected Works of Eugene Paul Wigner;* Wightman, A. S., Ed.; Springer: Berlin, Heidelberg, 1993; Vol. A/1, pp 294–297. doi:10.1007/978-3-662-02781-3_20
12. Marinica, D. C.; Borisov, A. G.; Shabanov, S. V. *Phys. Rev. Lett.* **2008,** *100,* 183902. doi:10.1103/physrevlett.100.183902
13. Romano, S.; Zito, G.; Torino, S.; Calafiore, G.; Penzo, E.; Coppola, G.; Cabrini, S.; Rendina, I.; Mocella, V. *Photonics Res.* **2018,** *6,* 726–733. doi:10.1364/prj.6.000726
14. Mikheeva, E.; Koshelev, K.; Choi, D.-Y.; Kruk, S.; Lumeau, J.; Abdeddaim, R.; Voznyuk, I.; Enoch, S.; Kivshar, Y. *Opt. Express* **2019,** *27,* 33847–33853. doi:10.1364/oe.27.033847
15. Liu, Z.; Xu, Y.; Lin, Y.; Xiang, J.; Feng, T.; Cao, Q.; Li, J.; Lan, S.; Liu, J. *Phys. Rev. Lett.* **2019,** *123,* 253901. doi:10.1103/physrevlett.123.253901
16. Gao, X.; Hsu, C. W.; Zhen, B.; Lin, X.; Joannopoulos, J. D.; Soljačić, M.; Chen, H. *Sci. Rep.* **2016,** *6,* 31908. doi:10.1038/srep31908
17. Novotny, L. Forces in Optical Near-Fields. *Near-field optics and surface plasmon polaritons;* Topics in Applied Physics; Springer: Berlin, Heidelberg, 2001; pp 123–141. doi:10.1007/3-540-44552-8_7

18. Liaw, J.-W.; Chen, Y.-S.; Kuo, M.-K. *Appl. Phys. A: Mater. Sci. Process.* **2016,** *122,* 182. doi:10.1007/s00339-016-9732-4
19. Savinov, V.; Fedotov, V. A.; Zheludev, N. I. *Phys. Rev. B* **2014,** *89,* 205112. doi:10.1103/physrevb.89.205112
20. Hwang, M.-S.; Lee, H.-C.; Kim, K.-H.; Jeong, K.-Y.; Kwon, S.-H.; Koshelev, K.; Kivshar, Y.; Park, H.-G. *Nat. Commun.* **2021,** *12,* 4135. doi:10.1038/s41467-021-24502-0
21. Limonov, M. F.; Rybin, M. V.; Poddubny, A. N.; Kivshar, Y. S. *Nat. Photonics* **2017,** *11,* 543–554. doi:10.1038/nphoton.2017.142
22. Koshelev, K.; Kruk, S.; Melik-Gaykazyan, E.; Choi, J.-H.; Bogdanov, A.; Park, H.-G.; Kivshar, Y. *Science* **2020,** *367,* 288–292. doi:10.1126/science.aaz3985
23. Bogdanov, A. A.; Koshelev, K. L.; Kapitanova, P. V.; Rybin, M. V.; Gladyshev, S. A.; Sadrieva, Z. F.; Samusev, K. B.; Kivshar, Y. S.; Limonov, M. F. *Adv. Photonics* **2019,** *1,* 016001. doi:10.1117/1.ap.1.1.016001

License and Terms